AD-A185 077 DEVELOPMENT OF A MICROBURST TURBULENCE MODEL FOR THE    1/1
JOINT AIRPORT WEATHER STUDIES WIND SHEAR DATA(U)
H CHANG ET AL. MAR 87 DOT/FAA/PM-87/12
UNCLASSIFIED DTFA01-82-Y-10513                F/G 4/2        NL
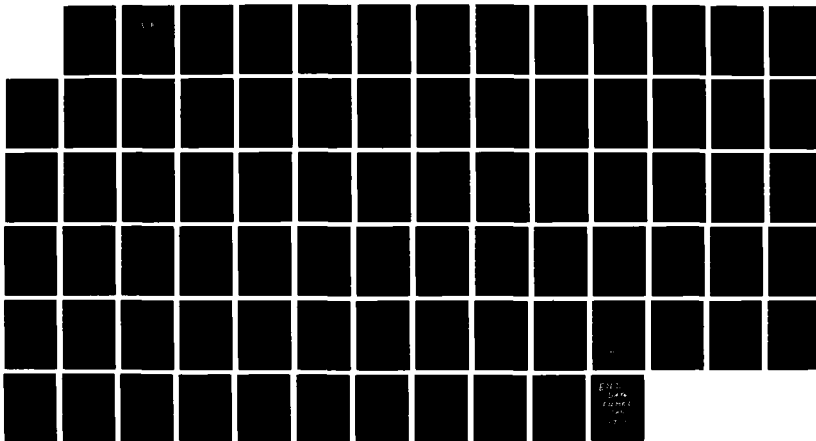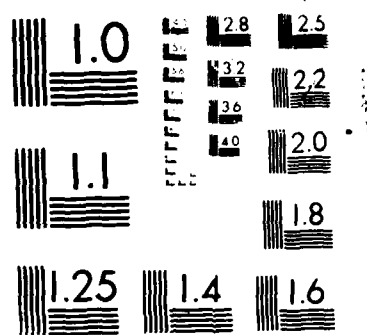
DOT/FAA/PM-87/12

Program Engineering
and Maintenance Service
Washington, D.C. 20591

AD-A185 877

# Development of a Microburst Turbulence Model for the Joint Airport Weather Studies Wind Shear Data

DTIC
SELECTED
OCT 1 5 1987
D

Ho-Pen Chang
Walter Frost

FWG Associates, Inc.
Rt. 2, Box 271-A
Tullahoma, TN 37388

for

Research Applications Program
National Center for Atmospheric Research
P.O. Box 3000
Boulder, CO 80307

March 1987

U.S. Department of Transportation
**Federal Aviation Administration**

87   10 2 091

| 1. Report No. | 2. Government Accession No. | 3. Recipient's Catalog No. |
|---|---|---|
| DOT/FAA/PM-87/12 | AD-A185877 | |

| 4. Title and Subtitle | 5. Report Date |
|---|---|
| Development of a Microburst Turbulence Model for the Joint Airport Weather Studies (JAWS) Wind Shear Data | March 1987 |
| | 6. Performing Organization Code |
| | 8. Performing Organization Report No. |

| 7. Author's: |
|---|
| Ho-Pen Chang and Walter Frost |

| 9. Performing Organization Name and Address | 10. Work Unit No. (TRAIS) |
|---|---|
| FWG Associates Rt. 2, Box 271A Tullahoma, TN 37388 | |
| | 11. Contract or Grant No. |
| | DTFA01-82-Y-10513 |
| | 13. Type of Report and Period Covered |

| 12. Sponsoring Agency Name and Address | |
|---|---|
| U.S. Department of Transportation Federal Aviation Administration Program Engineering and Maintenance Service Washington, D.C. 20591 | Technical Report |
| | 14. Sponsoring Agency Code |
| | APM-310 |

15. Supplementary Notes

Research performed under Interagency Agreement No. DTFA01-82-Y-10513 between the National Science Foundation and the Federal Aviation Administration.

16. Abstract

A turbulence model is developed to supplement the microburst quasi-steady wind shear model established earlier from the JAWS Doppler radar data sets. The wind shear model is, in effect, a quasi-steady, spatially varying wind field. The spatial scale of the wind variation is on the order of 500-750 ft (150-200 m). Airborne sensor response (i.e., angle of attack, stall warning, pitot tubes, etc.), structural dynamics, pilot workload, and other such factors, however, respond to much higher frequency wind effects. To account for these effects, a "first-cut" turbulence model based on Doppler radar second moment data is presented. Superimposing the turbulent fluctuation from this turbulence model on the quasi-steady JAWS wind field is believed to provide a more realistic simulation of the microburst flow for aviation application.

The Doppler radar second moments or spectral width data from the June 30, July 14, and August 5, 1982, JAWS microburst measurements are analyzed in considerable detail. Microburst turbulence intensity is calculated by subtracting the spectral width broadenings due to wind shear, antenna motion, and precipitation fall speeds from the radar spectra width. The turbulence intensity is compared with the in situ measurement from the NASA B-57B aircraft. Isotropy of a microburst turbulence is quantitatively investigated by comparing the turbulence information from two radar stations which observed the microburst at different directions (approximately 90°). The turbulence energy contained in a microburst is compared with the theoretical models, both Dryden spectrum and von Karman spectrum. By using a curve-fitting technique, a functional form of the microburst turbulence intensity is found in terms of the radial distance from the microburst center and the height above the ground. Based on these turbulence parameters relevant to a microburst, a turbulence model is developed to supplement the existing JAWS quasi-steady mean wind data. Finally, the turbulence model is applied to flight simulations of a B727-type aircraft approaching and/or taking off through a JAWS microburst.

| 17. Key Words | 18. Distribution Statement |
|---|---|
| Turbulence, Doppler radar, spectrum width, wind shear, microburst, second moment, curve fitting, radial distance, flight simulation, approach, departure | This document is available to the public through the National Technical Information Service, Springfield, Virginia 22161. |

| 19. Security Classif. (of this report) | 20. Security Classif. (of this page) | 21. No. of Pages | 22. Price |
|---|---|---|---|
| Unclassified | Unclassified | 77 | |

Form DOT F 1700.7 (8-72)    Reproduction of completed page authorized

## ACKNOWLEDGMENT

## TABLE OF CONTENTS

## LIST OF TABLES

## LIST OF FIGURES

v

## NOMENCLATURE

| | |
|---|---|
| C | Speed of light, $3.0 \times 10^8$ m/s |
| f | Frequency (Hz) |
| h | Normalized height |
| $K_r, K_\theta, K_\phi$ | Radial wind shears in radial direction (1/sec), elevational direction (1/(radian·sec)), and azimuthal direction (1/(radian·sec)), respectively |
| ln | Natural logarithm function |
| NC | Normalized coherent power $= |R(\tau)|/R(0)$ |
| $P_N$ | Linear channel noise power ($dB_m$) |
| $P_S$ | Linear channel signal power ($dB_m$) |
| PRF | Pulse repetition frequency of a radar system (1/sec) |
| $R_0$ | Radial distance of a pulse volume from a radar system (m) |
| $R(\tau)$ | Auto-correlation function of the signal power received by a radar system |
| r | Normalized radial distance |
| V | Local quasi-steady mean wind (m/s) |
| $V_0$ | Mean wind velocity (m/s) |
| $V_r$ | Radial velocity along radar beam (m/s) |

### Greek Symbols

| | |
|---|---|
| $\alpha$ | Angular velocity of radar beam (radians/sec) |
| $\theta, \phi$ | Elevation angle and azimuth angle of the radar beam relative to a reference coordinate system (degrees, radians) |
| $\gamma$ | One-way half-power pattern width of a radar system (radians); glide slope angle (degrees) |
| $\Lambda_1, \Lambda_2, \Lambda_3$ | Turbulence length scale (m) |
| $\lambda$ | Wavelength of a radar system (m) |
| $\pi$ | 3.14159 ... |

| | |
|---|---|
| $\sigma_d$ | Spectrum width broadening due to different speeds of falls for various sized drops (m/s) |
| $\sigma_{do}$ | Spectrum width broadening caused by the spread in terminal velocity of various size drops (m/s) |
| $\sigma_p$ | Pulse standard deviation, second moment (m/s) |
| $\sigma_r^2$ | Second central moment of a distance-weighting function (m²) |
| $\sigma_s$ | Spectrum width broadening due to radial wind shear (m/s) |
| $\sigma_t$ | Microburst turbulence intensity (m/s) |
| $\sigma_w$ | Wind standard deviation (m/s) |
| $\sigma_\alpha$ | Spectrum width broadening due to antenna motion (m/s) |
| $\sigma_\theta^2, \sigma_\phi^2$ | Second central moments of the two-way antenna power pattern in directions $\theta$ and $\phi$, respectively (radian²) |
| $\sigma_1, \sigma_2, \sigma_3$ | Turbulence intensity in longitudinal, lateral, and vertical directions, respectively (m/s) |
| $\tau$ | Pulse duration of a Doppler radar system (sec) |
| $\phi_1(K), \phi_2(K), \phi_3(K)$ | Turbulence energy spectrum functions in longitudinal, lateral, and vertical directions, respectively (in wave number domain, m³/(sec²·radians)) |

# 1.0 INTRODUCTION

The Workshop on Wind Shear/Turbulence Inputs to Flight Simulation and Systems Certification (Frost and Bowles 1984) concluded that knowledge of the inter-relation between turbulence and wind shear is required to provide a better understanding of the microburst phenomenon. Actually, the distinction between wind shear and turbulence is simply a matter of definition; wind shear is low-frequency turbulence. JAWS radar-measured microburst data sets are smoothed through synthesis to a spatial grid that is about 656 x 656 x 820 ft (200 x 200 x 250 m). There are atmospheric disturbances within the volume element that are relatively large compared to the aircraft. These disturbances, however, are smoothed out by the data reduction process for the JAWS microburst data sets. As Campbell (1984) and Frost (1984) pointed out, high-frequency turbulence should be superimposed on the JAWS data. The subject of this study is to develop an effective microburst turbulence model to supplement the existing JAWS data.

As Taylor and von Karman have stated, turbulence can be generated by friction forces at fixed walls or by the flow of layers of fluids with different velocities past or over one another. Usually, turbulence generated by fixed walls is designated as "wall turbulence" and turbulence in the absence of walls is indicated as "free turbulence." In the literature, several investigators (Fichtl 1973, Barr et al. 1974, Frost et al. 1978) have summarized models of atmospheric boundary layer turbulence. Turbulence length scale and intensity used in their models are proportional to the height above level terrain, which is probably not true for microburst turbulence.

A number of studies (Zegadi et al. 1983, Boldman and Brinich 1977, Costello 1976) are devoted to the problem of measuring the turbulence characteristics in impinging jet flows which contain free turbulences. Recently, the structure of turbulence in an impinging jet in a uniform crossflow was studied by Shayesteh et al. (1985) and Crabb et al. (1981). Because microburst turbulence is a mixture of wall turbulence (in the atmospheric boundary layer) and free turbulence (in the downburst flow), its turbulence characteristics are essentially affected by the interaction between two kinds of turbulence flows. JAWS radar-measured data provided turbulence information (radar spectral width and wind standard deviation) associated with a microburst (Elmore and McCarthy 1984). Based on this turbulence information, a microburst turbulence model has been defined and its effect on simulated aircraft flight studied in this report.

A detailed analysis of the JAWS radar-measured turbulence information with emphasis on finding the significant turbulence parameters for JAWS microbursts is first reported. The radar-measured turbulence data are then compared with the *in situ* aircraft measurements. The comparison shows that the analytical Dryden spectrum model is a reasonable approximation to the partitioning of energy between frequencies within microburst turbulence (at least higher frequencies). A polynomial curve-fitting technique is applied to find the form of the JAWS microburst turbulence intensity as a function of the radial distance from the microburst center and the height above ground. The length scales associated with the microburst turbulence are commuted by integrating the auto-correlation function of the quasi-steady mean wind components.

To investigate the effect of turbulence on aircraft trajectories through the JAWS data sets, three turbulent wind components are computer simulated with a z-transformation technique. As statistical analysis of the simulated turbulence wind components along the aircraft's trajectories is made and the influence of the microburst turbulence on the aircraft performance is investigated.

## 2.0 ANALYSES OF JAWS TURBULENCE DATA

In addition to the spatial velocity and reflectivity fields of the JAWS microbursts, which were analyzed and reported by Frost et al. (1985), JAWS data sets also provided turbulence information in the form of radar-measured pulse, wind, and total standard deviations (defined below). Analyses of these turbulence data are presented in this section. Figure 1 shows the locations and the coordinates of three JAWS microbursts with respect to the CP-2 radar. Table 1 lists basic information about the three microburst data sets measured on June 30, July 14, and August 5, 1982. Three radar stations, CP-2, CP-3, and CP-4, were operated in the JAWS field experiment. The characteristics of the radars are given in Table 2.

### 2.1 Definition of Measurements

The definitions of the JAWS turbulence measurements, pulse, wind, and total standard deviations are:

Pulse standard deviation, $\sigma_p$, is the total spectrum width, also called the second moment. For a single range gate, it is calculated from the equation (Keeler and Frush 1984):

$$\sigma_p = \begin{cases} \dfrac{\lambda \cdot PRF}{\sqrt{8}\ \pi} \sqrt{-\ln[NC \cdot (1 + P_N/P_S)]}\ \text{m/s}, & P_S < -90\ dB_m \\[3mm] \dfrac{\lambda \cdot PRF}{\sqrt{8}\ \pi} \sqrt{-\ln[NC]}\ \text{m/s}, & P_S \geqslant -90\ dB_m \end{cases}$$

(1)

with the constraint that $[NC \cdot (1 + P_N/P_S)] < 1$ where $\lambda$ is the radar wavelength (m), PRF is the radar pulse repetition frequency (1/sec), $P_N$ is the linear channel noise power as determined from system measurement or the calibration curve ($dB_m$), $P_S$ is the linear channel signal power as determined from the calibration curve ($dB_m$), and NC is the normalized coherent power estimate equal to $|R(\tau)/R(0)|$; $R(\tau)$ is the auto-correlation function of the signal power received by the radar system. However, the JAWS $\sigma_p$ provided for analysis is a Cressman weighted average at each grid point. Therefore, in this analysis we assume that $\sigma_p$ represents the pulse standard deviation for a pulse volume centered at the grid point. Without the raw data, the influence of this assumption cannot be meaningfully assessed.

Wind standard deviation $\sigma_w$ at each grid point is the square root of the variance of the weighted velocity estimates used to compute the quasi-steady mean wind at the grid point.

$$\sigma_w = \left[\frac{1}{N} \Sigma(V_r^2 - \overline{V}_r^2)\right]^{1/2}$$

(2)

where N is the number of range gates involved in a grid volume. The effects of motion scales larger than the pulse volume and smaller than the grid volume are approximated by the variance, square of $\sigma_w$. Finally, total standard

3
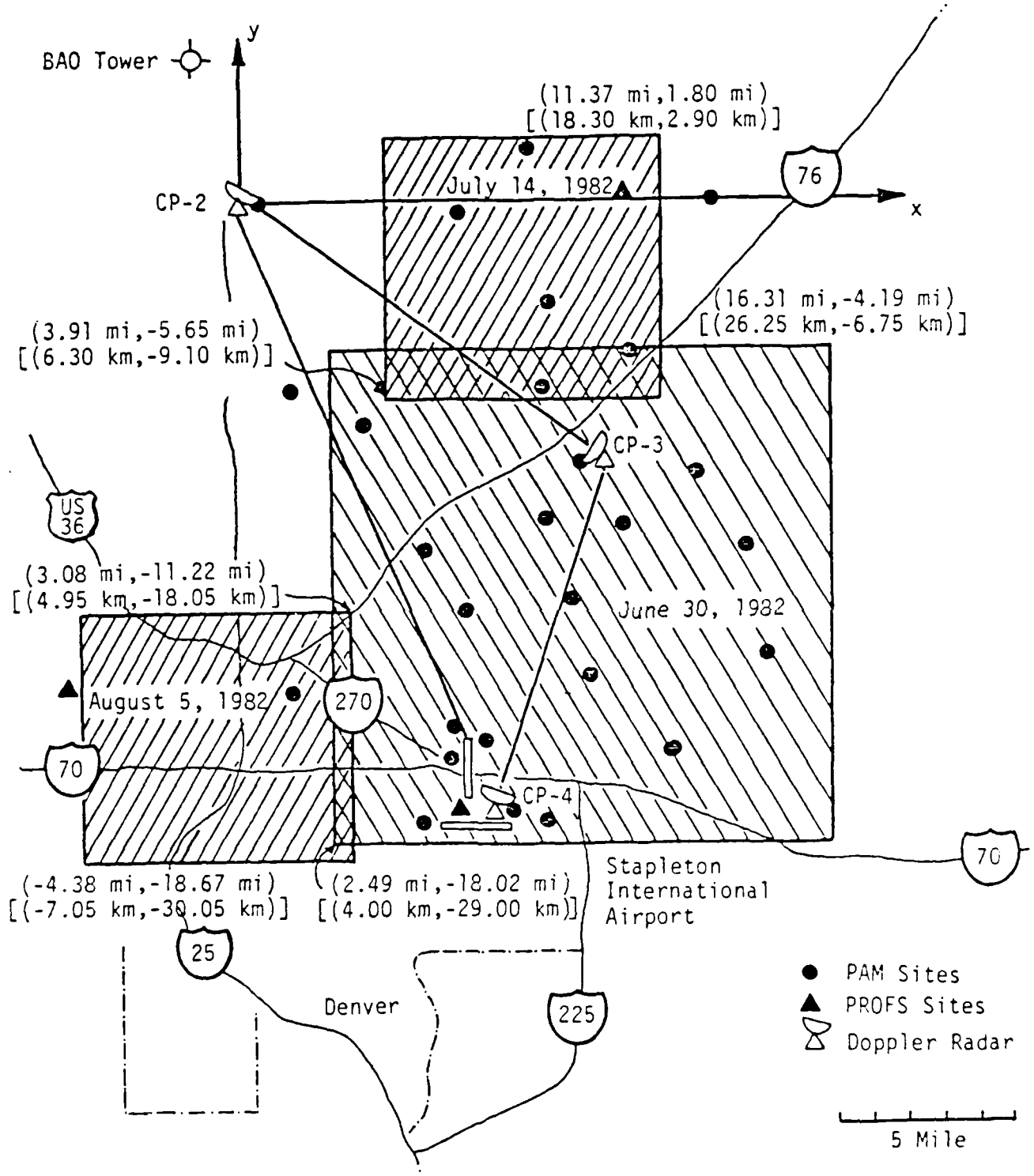
Figure 1. Locations of three JAWS microbursts.

TABLE 1. Three JAWS Microburst Data Sets.

| Data Sets | Nomenclature | Number of Grids | Grid Spacing, ft (m) | Description of Data |
|---|---|---|---|---|
| August 5, 1982 (1845, 1847, 1850, and 1852 MDT measurements) | 5AU1845 5AU1847 5AU1850 5AU1852 | 81x81x9 | 492x492x820 (150x150x250) | Each measurement including: 1) u, v, and w wind speed components 2) Radar reflectivity 3) Pulse SD (from CP-4) 4) Wind SD (from CP-4) 5) Total SD (from CP-4) |
| June 30, 1982 (1821, 1823, and 1826 MDT measurements) | 30JN1821 30JN1823 30JN1826 | 90x90x5 | 820x820x820 (250x250x250) | Same as above |
| July 14, 1982 (1452 MDT measurement) | 14JL1452 | 61x61x11 | 656x656x492 (200x200x150) | 1) u, v, and w wind speed components 2) Radar reflectivity 3) CP-2 pulse SD (from CP-2) 4) CP-2 wind SD (from CP-2) 5) CP-2 total SD (from CP-2) 6) CP-4 pulse SD (from CP-4) 7) CP-4 pulse SD (from CP-4) 8) CP-4 total SD (from CP-4) 9) Pulse average SD 10) Wind average SD 11) Total average SD |

5

TABLE 2.   Characteristics of JAWS Doppler Radar.

| Parameter | CP-2 | CP-3 | CP-4 |
|---|---|---|---|
| Coordinates w.r.t. CP-2 (km) | (0,0) | (14.15,-11.19) | (10.43,-25.45) |
| Wavelength (cm) | 10.67 | 5.45 | 5.49 |
| Pulse duration (μs) | 0.4-1.5 | 1.0 | 1.0 |
| Average power (dB$_m$) | 59 | 55 | 55 |
| Pulse repetition frequency (Hz) | 960, 480 | 1666, 1250 | 1666, 1250 |
| Antenna diameter (m) | 8.534 | 3.658 | 3.658 |
| System gain (dB) | 43.9 | 43.0 | 41.0 |
| Beamwidth (deg) | 0.97 | 1.17 | 1.09 |
| No. of samples in estimate | 32,64,...,2048 | 32,64,...,2048 | 32,64,...,2048 |
| No. of range gates | 256,512,768,1024 | 512 | 512 |
| Azimuthal scan rate (deg/sec) | 0-15 | 0-35 | 0-35 |
| Min. elevation angle increment (deg) | 0.1 | 0.1 | 0.1 |
| Range gate spacing (m) | 90-600 | 150-240 | 150-240 |
| Max. unambiguous range (km) | 150, 300 | 90, 120 | 90, 120 |
| Max. unambiguous velocity (m/s) | ±25.7, ±12.8 | ±22.6, ±17.0 | ±22.8, ±17.2 |

deviation is computed by squaring $\sigma_p$ and $\sigma_w$, summing them, and taking the square root of the result.

As reported by Doviak and Zrnic' (1984), there are four potentially important contributions to the width or second moment of the Doppler spectrum for a narrow beam radar: turbulence, wind shear, antenna motion, and the spread of particle fall speeds.

$$\sigma_p = (\sigma_t{}^2 + \sigma_s{}^2 + \sigma_\alpha{}^2 + \sigma_d{}^2)^{1/2} \tag{3}$$

where $\sigma_s$ is spectrum width broadening due· to radial ·wind shear, $\sigma_t$ is turbulence intensity, $\sigma_\alpha$ is the broadening due to antenna motion, and $\sigma_d$ is the broadening due to different precipitation fall velocities. Rearranging Equation 3, the turbulence intensity is given by:

$$\sigma_t = (\sigma_p{}^2 - \sigma_s{}^2 - \sigma_\alpha{}^2 - \sigma_d{}^2)^{1/2} \tag{4}$$

The cited spectral broadening mechanisms are independent of one another. If one can determine the contributions of the last three in Equation 4, one can isolate the contribution of turbulence for use in the microburst turbulence simulation.

The spectrum width broadening due to the radial wind shear, $\sigma_s$, can be determined directly from the angular dependence of the mean radial velocity as:

$$\sigma_s = [(\sigma_r K_r)^2 + (R_o \sigma_\theta K_\theta)^2 + (R_o \sigma_\phi K_\phi)^2]^{1/2} \tag{5}$$

where $K_r$, $K_\theta$, and $K_\phi$ are the radial wind shears in the directions r (radial), $\theta$ (elevation), and $\phi$ (azimuth), respectively. The radial wind shear terms at point P can be evaluated from (see Figure 2):

$$K_r = \frac{\text{Radial V at } P_{r2} \text{ (m/s)} - \text{Radial V at } P_{r2} \text{ (m/s)}}{150 \text{ m}}$$

$$K_\theta = \frac{\text{Radial V at } P_{\theta2} \text{ (m/s)} - \text{Radial V at } P_{\theta1} \text{ (m/s)}}{\gamma \text{ (radians)} \times R_o \text{ (m)}} \tag{6}$$

$$K_\phi = \frac{\text{Radial V at } P_{\phi2} \text{ (m/s)} - \text{Radial V at } P_{\phi1} \text{ (m/s)}}{\gamma \text{ (radians)} \times R_o \text{ (m)}}$$

Using the volume-weighted interpolation technique developed by Frost et al. (1985), the radial velocities at points $P_{r1}$, $P_{r2}$, $P_{\theta1}$, $P_{\theta2}$, $P_{\phi1}$, and $P_{\phi2}$ in Figure 2 are interpolated from the JAWS full-volume wind speed data. However, the JAWS wind speed at each grid point is a Cressman weighted average. In this analysis, the center of a pulse volume is assumed to be the grid point. $R_o$ is the radial distance of the pulse volume from the radar system. $\sigma_\theta{}^2$ and

7

Radar Station
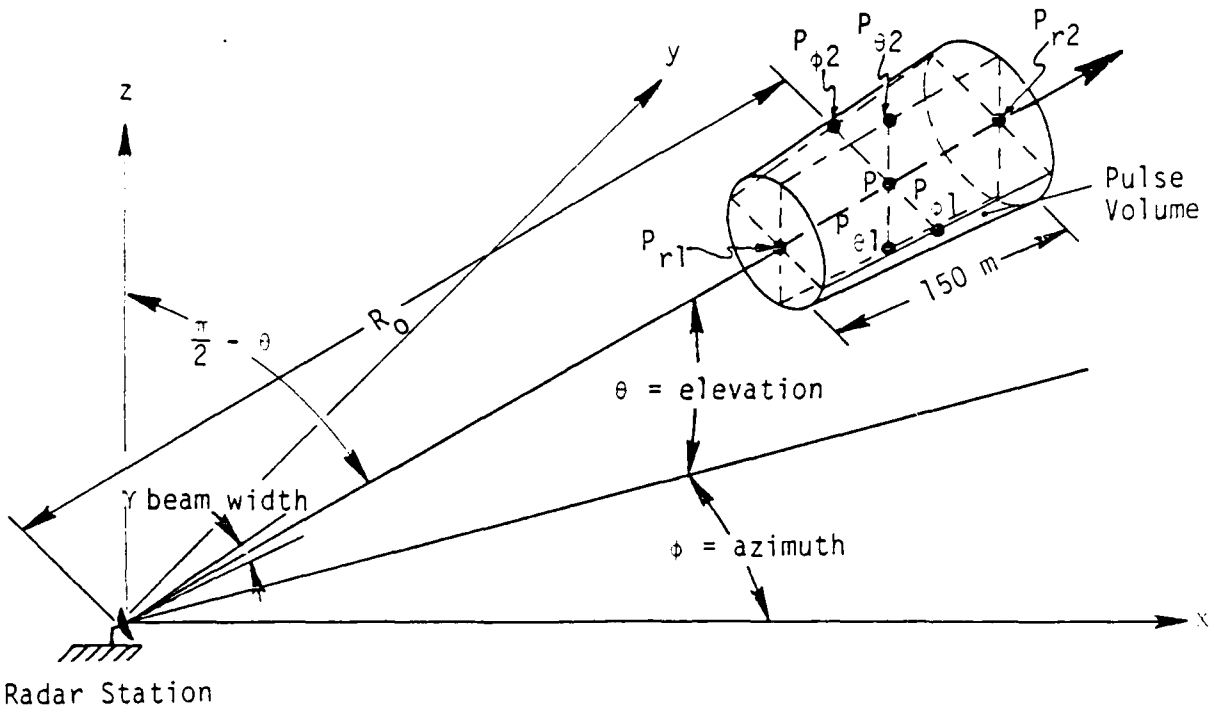
$$K_r = \frac{\text{Radial V at } P_{r2} \text{ (m/s)} - \text{Radial V at } P_{r1} \text{ (m/s)}}{150 \text{ m}}$$

$$K_\theta = \frac{\text{Radial V at } P_{\theta 2} \text{ (m/s)} - \text{Radial V at } P_{\theta 1} \text{ (m/s)}}{\gamma \text{ (radians)} \times R_o \text{ (m)}}$$

$$K_\phi = \frac{\text{Radial V at } P_{\phi 2} \text{ (m/s)} - \text{Radial V at } P_{\phi 1} \text{ (m/s)}}{\gamma \text{ (radians)} \times R_o \text{ (m)}}$$

Figure 2. Definition of radial shear terms, $K_r$, $K_\theta$, and $K_\phi$.

$\sigma_\phi^2$ are the second central moments of the two-way antenna power pattern in the directions $\theta$ and $\phi$, which in terms of the one-way half-power pattern width, $\gamma$, in radians, are (Doviak and Zrnic' 1984):

$$\sigma_\theta^2 = \sigma_\phi^2 = \gamma^2/(16 \ln 2) \qquad (7)$$

Finally, the second central moment of the distance-weighting function is given as (Doviak and Zrnic' 1984):

$$\sigma_r^2 = (0.35 \, C\tau/2)^2 \qquad (8)$$

where C is the speed of light (m/s) and $\tau$ is the pulse duration (sec) of the Doppler radar.

If the antenna pattern is Gaussian with a one-way half-power pattern width, $\theta_1$, and rotates at an angular velocity of $\alpha$, the spectrum width broadening associated with the antenna motion is:

$$\sigma_\alpha = [\dot{\alpha}\lambda \cos(\theta)/2\pi\gamma]\sqrt{\ln 2} \qquad (9)$$

Finally, the spectrum width broadening due to the radial components fall speeds of different sized drops is related to the radar and meteorological parameters by:

$$\sigma_d = \sigma_{do} \sin \theta \qquad (10)$$

where the spectrum width $\sigma_{do}$ is caused by the spread in terminal velocity of various size drops falling relative to the air contained in a given volume. Lhermitte (1963) reported that for rain $\sigma_{do} = 1.0$ m/s and is nearly independent of the drop size distribution.

## 2.2  Analysis of Pulse SD and Wind SD

A Doppler radar system is only capable of detecting the characteristics of the wind field along the radar beam. Therefore, the spectrum width is a measure of the turbulent fluctuations in the radial velocity component along the beam. In this study, the radial velocity at each grid point was obtained by transforming the JAWS longitudinal, lateral, and vertical velocity components at the grid points back to the component in the radial direction relative to the given radar. Although this process introduces some inaccuracies, it does not affect the results.

Figure 3 shows the contours of the radial velocity and pulse SD at ground level from the CP-4 radar for the JAWS July 14 1452 MDT (14JL1452) microburst (whose quasi-steady wind field is quite symmetric about the microburst center). Figure 4 shows the contours of the same parameters in a horizontal plane at a height above ground of approximately 1 km. In the radial velocity plots, the dashed line contours represent radial velocity toward the radar whereas the solid line contours represent the radial velocity

Contour from -14.0 to 2.0 m/s

Contour interval = 1.0 m/s    Mean value = -8.77 m/s

Corner Coordinates w.r.t. CP-2
(11.37 mi, 1.80 mi)
[(18.30 km, 2.90 km)]
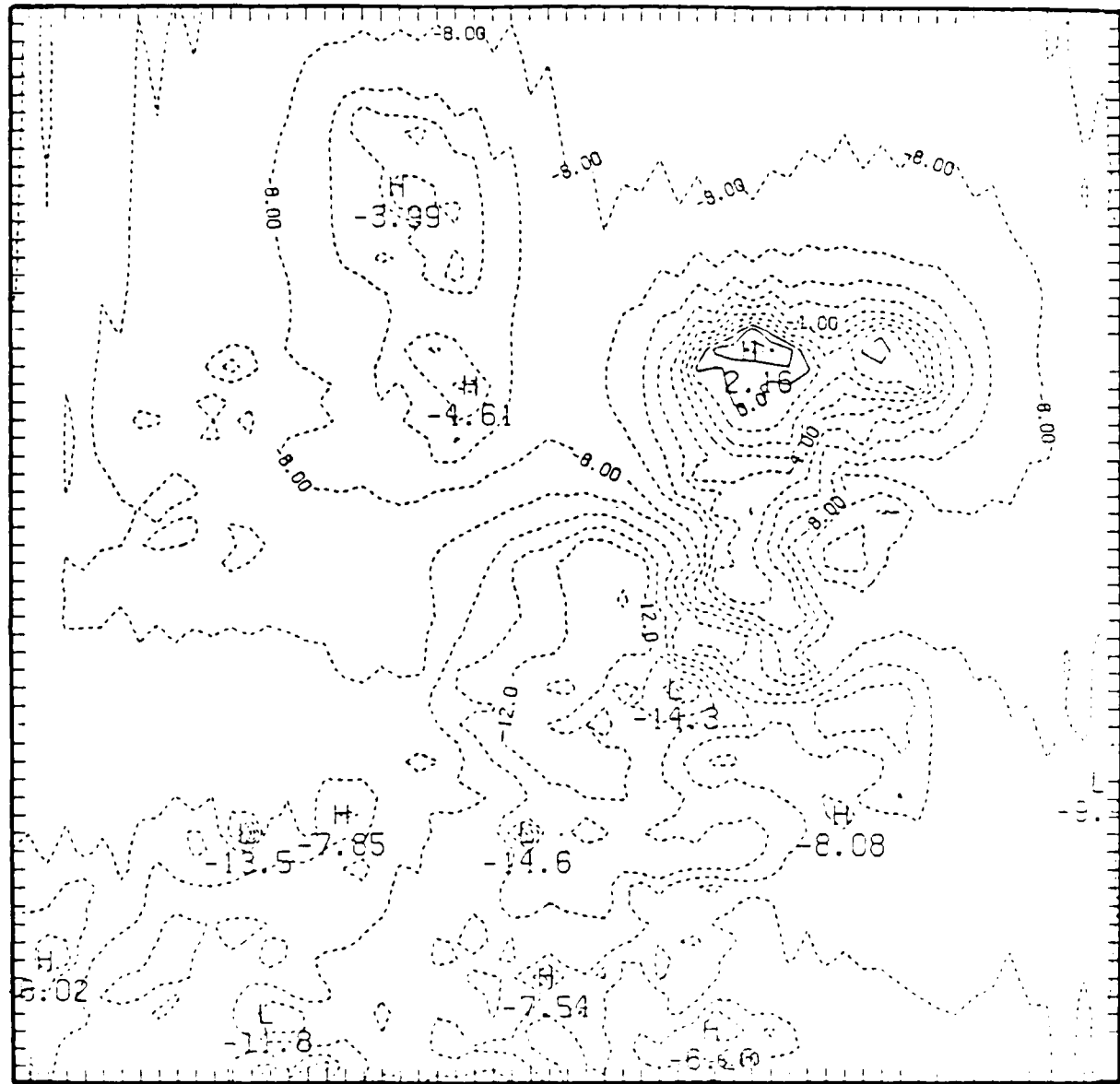
Corner Coordinates w.r.t. CP-2
(3.91 mi, -5.65 mi)
[(6.30 km, -9.10 km)]

(a) Radial velocity

Figure 3.   Contour of radial velocity and pulse SD at ground level for
14JL1452 microburst from CP-2.  (Large numbers correspond to
magnitude of highs and lows while smaller numbers represent
contour values.)

Contour from 3.0 to 10.0 m/s

Corner Coordinates w.r.t. CP-2
(11.37 mi, 1.80 mi)
[(18.30 km, 2.90 km)]

Contour interval = 0.5 m/s    Mean value = 3.12 m/s
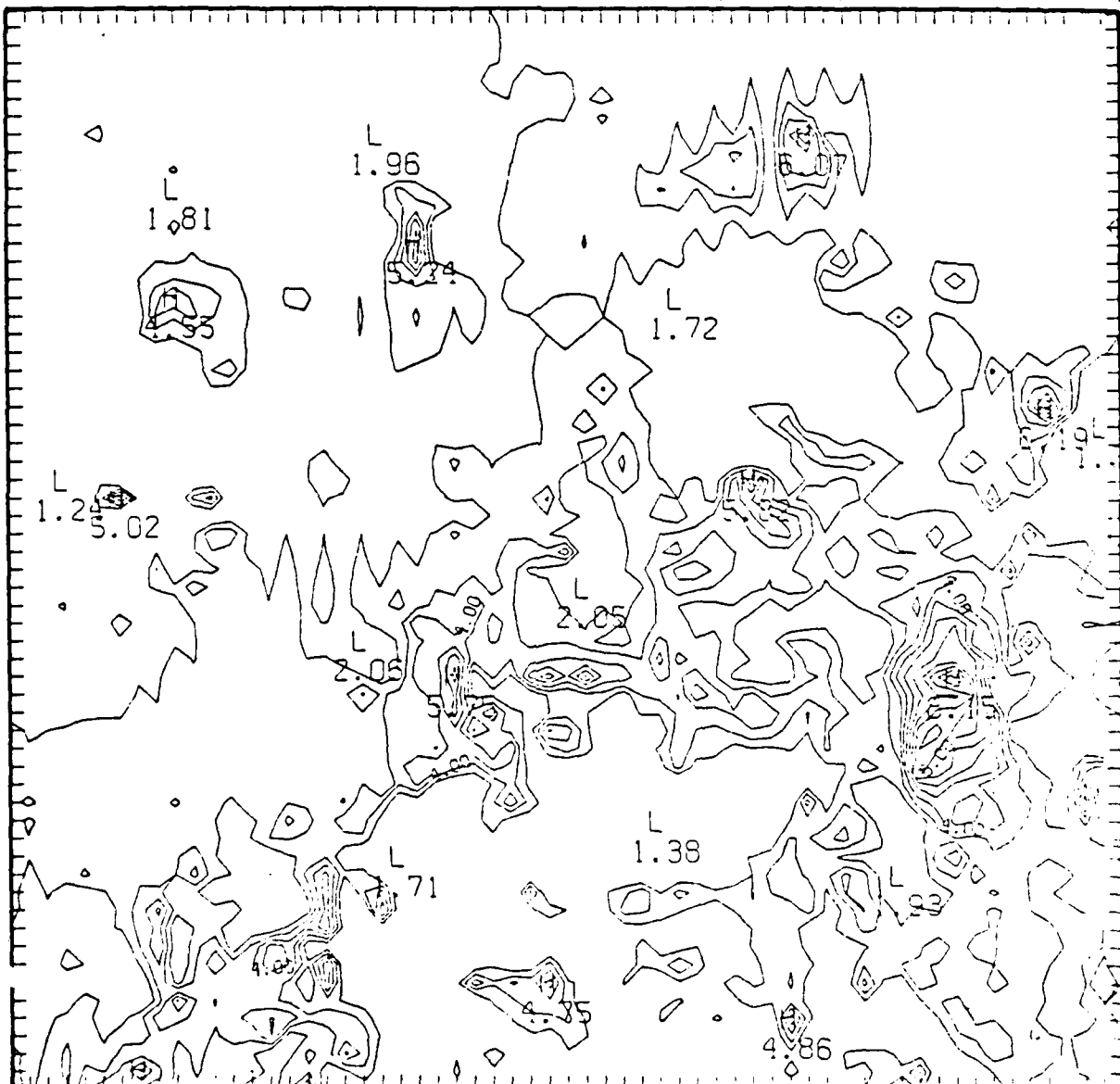


Corner Coordinates w.r.t. CP-2
(3.91 mi, -0.65 mi)
[(6.30 km, -9.10 km)]

(b) Pulse SD

Figure 3.   (continued).

Contour from -10.4 to 1.6 m/s

Corner Coordinates w.r.t. CP-2
(11.37 mi, 1.80 mi)

Contour interval = 0.8 m/s      Mean value = -4.32 m/s     [(13.30 km, 2.90 km)]

Corner Coordinates w.r.t. CP-2
(3.91 mi, -5.65 mi)
[(6.30 km, -9.10 km)]

(a) Radial velocity

Figure 4.   Contour of radial velocity and pulse SD at level 8  (about
            1 km above ground) for 14JL1452 microburst from CP-4.
            (Large numbers correspond to magnitude of highs and lows
            while smaller numbers represent contour values.)

Contour from 3.0 to 10.0 m/s

Contour interval = 0.5 m/s    Mean value = 2.74 m/s

(b) Pulse SD

Figure 4. (continued).

away from the radar. Inspection of Figures 3 and 4 shows that increased $\sigma_p$ coincident with the larger shear regions in Figure 4 but not necessarily in Figure 3. Intuitively one anticipates a correspondence between regions of high turbulence and strong shear. It is believed that this inconsistency at ground level in Figure 3 is possibly due to terrain effects. Similar results are also obtained for the data from the CP-2 radar.

Figure 5 shows contours of the radial velocity and the pulse SD at 1 km above the ground for the August 5 1847 MDT (5AU1847) microburst as measured with the CP-4 radar. The similar coincidence of the larger shear regions with the higher measured spectrum width at upper levels is apparent. Similar results were also obtained from the June 30 microburst data.

CP-2 and CP-4 radars, whose characteristics are listed in Table 2, simultaneously measured the turbulence information associated with the JAWS July 14 microburst. Since the two radars view the same turbulence from different directions (an angle of almost 90°), agreement between their respective measurements will indicate to what degree the microburst turbulence may be considered isotropic. Figure 6 shows contours of the wind SD at a height of 0.9 km from the CP-4 and CP-2 radars. Figure 7 shows contours of the absolute value of the wind SD difference between the CP-4 and CP-2 radars, $\Delta\sigma_w = |\sigma_{w,CP-4} - \sigma_{w,CP-2}|$ at a height of 0.9 km. Similar analysis for the pulse SD is shown in Figures 8 and 9. The SD measurements from both CP-4 and CP-2 radars show good correlation with the exception of a few highly localized locations. These localized values cannot be described on a physical basis and are believed to be signal anomalies.

A cumulative probability technique has been used to quantitatively illustrate the characteristics of the JAWS microburst turbulence measurements. Figure 10 shows the cumulative probability distributions of the pulse SD and the wind SD for the 14JL1452 microburst measured with both the CP-2 and CP-4 radars. Figure 10 also shows the cumulative probability distributions of the SD differences, $\Delta\sigma_w$ and $\Delta\sigma_p$. These probabilities are derived from the full-volume data set including 61 x 61 x 11 grid points. About 80 percent of $\Delta\sigma_p$ are less than 1 m/s, which is approximately equal to the background turbulence level of the microburst, and 80 percent of $\Delta\sigma_w$ are less than 0.5 m/s. Therefore, it is concluded that the SD's from the CP-2 and CP-4 radars have good correlation with each other in over 80 percent of the full volume. This correlation shows that both radars are measuring similar properties in the same way and also suggests the turbulence to be isotropic. As expected, $\sigma_p$ is larger than $\sigma_w$. This is because the second moment estimate involves a difference while the velocity estimate does not. Moreover, the second moment estimate is a better representation of turbulence intensity on a smaller scale compared with the grid scales. Therefore, it is argued that the microburst turbulence intensity should be derived from the pulse SD by removing the spectral broadening effects mentioned earlier. A value of pulse SD in excess of 2.5 m/s exists for 50 percent of the full-volume data set. This suggests that over half of the microburst volume contains light to moderate turbulence. The wind SD, however, exceeds 2.5 m/s in less than 1 percent of the full microburst volume. Finally, Figure 10 shows a limiting value of the spectrum width of about 1 m/s which represents the background turbulence level throughout the full microburst volume. This significant background value is attributed to the radial wind shear effects and was not found in any of three tornadic storms reported by Doviak and Zrnic' (1984). As it is clearly seen
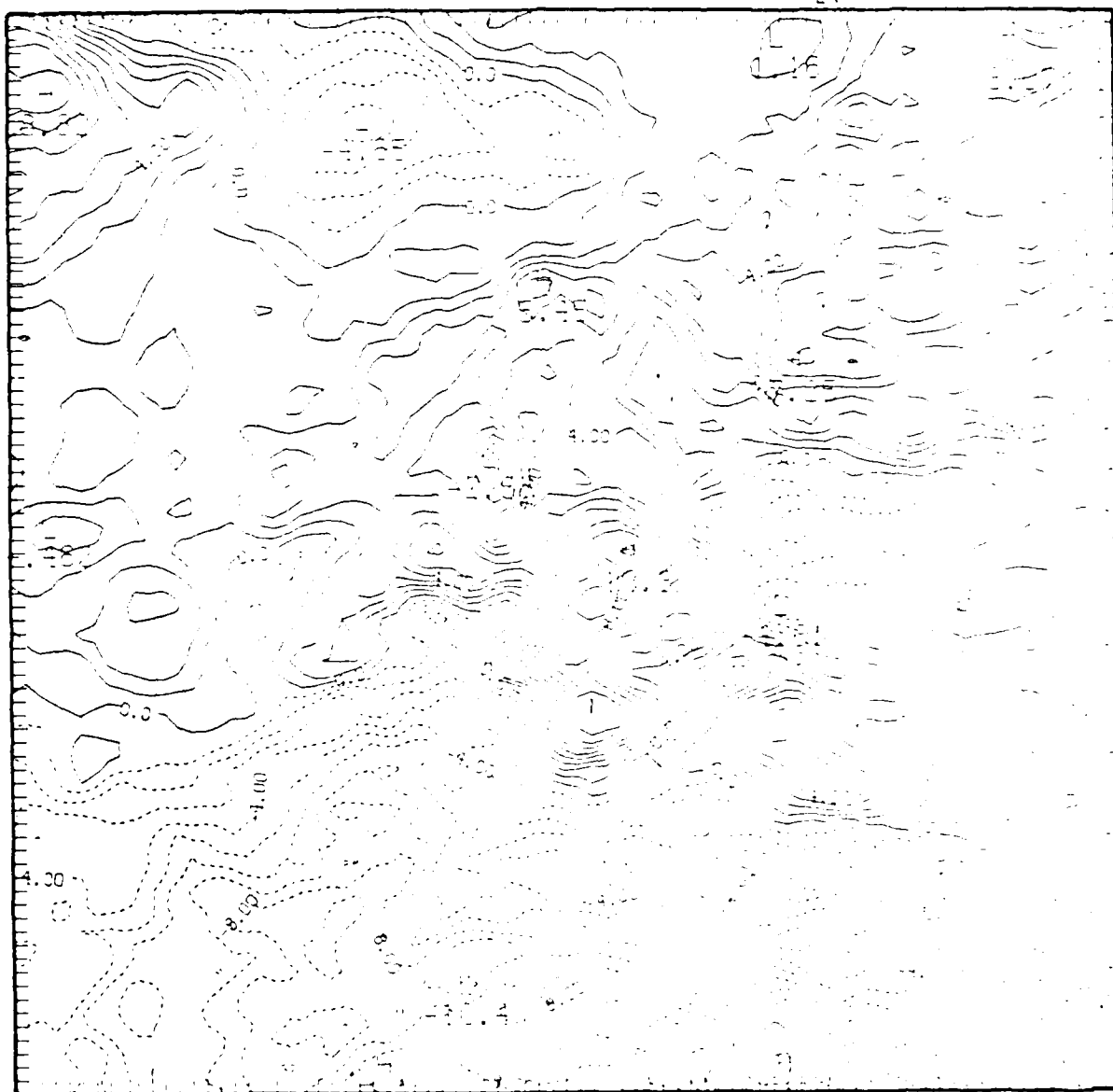
Corner Coordinates w.r.t. CP-2
(4.38 mi, -18.67 mi)
[(-7.05 km, -30.05 km)]

(a) Radial velocity

Figure 5.   Contour of radial velocity and pulse SD at level 5 (1 km
            above ground) for 5AU1847 microburst from CP-4.   (Large
            numbers correspond to magnitude of highs and lows while
            smaller numbers represent contour values.)

Contour from 3.0 to 9.5 m/s

Contour interval = 0.5 m/s    Mean value = 2.58 m/s



Corner Coordinates w.r.t. CP-2
(4.38 mi, -18.67 mi)
[(-7.05 km, -30.05 km)]
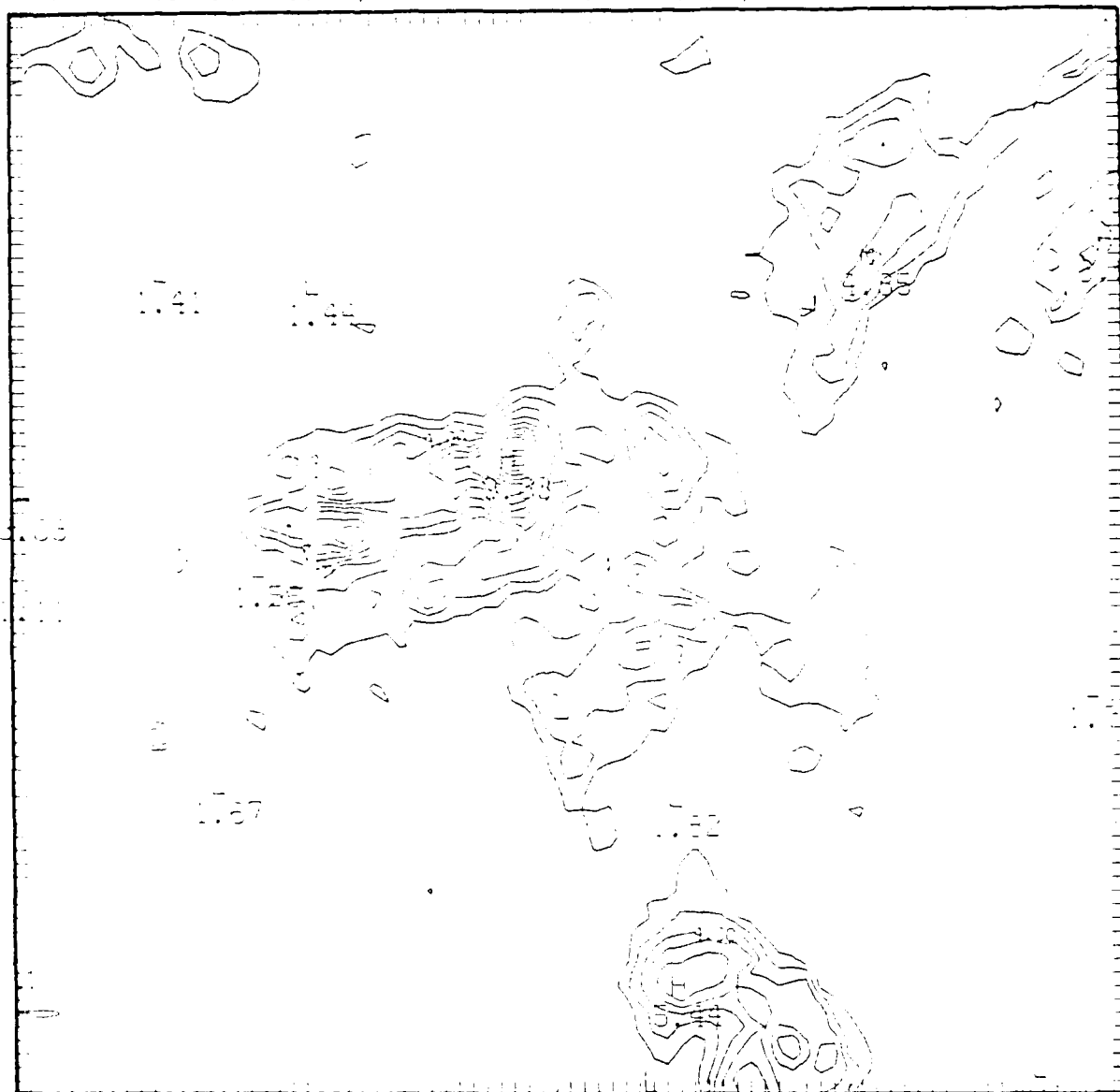
(b) Pulse SD

Figure 5. (continued).

Contour from 1.0 to 4.0 m/s

Contour interval = 0.5 m/s     Mean value = 0.94 m/s

Corner Coordinates w.r.t. CP-2
(11.37 mi, 1.80 mi)
[(18.30 km, 2.90 km)]
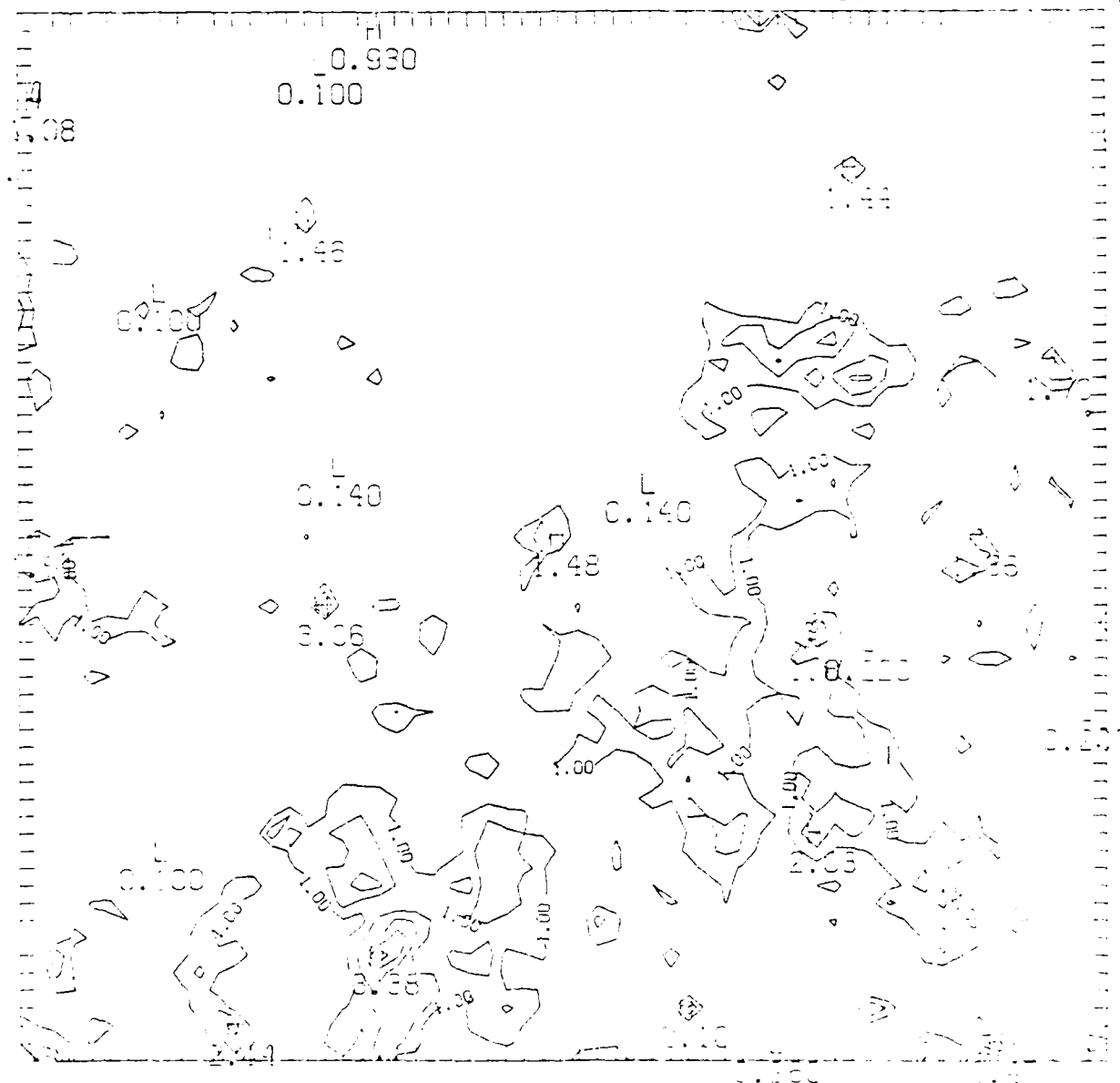


Corner Coordinates w.r.t. CP-2
(3.91 mi, -5.65 mi)
[(6.30 km, -9.10 km)]

(a) From CP-4 radar

Figure 6.   Contour of wind SD at level 7 (0.9 km above ground) for
            14JL1452 microburst from CP-4 and CP-2.  (Large numbers
            correspond to magnitude of highs and lows while smaller
            numbers represent contour values.)

Contour from 1.0 to 4.0 m/s

Contour interval = 0.5 m/s      Mean value = 0.51 m/s      [(18.30 km, 2.90 km)]
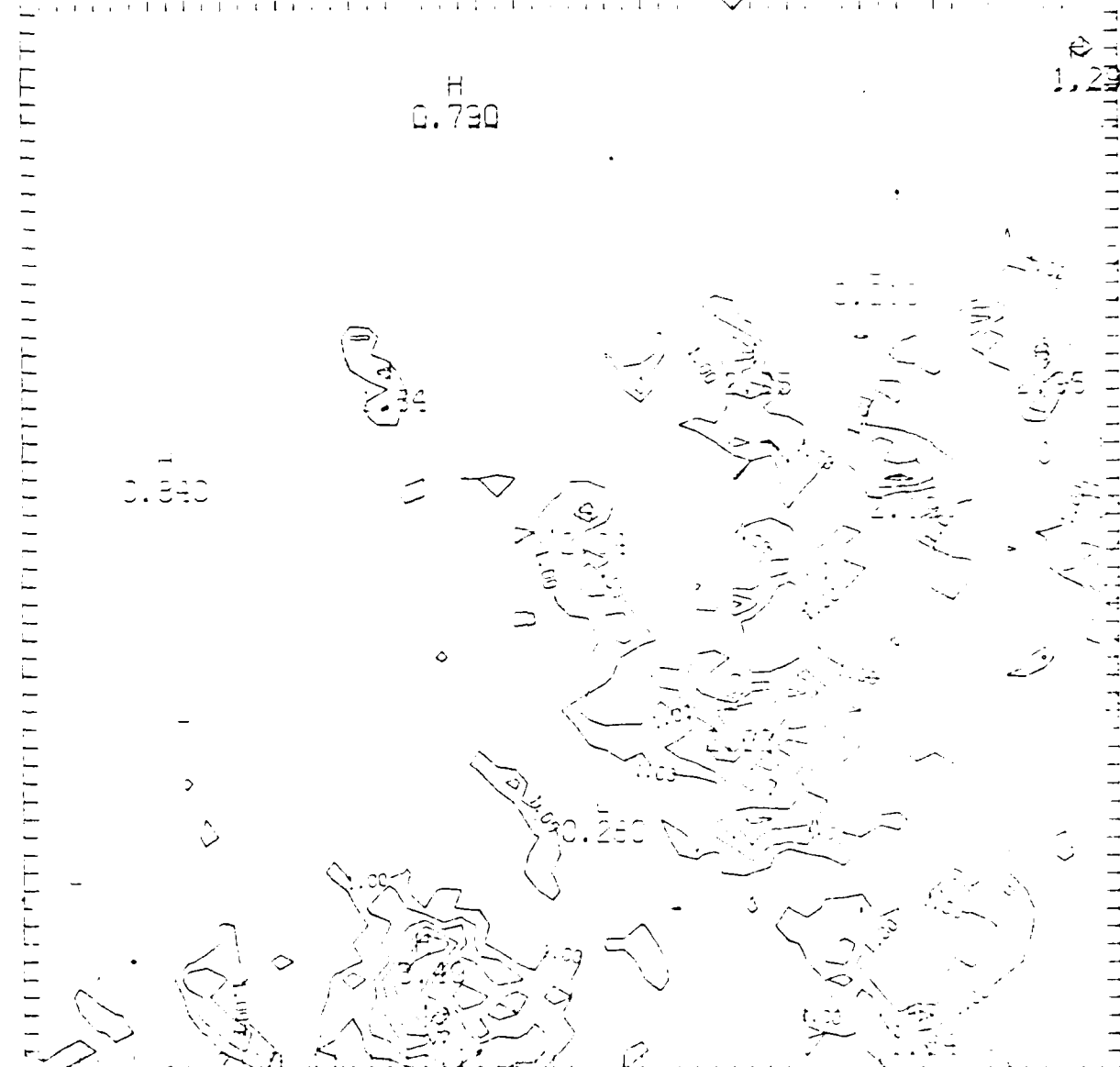


Corner Coordinates w.r.t. CP-2
(3.91 mi, -5.65 mi)
[(6.30 km, -9.10 km)]

(b) From CP-2 radar

Figure 6.   (continued).
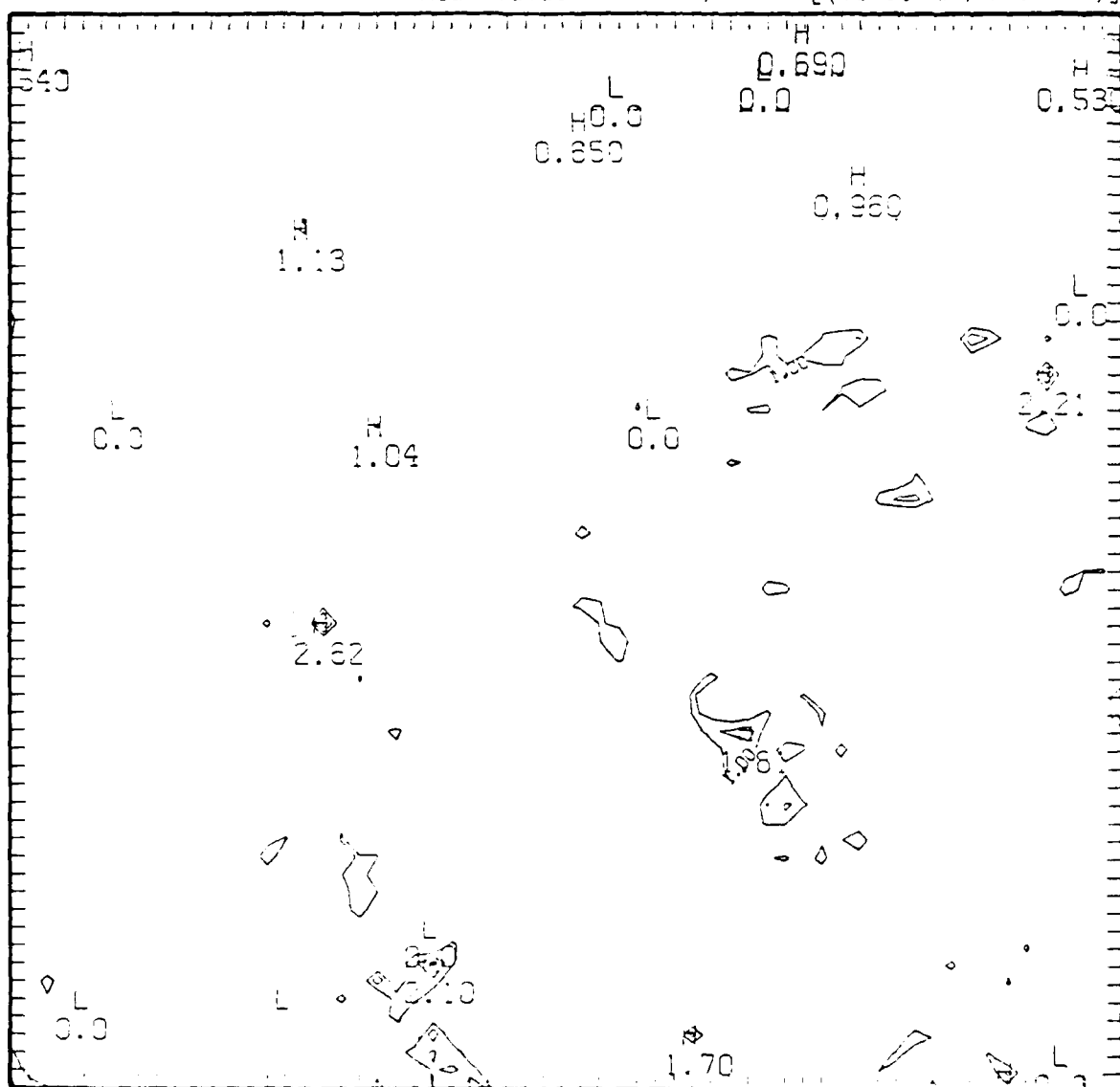
Figure 7.  Contour of wind SD difference between the measurements
from CP-4 and CP-2 radars at level 7 (0.9 km above
ground) for 14JL1452 microburst.  (Large numbers corre-
spond to magnitude of highs and lows while smaller
numbers represent contour values.)

Contour from 3.0 to 10.0 m/s
Contour interval = 0.5 m/s    Mean value = 2.5 m/s
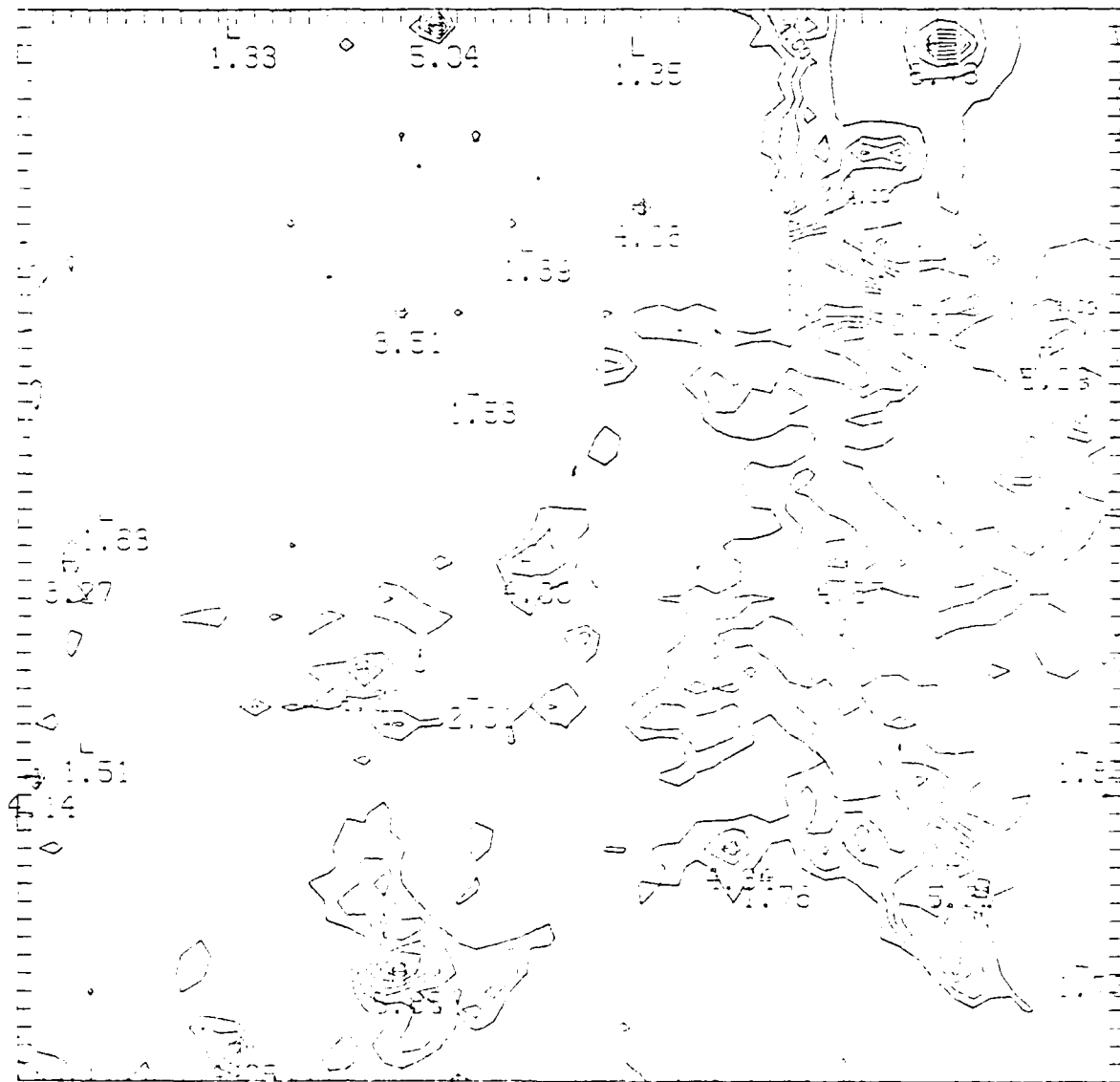
Corner Coordinates w.r.t. CP-2
 (3.91 mi, -5.65 mi)
[(6.30 km, -9.10 km)]

(a) From CP-4 radar

Figure 8.  Contour of pulse SD at level 7 (0.9 km above ground) for
           14JL1452 microburst from CP-4 and CP-2.  (Large numbers
           correspond to magnitude of highs and lows while smaller
           numbers represent contour values.)

Contour from 3.0 to 10.0 m/s
Contour interval = 0.5 m/s    Mean value = 1.9 m/s

Corner Coordinates w.r.t. CP-2
(11.37 mi, 1.80 mi)
[(18.30 km, 2.90 km)]
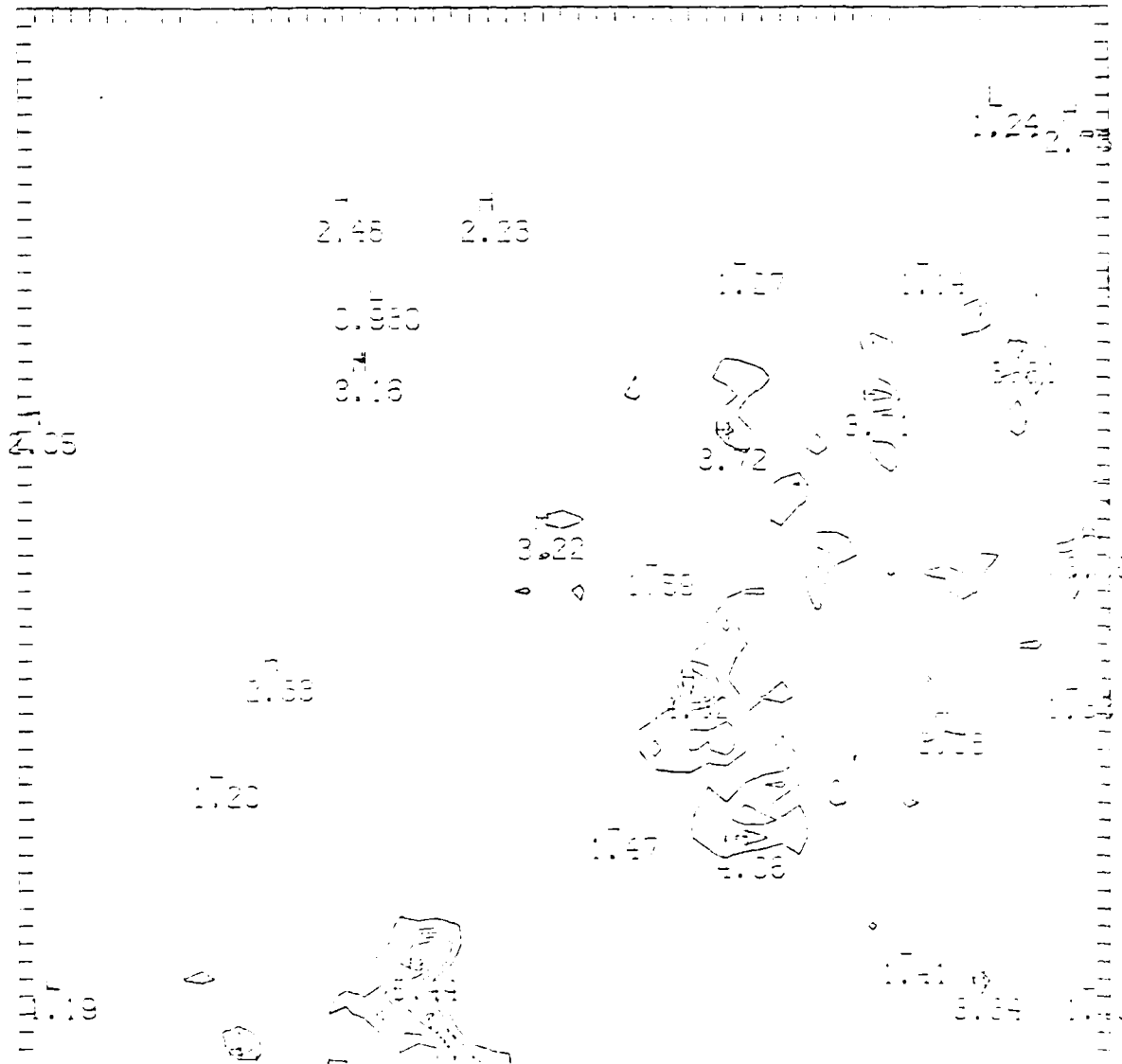


Corner Coordinates w.r.t. CP-2

(3.91 mi, -5.65 mi)
[(6.30 km, -9.10 km)]

(b) From CP-2 radar

Figure 8.  (continued).

21

Figure 9. Contour of pulse SD difference between the measurements from CP-4 and CP-2 radars at level 7 (0.9 km above ground) for 14JL1452 microburst. (Numbers correspond to magnitude of highs and lows.)
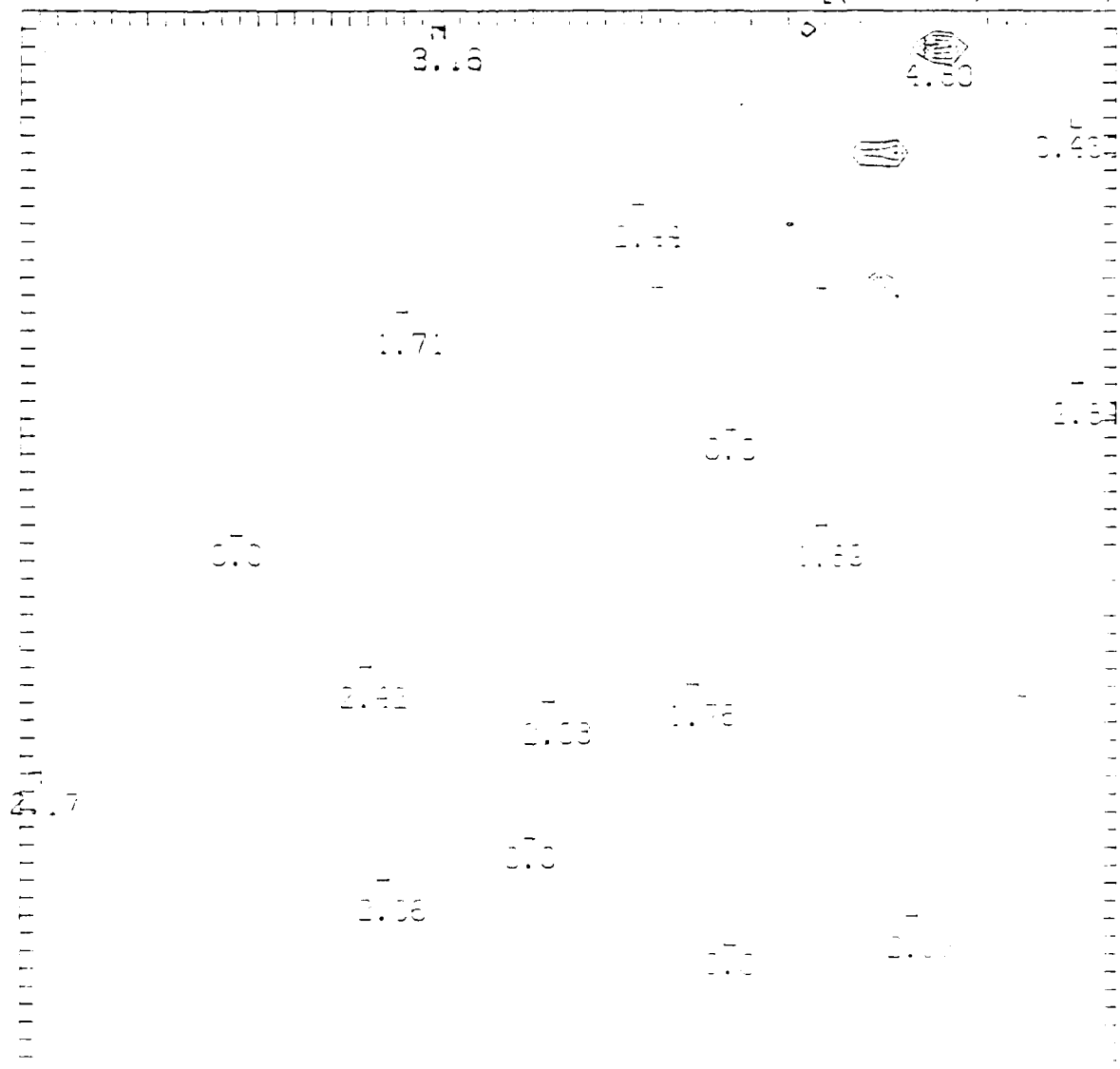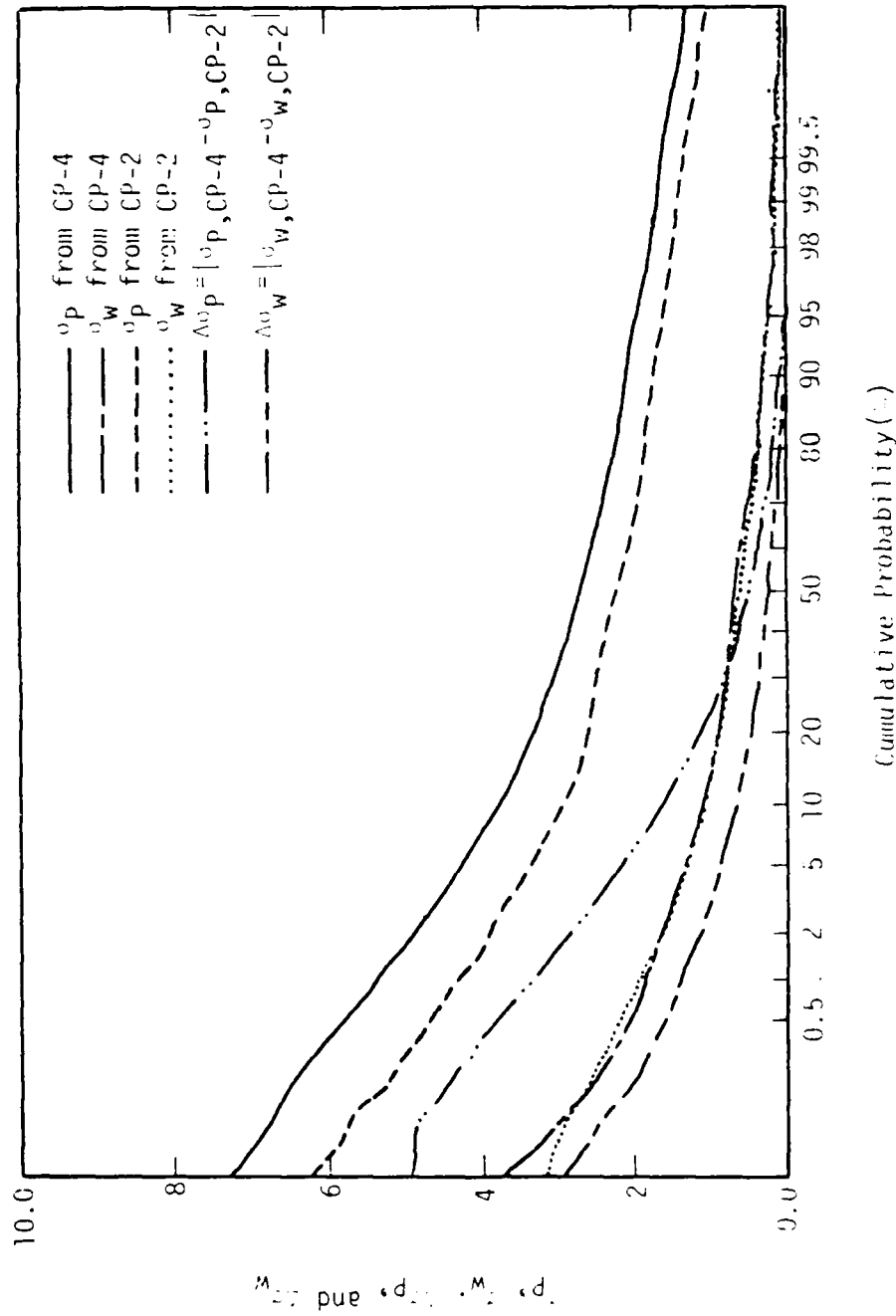
Figure 10. Cumulative probabilities of $\sigma_\rho$, $\sigma_w$, $\Delta\sigma_\rho$, and $\Delta\sigma_w$ for 14JL1452 microburst from both CP-4 and CP-2.

Legend:
- $\sigma_\rho$ from CP-4
- $\sigma_w$ from CP-4
- $\sigma_\rho$ from CP-2
- $\sigma_w$ from CP-2
- $\Delta\sigma_\rho = |\sigma_\rho, CP-4 - \sigma_\rho, CP-2|$
- $\Delta\sigma_w = |\sigma_w, CP-4 - \sigma_w, CP-2|$

Cumulative Probability (%)

$\sigma_\rho$, $\sigma_w$, $\Delta\sigma_\rho$, and $\Delta\sigma_w$

from Figure 11, the background turbulence intensity is significantly decreased by the spectrum width broadening due to wind shear.

The spectrum width broadenings due to the radial wind shear, antenna motion, and the different fall speeds for various sized drops--as defined in Equations 5, 9, and 10 respectively--were evaluated and subtracted from the total spectrum width. In most situations, the broadening from both the antenna motion and the different fall speeds is small compared to that from the radial wind shear. The cumulative probabilities of the spectrum width contribution due to the radial wind shear, $\sigma_s$, and the microburst turbulence, $\sigma_t$, are shown in Figure 11 for the 14JL1452 measurement from both the the CP-4 and CP-2 radars. Microburst turbulence intensity, $\sigma_t$, derived from the CP-4 radar is consistent with that from the CP-2 radar over 80 percent of the full volume. This, in turn, suggests that the microburst turbulence is essentially isotropic turbulence. It is interesting to note that the cumulative probability distribution of the wind SD, $\sigma_w$ (see Figure 10), is very close to that of the spectrum width broadening due to the radial wind shear shown in Figure 11.

Similar analyses are shown in Figures 12 and 13 for the 5AU1847 and 30JN1823 microbursts, respectively. Among the three microbursts analyzed, the JAWS June 30 microburst contains the strongest turbulence, whereas the August 5 microburst has the most complicated wind profile structure.

Finally, cumulative probabilities of the radial wind shear terms $K_r$, $K_\theta$, and $K_\phi$, as defined in Equation 6, for CP-4 and CP-2, are shown in Figures 14 through 17 for the JAWS microbursts. It is seen that the microburst contains larger shear in the elevation direction than in the azimuthal direction. In the July 14 microburst, only 5 percent of all azimuthal shears are larger than $5 \times 10^{-3}$ 1/sec, while 35 percent of all elevational shears are in excess of 5 $\times 10^{-3}$ 1/sec. In the August 5 case, 10 percent of the azimuthal shears are larger than $10^{-2}$ 1/sec and over 30 percent of the elevational shears are higher than $10^{-2}$ 1/sec. The radial velocity shear in the elevational direction of the JAWS microburst is larger than twice the values associated with the storms investigated by Istok (1981). The difference is probably due to the strong localized wind shear inherent in microburst storms which are a mixture of an atmospheric boundary layer and downburst flow. An additional explanation is that Istok's grids are much coarser than JAWS data. Comparing the wind shear terms shown in Figures 14 through 17, one can easily see that the August 5 microburst contains the strongest wind shear effects of the three microbursts analyzed. The August 5 microburst is, therefore, recommended as a good scenario for use in flight simulators for training avoidance and operational procedures if penetration is unavoidable.


2.3  Comparison of Radar Data and Aircraft Data

A comparison between the turbulence intensities measured simultaneously by JAWS Doppler radar and aircraft has been made. Using a ground-based radar system and an instrumented aircraft, turbulence characteristics associated with thunderstorms at high altitudes (>3500 m above ground level) were detected and studied by Burnham and Lee (1969), Lee (1977 and 1981), and Bohne (1981 and 1985). A comparison of some results from these previous studies

24
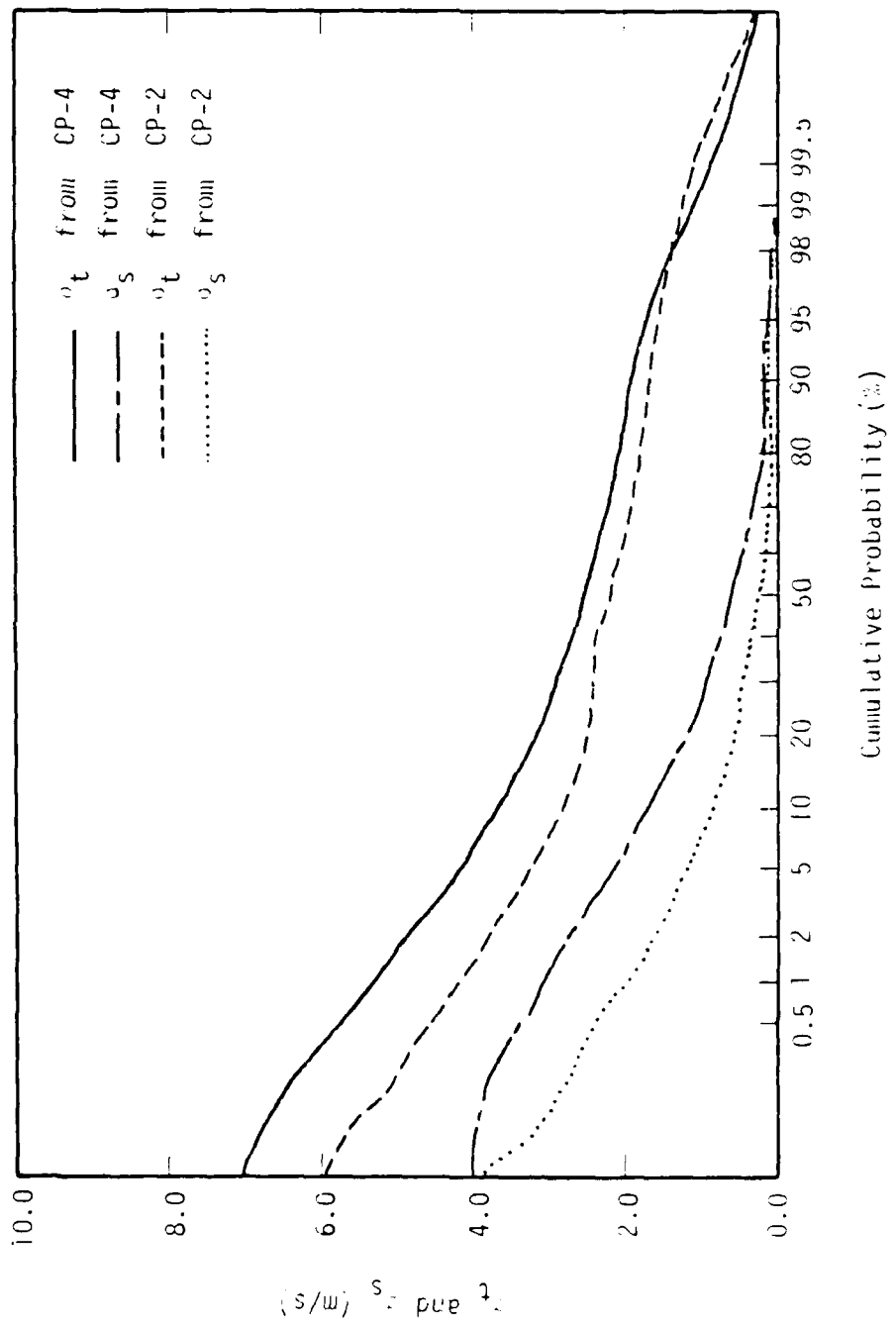
Figure 11. Cumulative probabilities of $\sigma_t$ and $\sigma_w$ for 14JL1452 microburst from both CP-4 and CP-2.
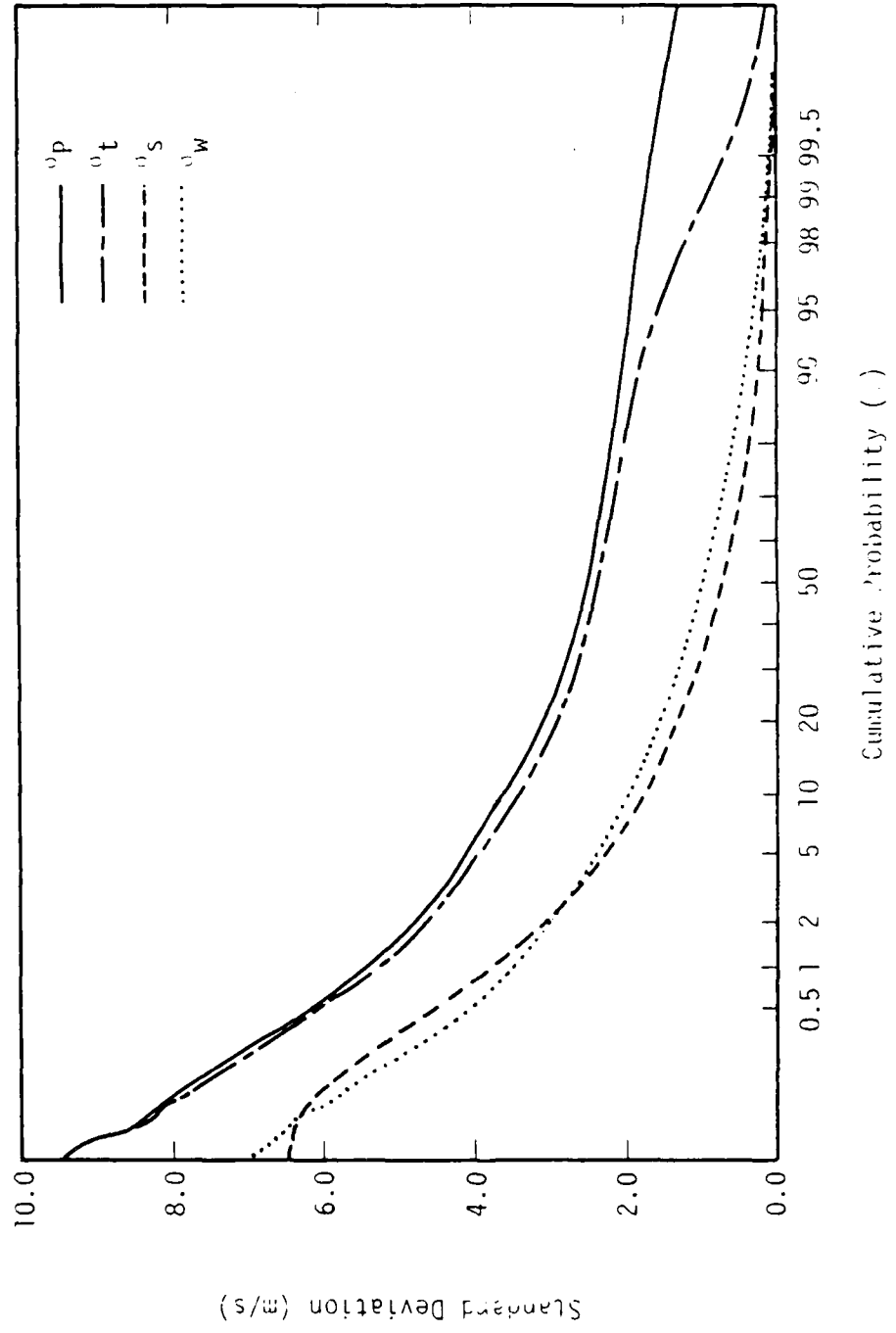
Figure 12. Cumulative probabilities of $\sigma_p$, $\sigma_t$, $\sigma_s$, and $\sigma_w$ for JAWS 847 microburst from CP-4.

26
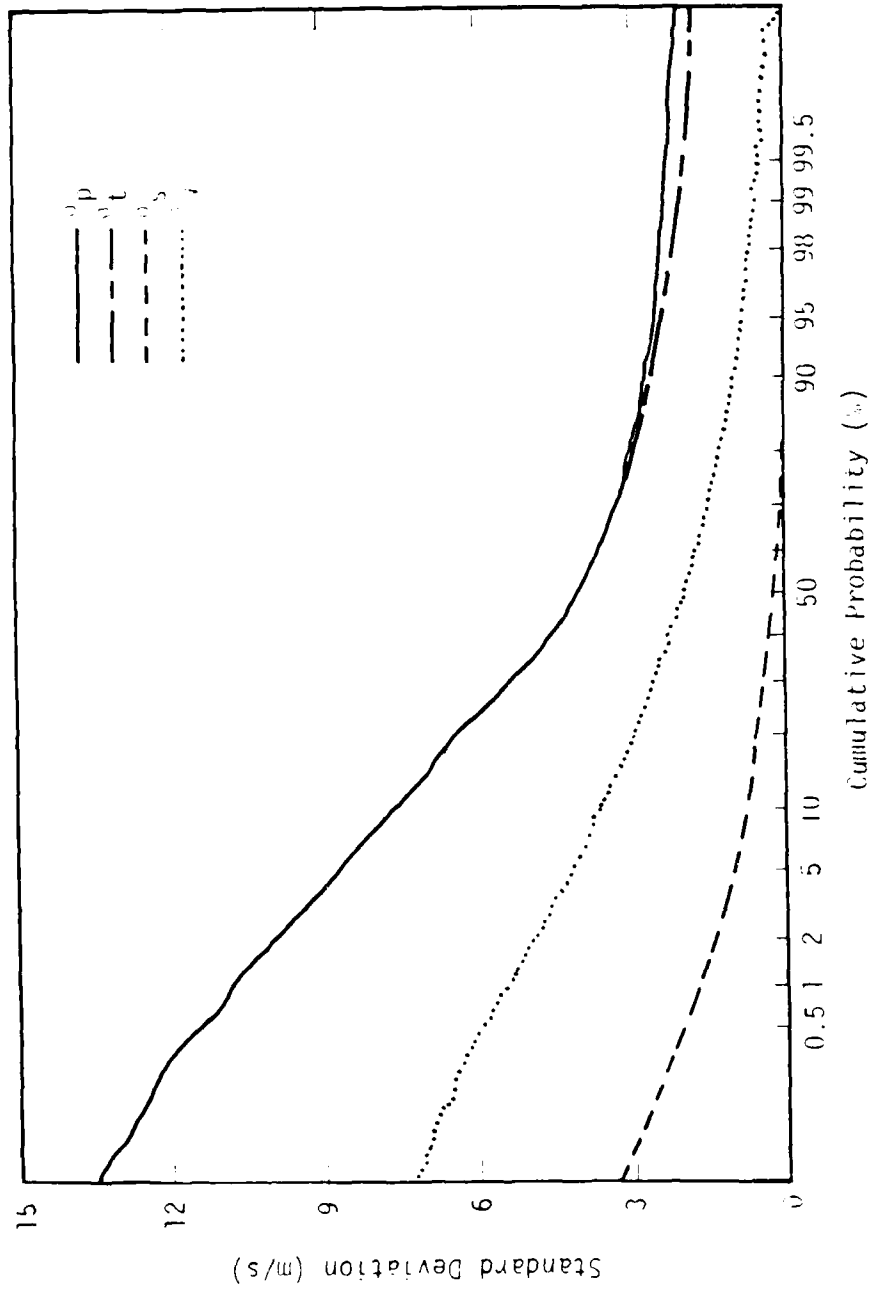
Figure 13. Cumulative probabilities of $\sigma_p$, $\sigma_t$, $\sigma_s$, and $\sigma_w$ for 30JUN1823 microburst from CP-4.
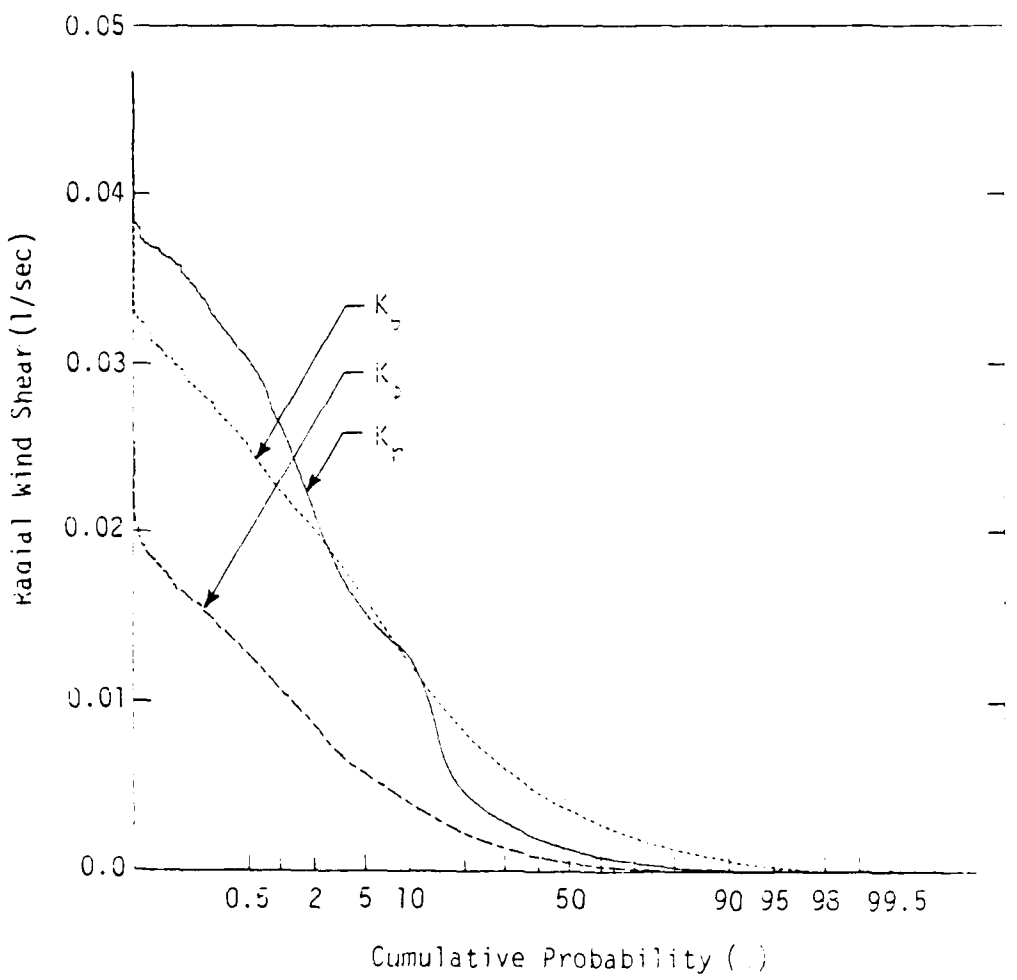
Figure 14. Cumulative probabilities of radial wind shear terms, $K_r$, $K_z$, and $K_y$, for 14JL1452 microburst for CP-4.

Figure 15.  Cumulative probabilities of radial wind shear terms,
$K_r$, $K_{\dot{}}$, and $K_{\cdot}$, for 14JL1452 microburst for CP-2.
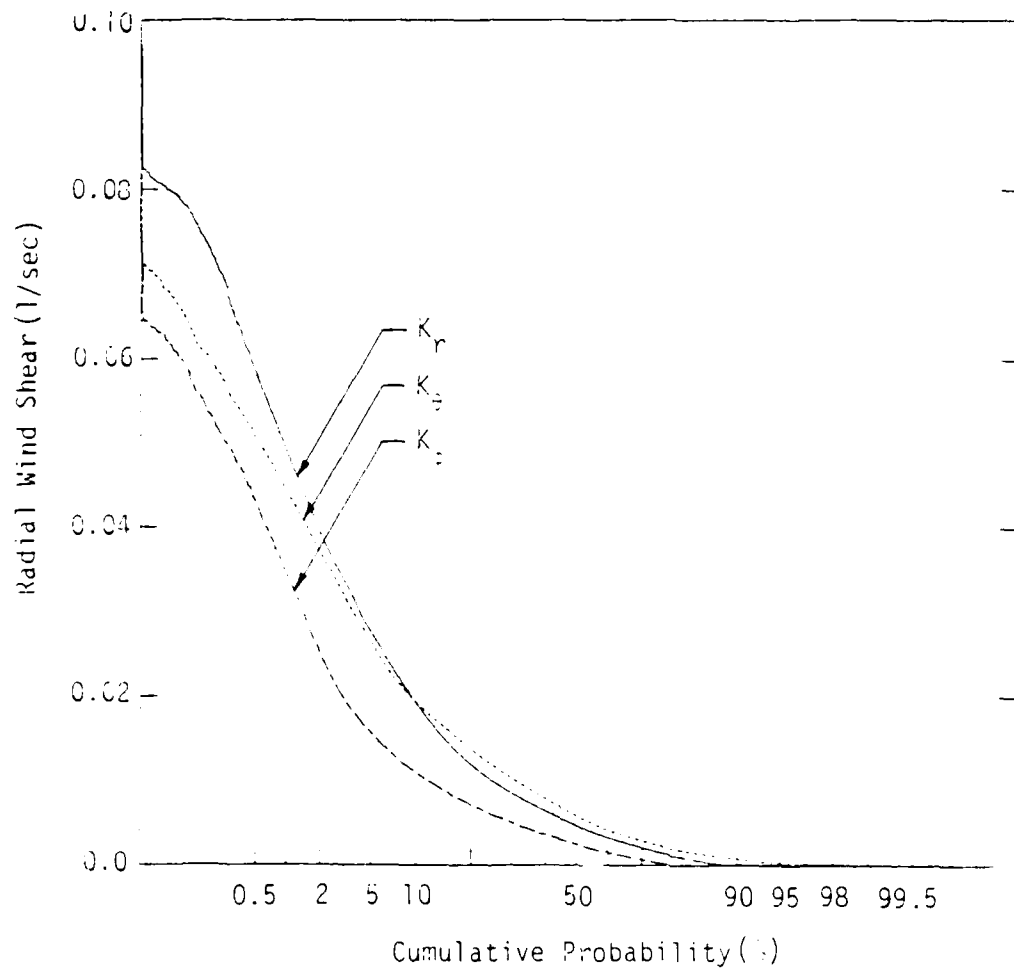
Figure 16.   Cumulative probabilities of radial wind shear terms,
             $K_r$, $K_\phi$, and $K_z$, for 5AU1847 microburst for CP-4.
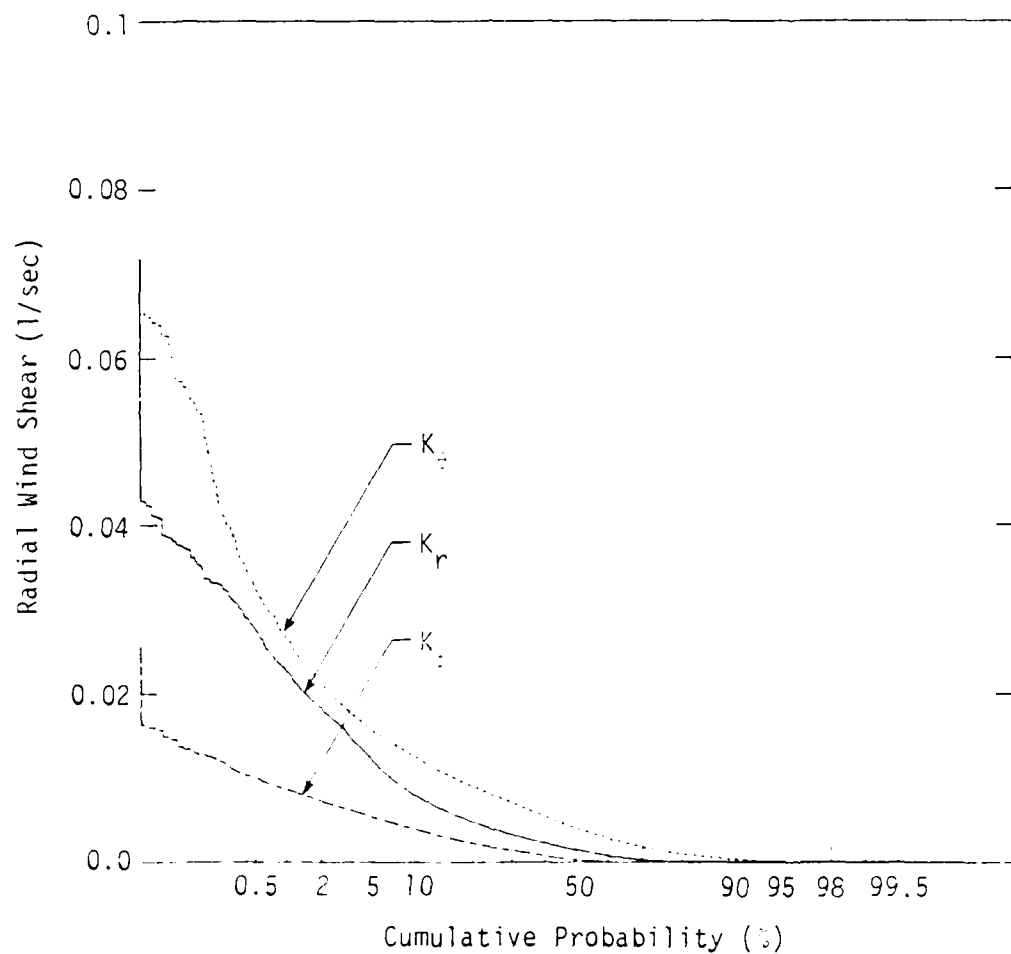
Figure 17.  Cumulative probabilities of radial wind shear terms, $K_r$, $K_z$, and $K_\theta$ for 30JN1823 microburst for CP-4.

with the current experimental measurements of microbursts at low altitudes (<2000 m above ground level) is made in this section.

During the JAWS field experiment, the NASA B-57B gust gradient aircraft was used to measure turbulence along paths near microburst storms. Unfortunately, because of aircraft control restrictions during storms in the Stapleton airport area, very few of these research aircraft flights coincided with the Doppler radar measurements. Table 3 shows the gust gradient flights of the NASA B-57B aircraft during JAWS experiment. Among these flights, only Runs 23, 24, and 25 for Flight 6 coincide with Doppler data. These data were measured during the JAWS July 14 microburst. Figure 18 shows the relative positions of the JAWS microburst and the aircraft flight paths for Runs 23, 24, and 25. Run 24 was flown through the microburst almost simultaneously with the JAWS radar measurement. The run started at 14:50:50 MDT and lasted for 87 seconds. Run 23 was flown through the field about 4 minutes earlier than the JAWS measurment while Run 25 was flown approximately 2 minutes later than the radar scan and slightly outside of the microburst measurement volume.

Figures 19 and 20 depict the flight path information for Runs 24 and 23, respectively. Both runs are flown through the field at approximately 450 ft (150 m) above the ground. Figure 21 compares the total spectrum width, $\sigma_D$, with the calculated turbulence intensities from Run 24 of the NASA B-57B measurements. The plotted longitudinal, lateral, and vertical SD's from the aircraft data are relative to the body axis of the aircraft. The total spectrum width (without subtracting any broadening) is about five times the turbulence intensity obtained from the aircraft. This agrees with the reported results of Robison and Konrad (1974) and Lhermitte (1968). Since the SD's from the aircraft measurements are relative to 2 to 3 second means, low turbulence intensity values are expected.

As mentioned earlier, the JAWS microburst turbulence intensity, $\sigma_t$, can be calculated by subtracting the other spectrum width broadening effects from the total spectrum width. Comparison of the $\sigma_t$ with the calculated SD's from the NASA B-57B measurement is shown in Figure 22 for Run 24 and in Figure 23 for Run 23. The wind standard deviation, $\sigma_w$, from the radar is also shown in the figures. The $\sigma_w$ is very consistent with the aircraft measurement. However, the microburst $\sigma_t$ is about three times that of the aircraft data. A comparison between the turbulence intensities obtained from a NOAA/WPL lidar and the NASA B-57B aircraft was reported by Huang et al. (1985). One of their comparisons is shown in Figure 24. The lidar spectrum width is again about 4 to 5 times that of the aircraft-measured turbulence intensity. Bohne (1981) reported another comparison between a turbulence variance of a so-called "true" vertical gust velocity which was derived from an aircraft-measured vertical gust velocity and a Doppler spectrum variance (shown in Figure 25). The turbulence variance of the "true" vertical gust velocity is relative to the mean of the whole run. The correlation coefficient of these two variances is 0.891.

Doppler radar and aircraft, of course, use different methods for measuring turbulence information. The former measures turbulence contained in a full three-dimensional volume in space whereas the latter measures information along the aircraft trajectory, i.e., a line in space. Thus, turbulence intensity meaured by the Doppler radar will, in general, be larger as shown in Figures 22 and 23. A better understanding of the relationship

TABLE 3.  Gust Gradient Flights of NASA B-57B Aircraft During JAWS 1982.

| Flight | Date | Start (MDT) | End (MDT) | Comments |
|--------|------|-------------|-----------|----------|
| 1 | 7/07 | 15:41:38 | 15:59:39 | Landmark familiarization flight |
| 2 | 7/08 | 14:49:11 | 16:40:35 | Light to moderate turbulence |
| 3 | 7/09 | 13:17:10 | 15:42:34 | Light to moderate turbulence with data correlation with JAWS 02 and 03 |
| 4 | 7/11 | 14:46:07 | 17:02:44 | Moderate turbulence and lightning |
| 5 | 7/13 | 15:20:18 | 16:44:56 | ILS approaches to Stapleton in light turbulence |
| 6 | 7/14 | 13:41:13 | 15:55:21 | Severe turbulence and outflows visible on radar |
| 7 | 7/15 | 14:08:13 | 16:26:20 | Outflows, severe turbulence, and ILS approaches |
| 8 | 7/17 | 15:49:35 | 17:17:56 | Rain with light to moderate turbulence |
| 9 | 7/20 | 15:59:30 | 18:35:52 | Light to moderate turbulence with some ILS approaches |
| 10 | 7/21 | 16:05:05 | 18:04:40 | Good downburst with moderate to severe turbulence |
| 11 | 7/22 | 13:36:09 | 15:24:45 | Light to moderate turbulence |
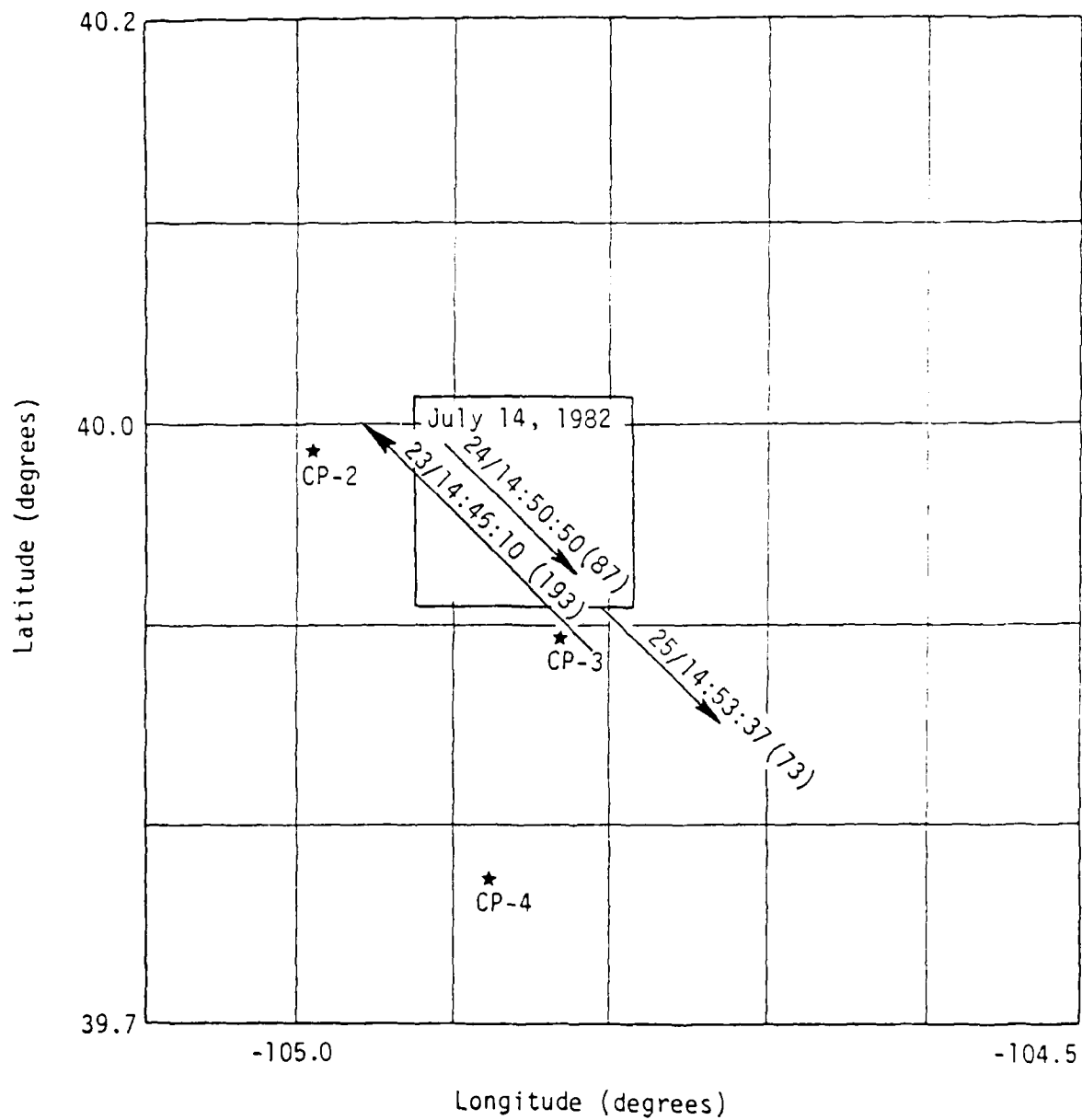
Figure 18. Relative positions of 14JL1452 microburst and flight paths of Runs 23, 24, and 25 in Flight 6 of NASA B-57B aircraft.

Date: July 14, 1982
Time: 14:50:50(MDT)
Duration: 87 seconds

Wind Direction Relative
to Flight Path
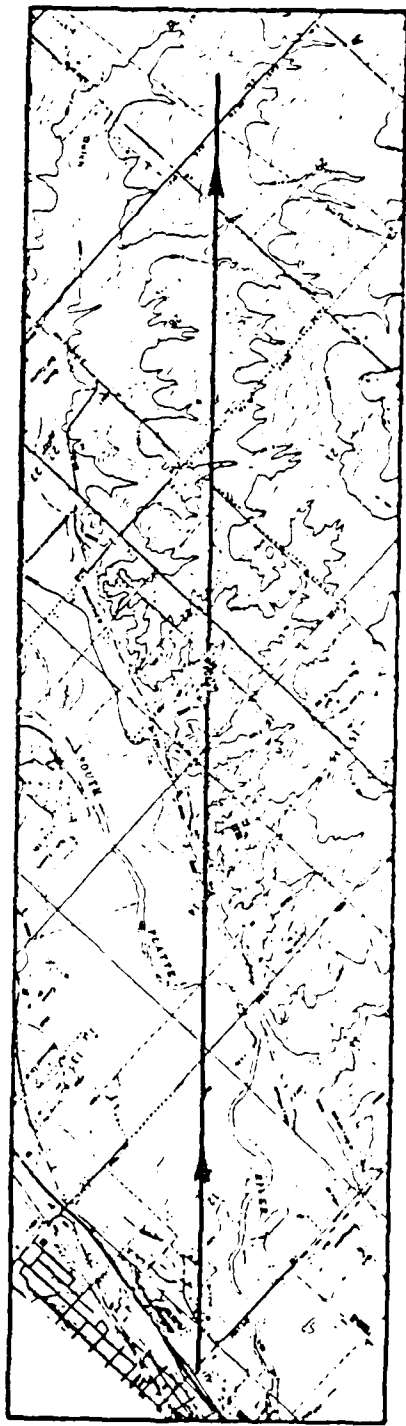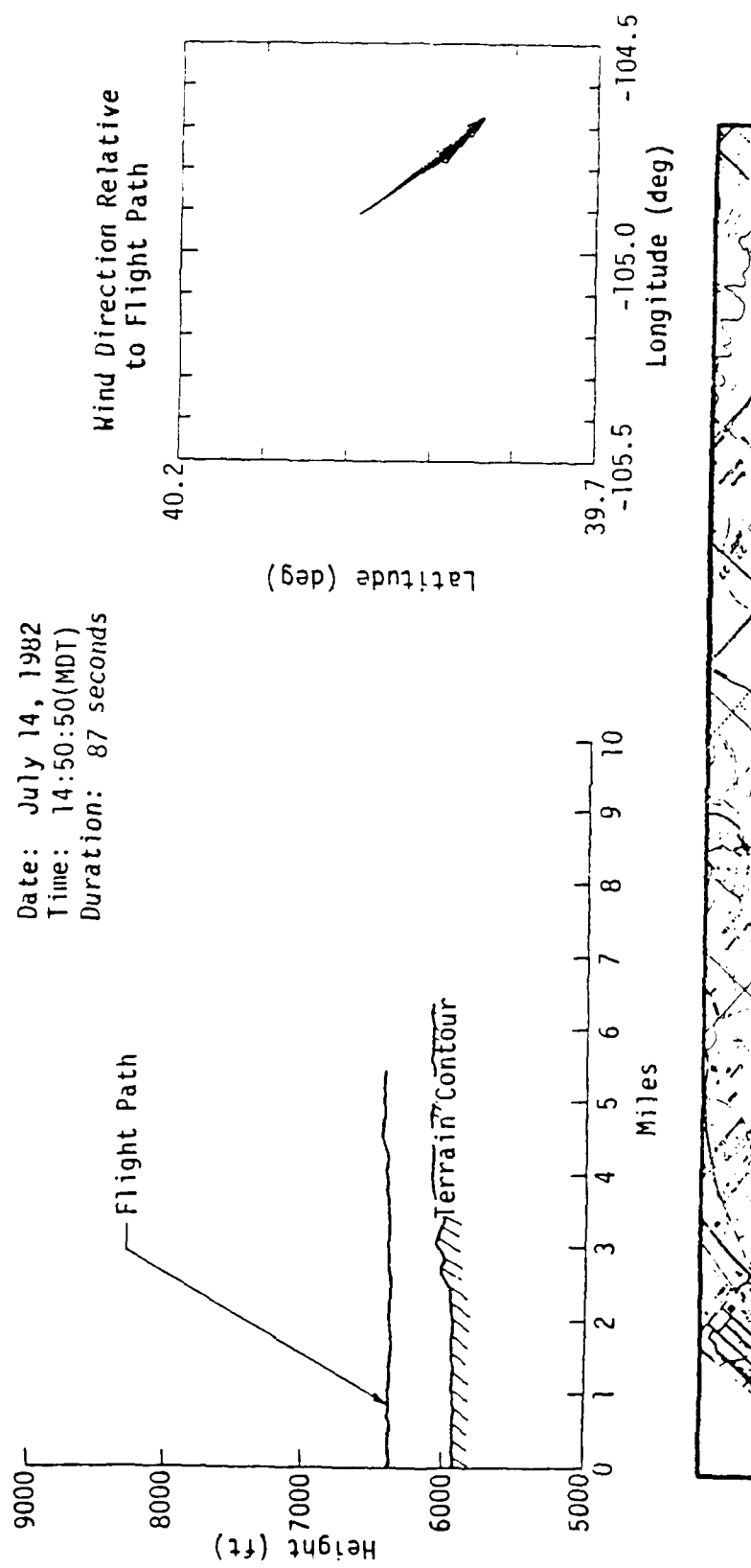
Figure 19. Flight path information, Run 24, Flight 6.
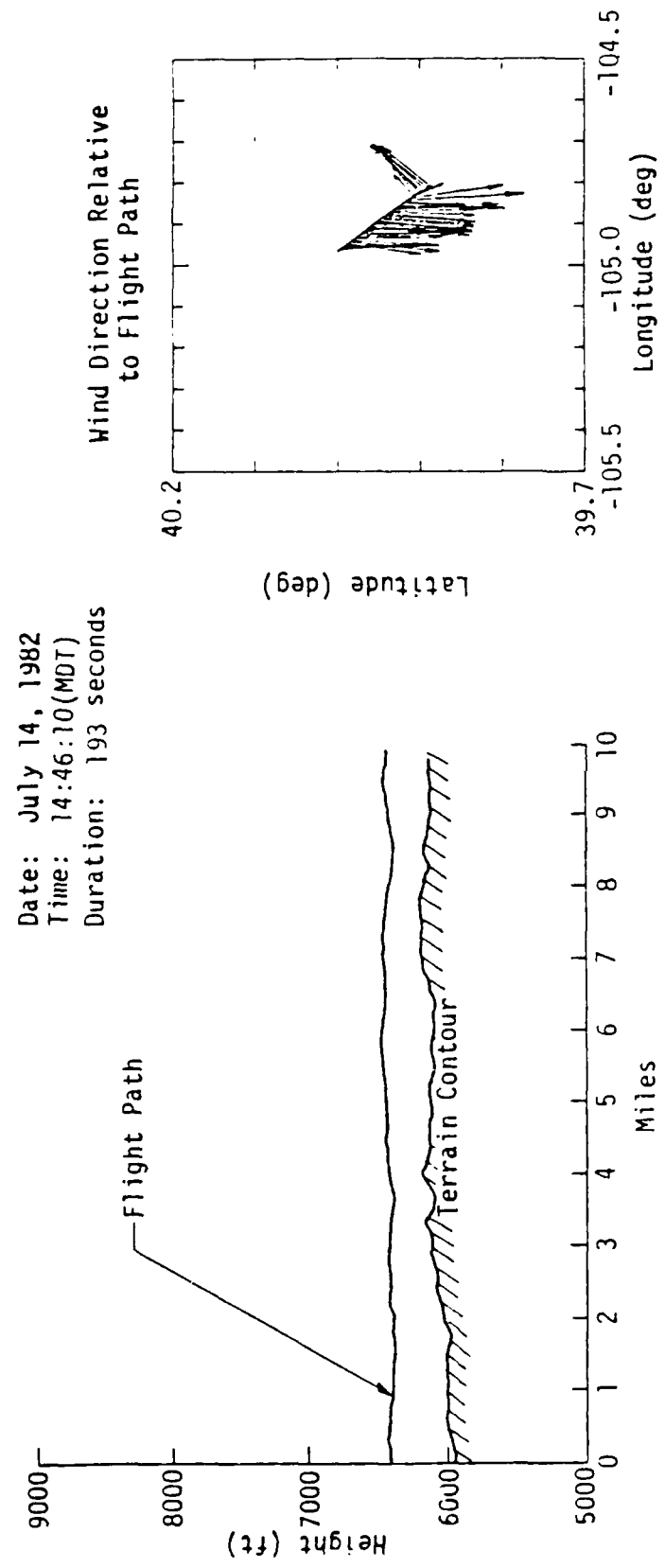
Figure 20. Flight path information, Run 23, Flight 6.
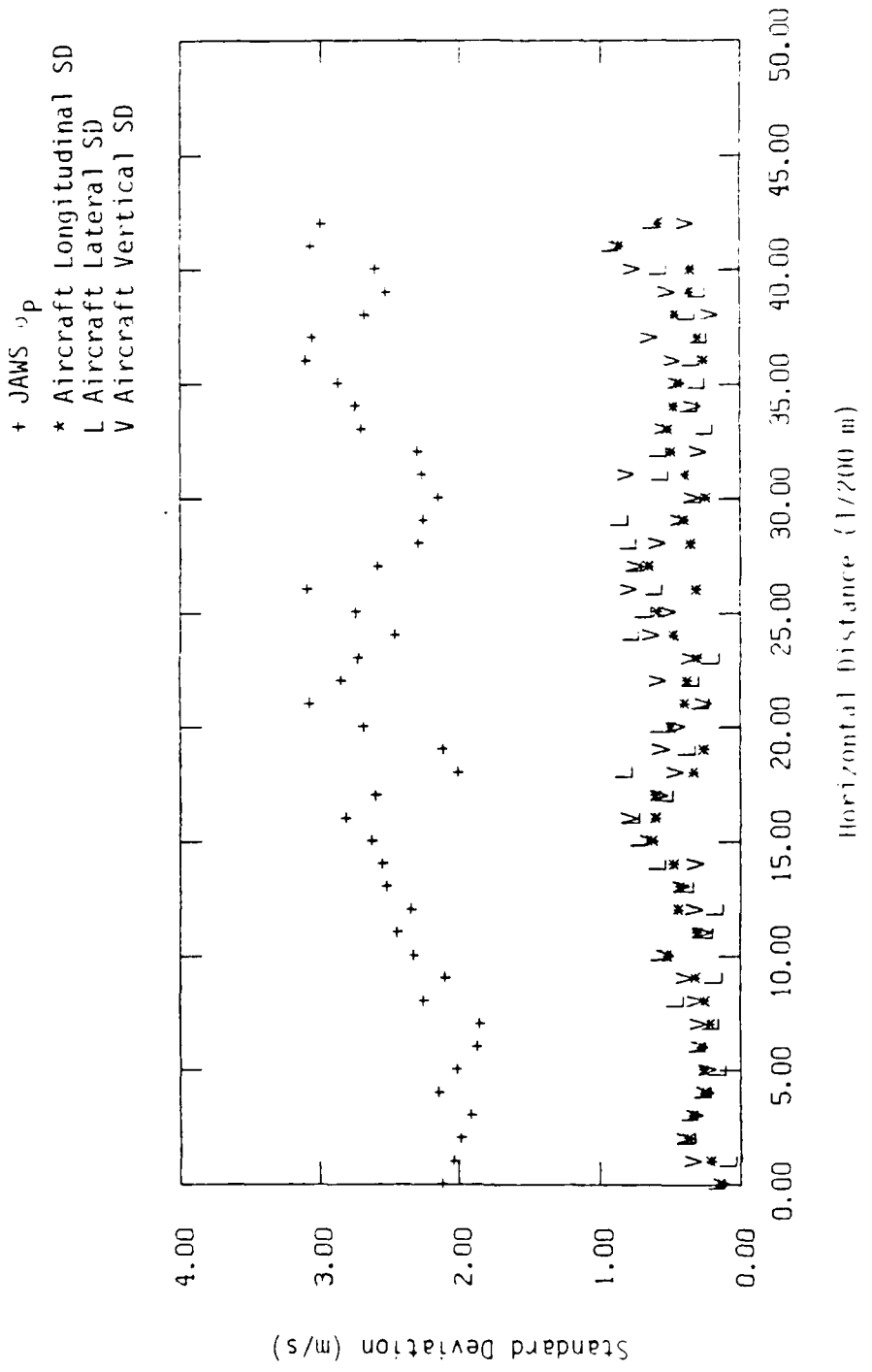
Figure 21. Comparison of $\sigma_p$ with calculated turbulence intensities from NASA B-57B aircraft measurement in Run 24.
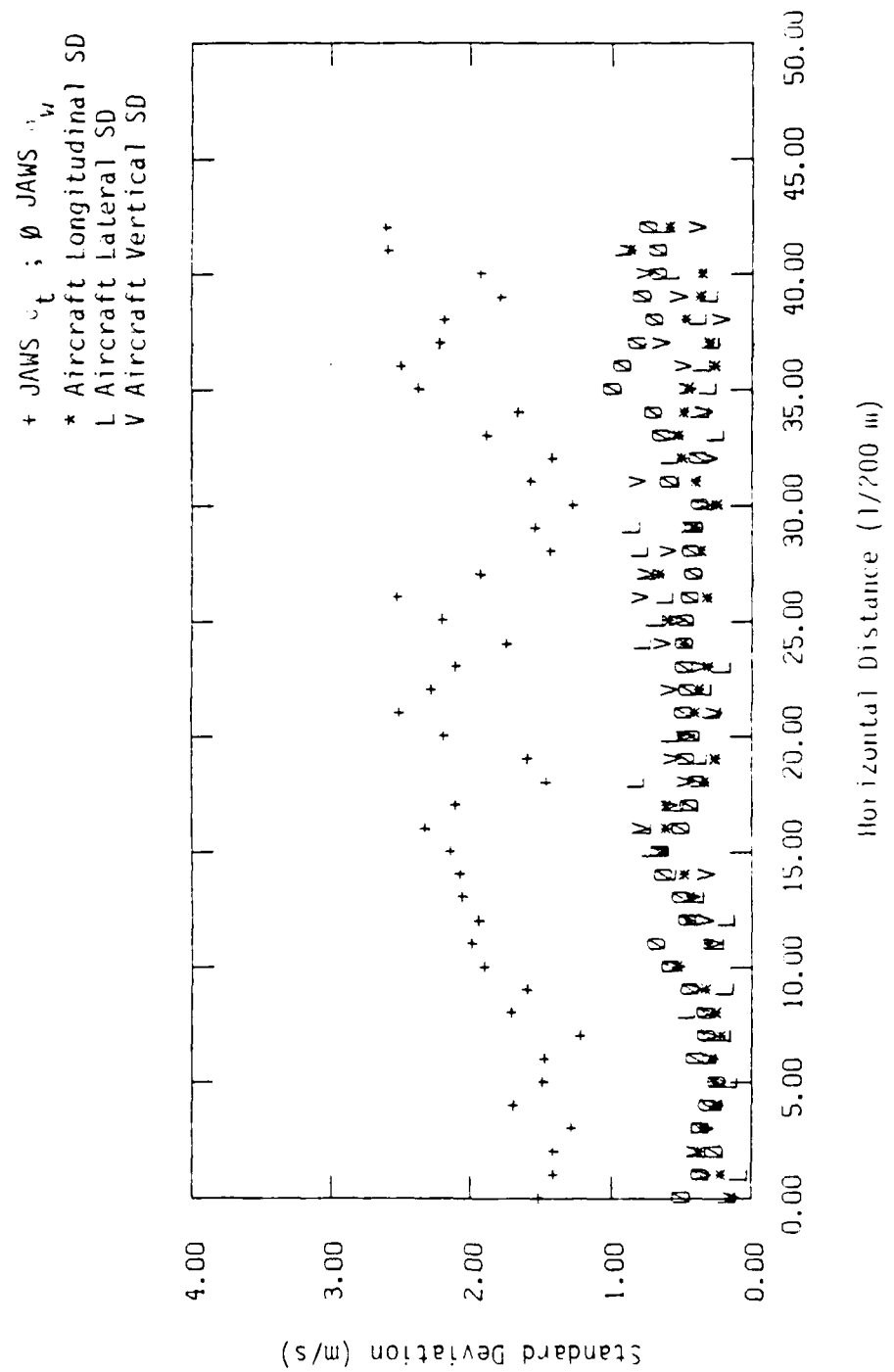
Figure 22. Comparison of $\sigma_t$ and $\sigma_w$ with calculated turbulence intensities from NASA B-57B aircraft measurement in Run 24.

38
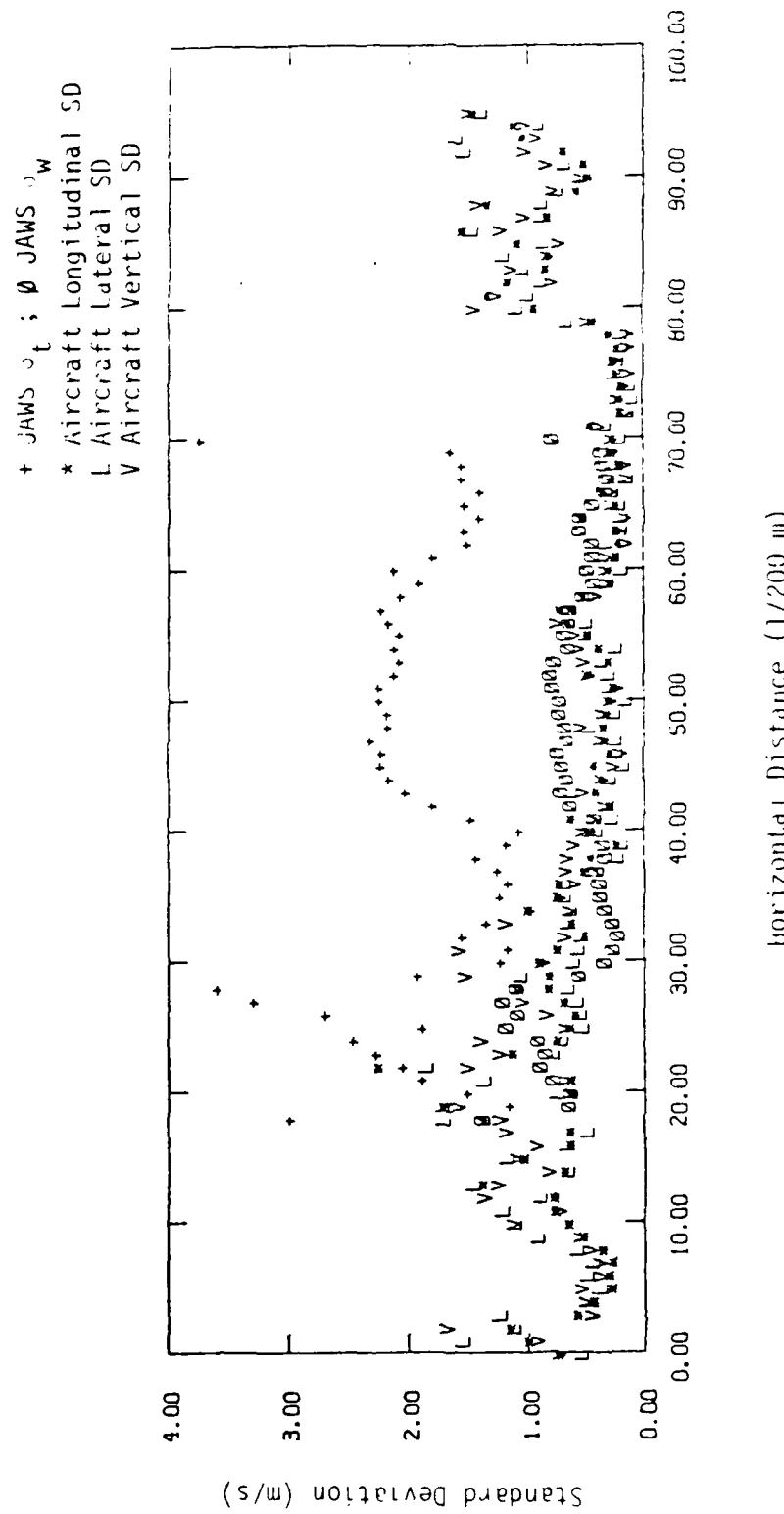
Figure 23. Comparison of $\sigma_t$ and $\sigma_w$ with calculated turbulence intensities from NASA B-57B aircraft measurement in Run 23.
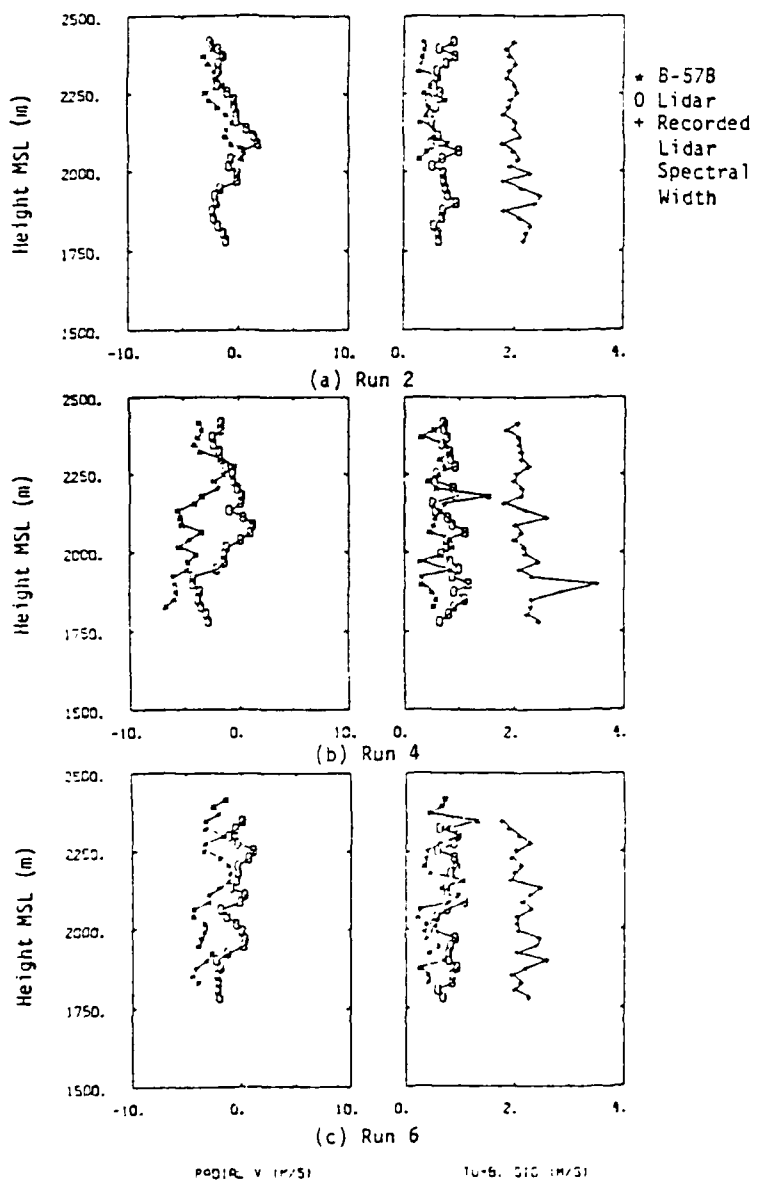
Figure 24. Comparison of radial mean wind velocity, calculated turbulence intensity, and lidar spectral width between aircraft measurement and lidar measurement on February 7, 1984 (Huang and Frost 1984).
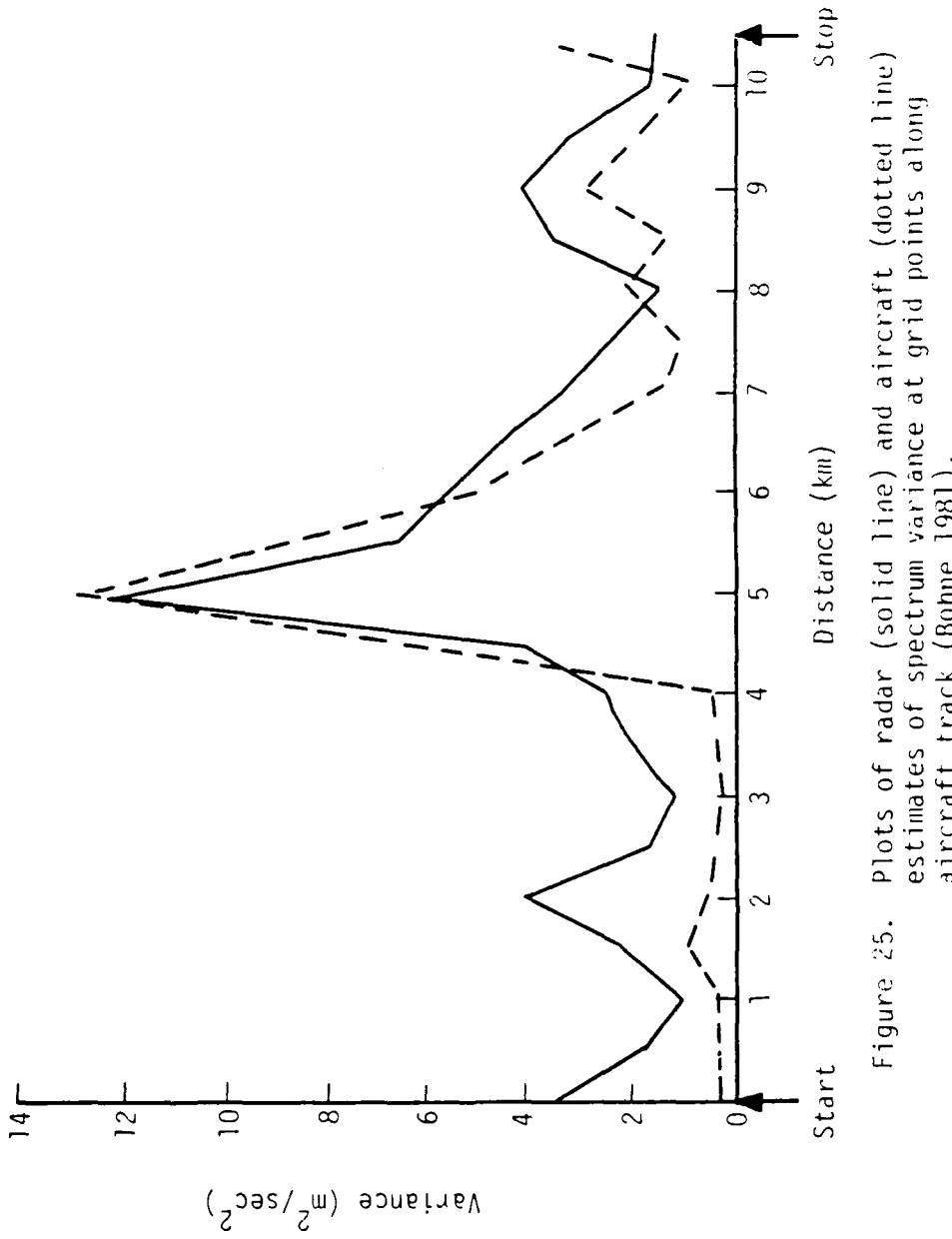
Figure 25.  Plots of radar (solid line) and aircraft (dotted line) estimates of spectrum variance at grid points along aircraft track (Bohne 1981).

41

between these two measurements is required in order to perfect a turbulence model to support the FAA and NCAR JAWS wind shear data sets. Also, this understanding will be highly beneficial to the development of terminal Doppler wind shear algorithms. More investigations, however, must be conducted to fully address this issue.

## 2.4  Microburst Turbulence Parameters

The important parameters for modeling turbulence are the turbulence intensity, length scale, and spectrum. The Dryden spectrum is currently recommended by the FAA AC-120-41 for wind shear turbulence modeling. Table 4 shows the turbulence intensity and the turbulence length scale suggested in this Advisory Circular for input to this spectrum. Both turbulence intensity and length scale are represented as a function of height only. In addition to the height, turbulence parameters associated with a microburst should be a function of the mean wind direction and the radial distance relative to the microburst center. In this study, microburst turbulence is assumed to be locally isotropic, at least for the smaller scales of interest here but not homogeneous on the large scale. Figure 26 schematically shows the top view of a microburst. MC represents the center of the microburst; circles a, b, c, and d designate locations at different radial distances from the center; and 1, 2, 3 ... A, B, C represent twelve directions emanating radially from the microburst center. The arrows represent the quasi-steady mean wind direction at ground level for JAWS July 14, June 30, and August 5 microbursts, respectively. Coordinates of the three microburst centers relative to the CP-2 radar are listed in Table 5.

### 2.4.1  Turbulence Intensity

The profiles of $\sigma_t/V$, which is the microburst turbulence intensity normalized by the local quasi-steady mean wind, at four radial distances 4, 8, 12, and 16 times the data set grid interval from the microburst center of the July 14 measurement are shown in Figure 27. Although the data are highly scattered, a characteristic trend is discernible. To more clearly understand this trend and to provide a functional relationship between the turbulence intensity, $\sigma_t/V$, radial distance from MC, and height above ground, a curve-fitting technique was applied.

The twelve directions given in Figure 26 were collected such as to divide the field into quarters. The directional dependence of the turbulence intensity on the direction of the quasi-steady mean wind could then be studied. The profile $\sigma_t/V$ in each quarter is then curve-fitted by the method of least squares (see Figure 28). Comparison of the profiles at various radial distances shows that the normalized turbulence intensity has higher variations along the mean wind direction (quarters, (3,4,5) and (9,A,B)) than the direction normal to the mean wind (quarters, (C,1,2) and (6,7,8)).

The $\sigma_t/V$ profiles at the various radial distances in a direction normal to the mean wind (quarters (C,1,2) and (6,7,8)) converge to a small value at radial distances greater than about four times the horizontal grid interval from the MC. However, the $\sigma_t/V$ profiles in the upwind direction (quarter (3,4,5)) increases with radial distances especially at lower levels, and then attains a maximum value at radial distance over 15 times the grid interval

TABLE 4.  FAA Turbulence Model in AC-120-41.

| Altitude (feet) | RMS Intensities (kts) | | | Scale Lengths (ft) | | |
|---|---|---|---|---|---|---|
| | Long | Lat | Vert | Long | Lat | Vert |
| 20 | 3.40 | 2.70 | 2.34 | 105.7 | 49.7 | 10.4 |
| 100 | 4.05 | 3.46 | 3.53 | 216.7 | 134.2 | 53.0 |
| 200 | 4.43 | 3.95 | 4.35 | 306.5 | 213.5 | 106.0 |
| 400 | 4.85 | 4.50 | 5.36 | 433.5 | 339.6 | 212.0 |
| 600 | 5.11 | 4.86 | 6.05 | 530.9 | 445.6 | 318.0 |
| 1500 | 5.74 | 5.78 | 7.94 | 840.9 | 824.5 | 795.3 |

$$\sigma_u = 2.33 \ z^{0.12} \qquad L_u = 21.7 \ z^{0.5}$$

$$\sigma_v = 1.56 \ z^{0.18} \qquad L_v = 4.2 \ z^{0.73}$$

$$\sigma_w = 0.98 \ z^{0.28} \qquad L_w = 0.53 \ z^{1.0}$$

TABLE 5.  Center of JAWS Microbursts.

| Data Sets | Coordinates of Microburst Center w.r.t. CP-2 | |
|---|---|---|
| | (Mile) | (Km) |
| August 5, 1982 | (-1.03, -14.94) | (-1.65, -24.05) |
| June 30, 1982 | (9.63, -11.18) | (15.50, -18.00) |
| July 14, 1982 | (8.76, -2.42) | (14.10, -3.90) |
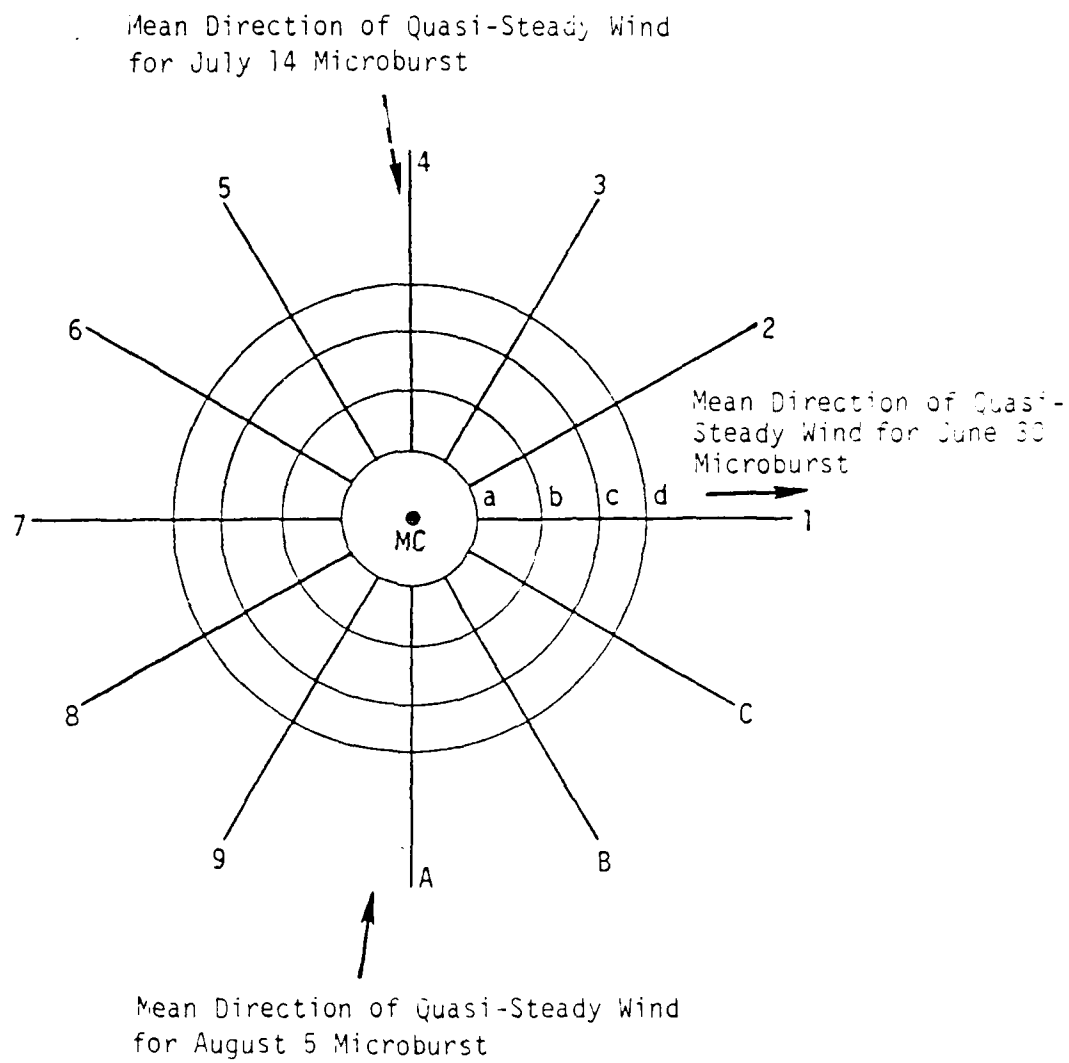
Figure 26. Schematic of sectors and radial lines relative to the microburst center along which turbulence intensity was evaluated.
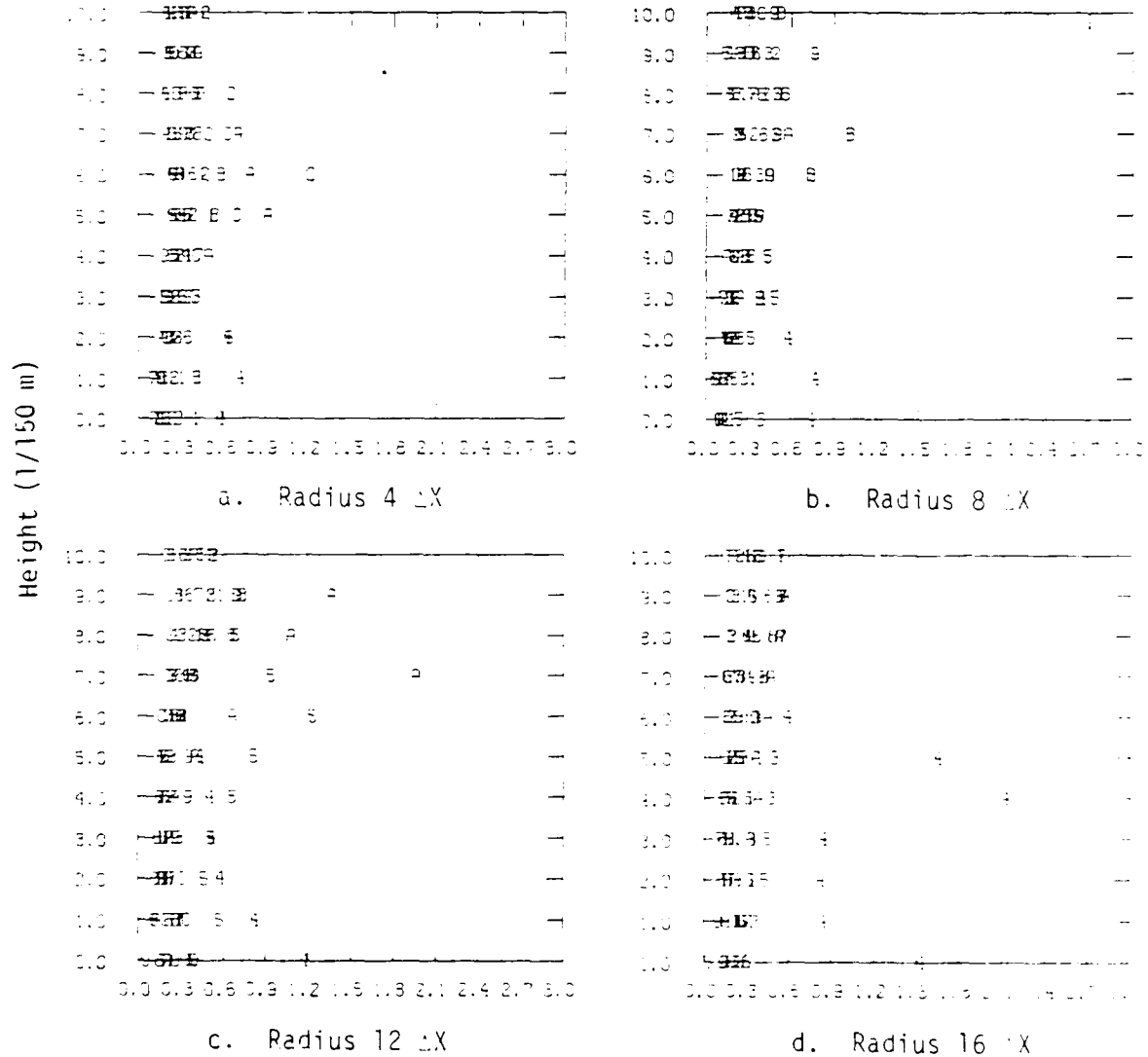
Figure 27. Turbulence intensity $\sigma_t/\overline{V}$ profiles at different radial distances from the microburst center for the 14JL1452 microburst.
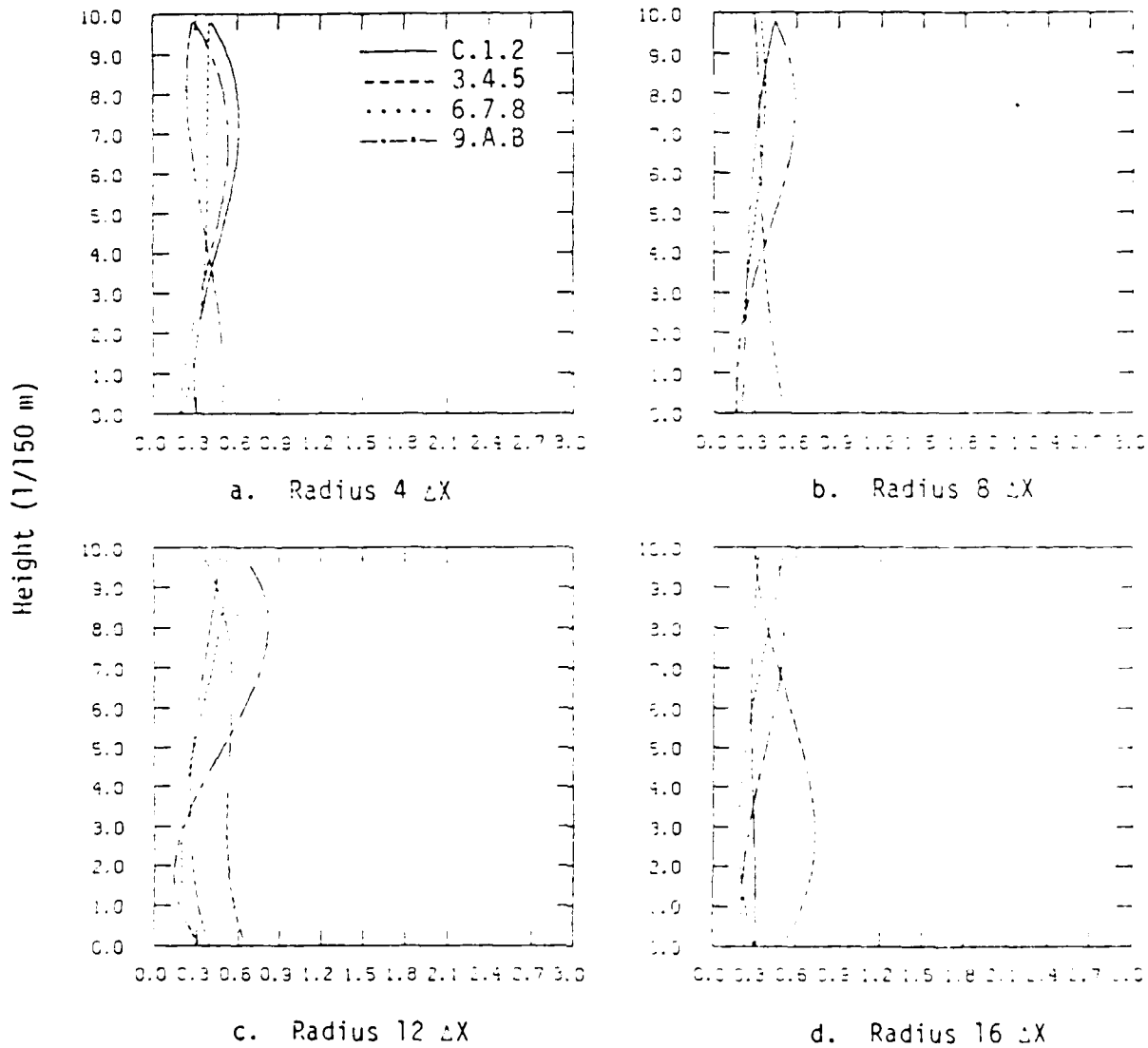
Figure 28. Curve fit of the turbulence intensity profiles $\cdot_t/\overline{V}$ at different radial distances from the microburst center for the 14JL1452 microburst.

approximately at level 4 (750 m above the ground). Moreover, the $\sigma_t/\overline{V}$ in the downwind direction (quarter (9,A,B)) increases first at higher levels then reaches a maximum value at radial distance about 12 times the grid interval at a level of approximately 9 (2000 m above the ground) and decreases at farther radial distances from MC. At altitudes below 600 m, the upwind side of turbulence is more severe than the downwind side of turbulence. However, this is not true at higher altitudes (>600 m). These $\sigma_t/\overline{V}$ profile characteristics suggest that the microburst turbulence intensity is not only a function of the radial distance and height above the ground but also depends on the direction of the quasi-steady mean wind. The August 5 and June 30 microbursts have similar $\sigma_t/\overline{V}$ profiles but because the wind profile structure is much more complicated than the July 14 case whose quasi-steady wind field is quite symmetric about the microburst center, the results obtained for $\sigma_t/\overline{V}$ from the July 14 microburst are not completely the same for either the August 5 or June 30 cases.

A functional form of the normalized $\sigma_t$ as a function of r, the radial distance normalized by the horizontal grid interval, and h, the height normalized by the vertical grid interval, is written:

$$\frac{\sigma_t(r,h)}{\overline{V}} = \left[ A \begin{bmatrix} r^3 \\ r^2 \\ r \\ 1 \end{bmatrix} \right]^T \begin{bmatrix} h^3 \\ h^2 \\ h \\ 1 \end{bmatrix} \qquad (11)$$

where

$$A = \begin{bmatrix} a_1 & b_1 & c_1 & d_1 \\ a_2 & b_2 & c_2 & d_2 \\ a_3 & b_3 & c_3 & d_3 \\ a_4 & b_4 & c_4 & d_4 \end{bmatrix}$$

where the elements of the matrix are determined by the curve-fitting technique. Table 6 lists the matrix elements for the 14JL1452 microburst.

## 2.4.2 Turbulence Length Scales

Length scale is another critical parameter for developing a turbulence model. The auto-correlation coefficient of the quasi-steady mean wind components along each radial direction shown in Figure 26 were curve-fit for each level. Figures 29 and 30 are the three component auto-correlation curves at three levels for the 14JL1452 and the 5AU1847 microbursts, respectively. The longitudinal component is in the direction of the horizontal mean wind. Based on the auto-correlation calculations, the integral length scales were evaluated with the well-known relationship:

$$L = \int_0^\infty R(x)\,dx \qquad (12)$$

TABLE 6. A Functional Form of Turbulence Intensity for 14JL1452 Microburst.

$$\frac{\sigma_t(r,h)}{\bar{V}} = \left\{ \begin{bmatrix} a_1 & b_1 & c_1 & d_1 \\ a_2 & b_2 & c_2 & d_2 \\ a_3 & b_3 & c_3 & d_3 \\ a_4 & b_4 & c_4 & d_4 \end{bmatrix} \begin{bmatrix} r^3 \\ r^2 \\ r \\ 1 \end{bmatrix} \right\}^T \begin{bmatrix} h^3 \\ h^2 \\ h \\ 1 \end{bmatrix}$$

| Quarter | (C,1,2) | (3,4,5) | (6,7,8) | (9,A,B) |
|---|---|---|---|---|
| $a_1$ | -0.551049E-06 | 0.741460E-05 | 0.911788E-06 | 0.657271E-06 |
| $b_1$ | 0.407547E-05 | -0.180272E-03 | -0.246583E-04 | 0.334910E-05 |
| $c_1$ | 0.197432E-03 | 0.102663E-02 | 0.104663E-03 | -0.394346E-03 |
| $d_1$ | -0.184692E-02 | -0.130838E-02 | -0.356118E-03 | -0.268900E-03 |
| $a_2$ | 0.332280E-05 | -0.116770E-03 | -0.270999E-04 | -0.225209E-04 |
| $b_2$ | 0.327677E-04 | 0.284746E-02 | 0.804118E-03 | 0.353051E-03 |
| $c_2$ | -0.262014E-02 | -0.163677E-01 | -0.477002E-02 | 0.288384E-02 |
| $d_2$ | 0.229965E-01 | 0.241284E-01 | 0.824520E-02 | 0.266095E-02 |
| $a_3$ | 0.664155E-04 | 0.529400E-03 | 0.215985E-03 | 0.179236E-03 |
| $b_3$ | -0.229589E-02 | -0.132217E-01 | -0.684668E-02 | -0.457740E-02 |
| $c_3$ | 0.208904E-01 | 0.782930E-01 | 0.507962E-01 | 0.189846E-01 |
| $d_3$ | -0.569887E-01 | -0.149245E+00 | -0.642522E-01 | -0.589026E-02 |
| $a_4$ | -0.180032E-03 | -0.704053E-03 | -0.258038E-03 | -0.180251E-03 |
| $b_4$ | 0.562896E-02 | 0.186553E-01 | 0.874772E-02 | 0.576422E-02 |
| $c_4$ | -0.434284E-01 | -0.962702E-01 | -0.779505E-01 | -0.458536E-01 |
| $d_4$ | 0.327257E+00 | 0.525894E+00 | 0.374366E+00 | 0.282357E+00 |
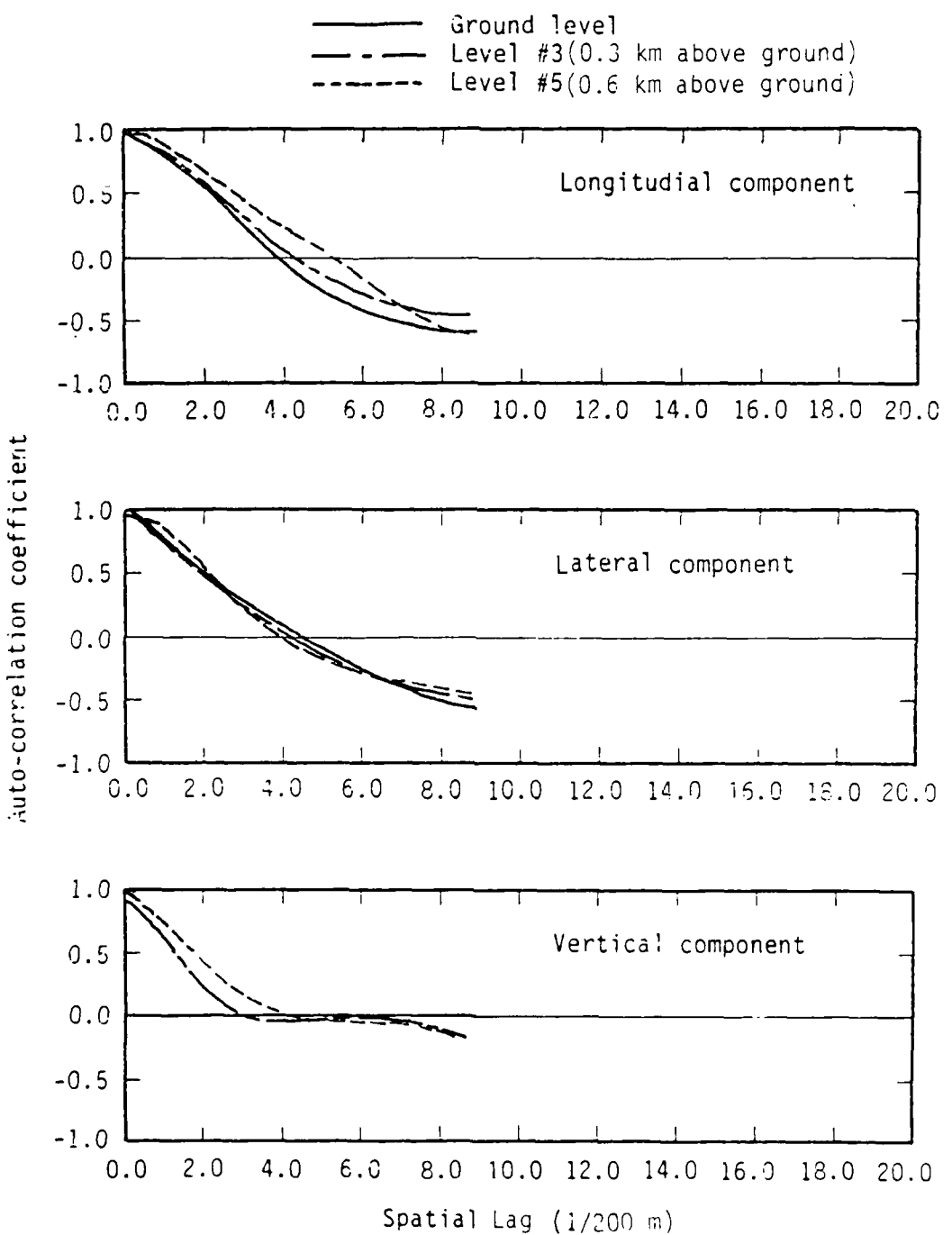
Figure 29.   Auto-correlation coefficient of velocity components for
             14JL1452 microburst.
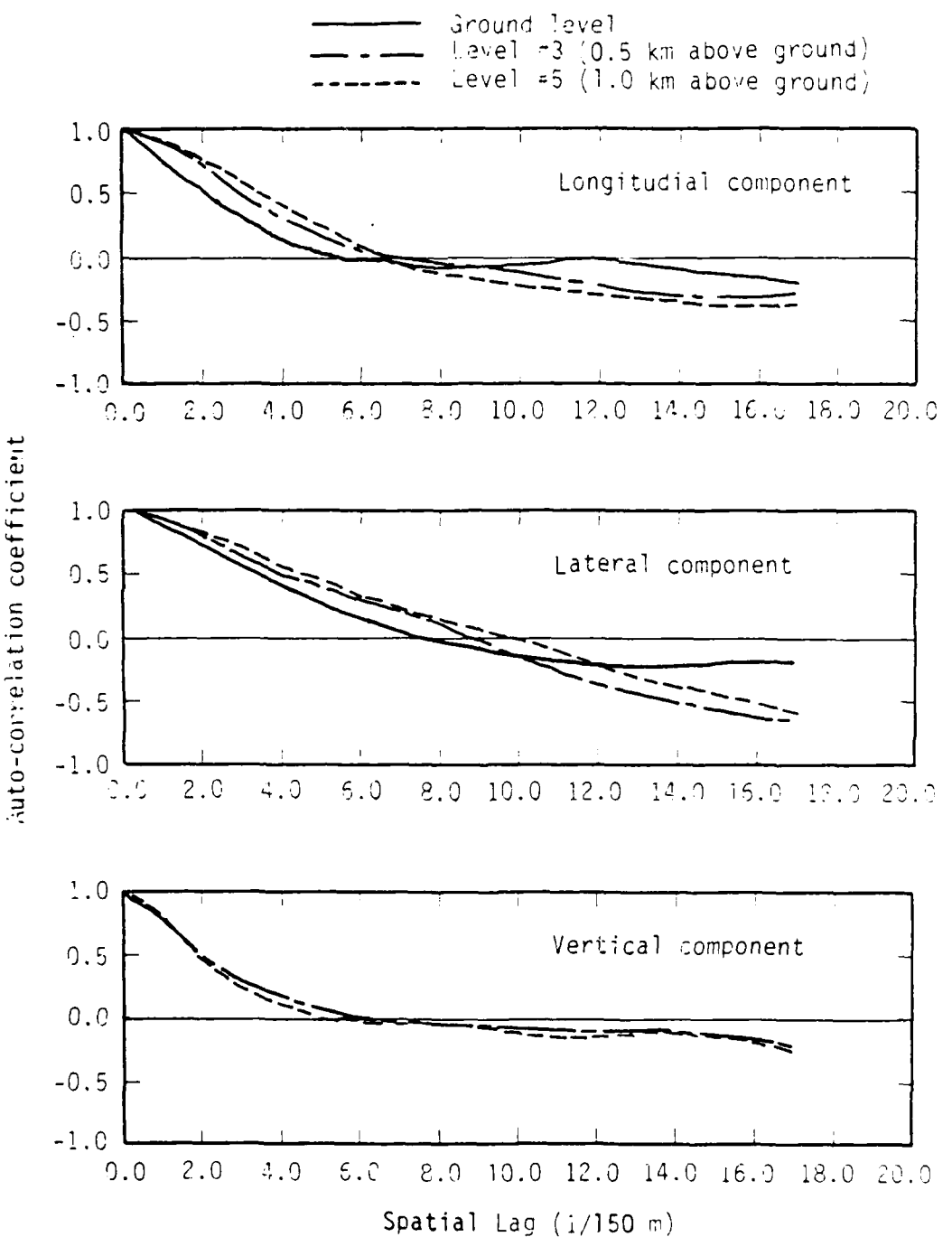
Figure 30.  Auto-correlation coefficient of velocity components for 5AU1847 microburst.

Table 7 shows the integral scale at each level for the July 14 and August 5 microbursts. As mentioned earlier, most investigators use a simple function of height to model the turbulence length scale in the atmospheric boundary layer. These functions are probably not true for microburst turbulence. Therefore, the relation between the turbulence scale and the height shown in Table 7 is used in the microburst turbulence simulation reported later in this study. The magnitude of the turbulence length scales, however, is too large because they include scales larger than the grid size (150-200 m) of the JAWS data sets. These scale sizes are already included in the quasi-steady wind data. To obtain a more representative length scale to use in the microburst turbulence simulation, the integral scales shown in Table 7 were somewhat arbitrarily multiplied by a constant factor of one-third to reduce them to typical grid sizes.

## 2.4.3 Turbulence Spectrum

In constructing a turbulence model, a key parameter is the spectrum of the turbulence. The spectrum is a measure of the energy associated with fluctuations of specific frequencies within the turbulence flow. The normalized auto-spectra of the turbulence components measured in Flight 6 Runs 24 and 23 of the NASA B-57B aircraft program are shown in Figures 31 and 32. The corresponding analytical Dryden and von Karman spectrum models are also shown in the figures. It can be seen that both the Dryden and von Karman spectra are reasonable approximations to the turbulence spectra measured near the microburst. Thus, since the two models appear to give similar results and because the form of the Dryden spectrum is more readily adaptable to mathematical manipulation, it is used in this study. Also, the Dryden spectrum is the spectrum currently recommended by the FAA in AC-120-41. The Dryden spectra for the three velocity fluctuation components, respectively, can be written as:

$$\phi_1(K) = \sigma_1^2 \, \frac{2\Lambda_1}{\pi} \, \frac{1}{1 + \Lambda_1^2 K^2}$$

$$\phi_2(K) = \sigma_2^2 \, \frac{\Lambda_2}{\pi} \, \frac{1 + 3\,\Lambda_2^2 K^2}{(1 + \Lambda_2^2 K^2)^2} \tag{13}$$

$$\phi_3(K) = \sigma_3^2 \, \frac{\Lambda_3}{\pi} \, \frac{1 + 3\,\Lambda_3^2 K^2}{(1 + \Lambda_3^2 K^2)^2}$$

where the subscripts 1, 2, and 3 represent the longitudinal, lateral, and vertical components, respectively; $\Lambda$ is the length scale; $\sigma$ is the turbulence intensity; and K is the wave number.

TABLE 7.  Integral Scales.

| August 5, 1982, 1847 Microburst | | | |
|---|---|---|---|
| Level | Longitudinal (m) | Lateral (m) | Vertical (m) |
| 1 (0 m) | 319 | 513 | 0 |
| 2 (250 m) | 419 | 450 | 355 |
| 3 (500 m) | 464 | 666 | 351 |
| 4 (750 m) | 559 | 682 | 338 |
| 5 (1000 m) | 520 | 713 | 317 |
| 6 (1250 m) | 403 | 473 | 292 |
| 7 (1500 m) | 473 | 334 | 254 |
| 8 (1750 m) | 468 | 475 | 234 |
| 9 (2000 m) | 524 | 521 | 236 |

| July 14, 1982, 1452 Microburst | | | |
|---|---|---|---|
| Level | Longitudinal (m) | Lateral (m) | Vertical (m) |
| 1 (0 m) | 422 | 422 | 0 |
| 2 (150 m) | 558 | 336 | 292 |
| 3 (300 m) | 465 | 432 | 310 |
| 4 (450 m) | 549 | 515 | 338 |
| 5 (600 m) | 553 | 421 | 369 |
| 6 (750 m) | 526 | 427 | 391 |
| 7 (900 m) | 433 | 435 | 395 |
| 8 (1050 m) | 437 | 417 | 385 |
| 9 (1200 m) | 365 | 409 | 374 |
| 10 (1350 m) | 456 | 577 | 367 |
| 11 (1500 m) | 418 | 500 | 367 |
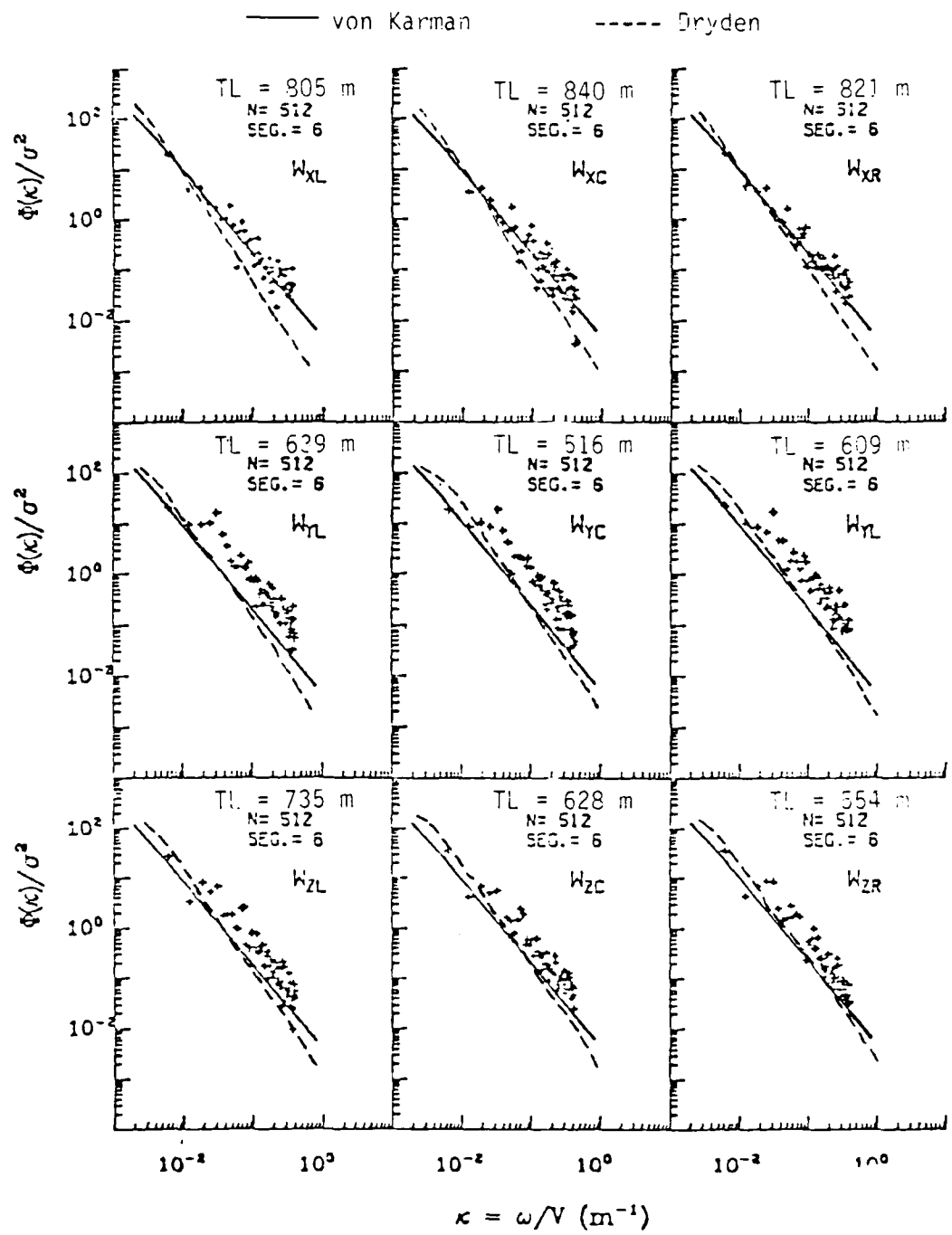
Figure 31.  Normalized auto-spectra of turbulence components (Flight 6, Run 24; NASA B-57B aircraft).
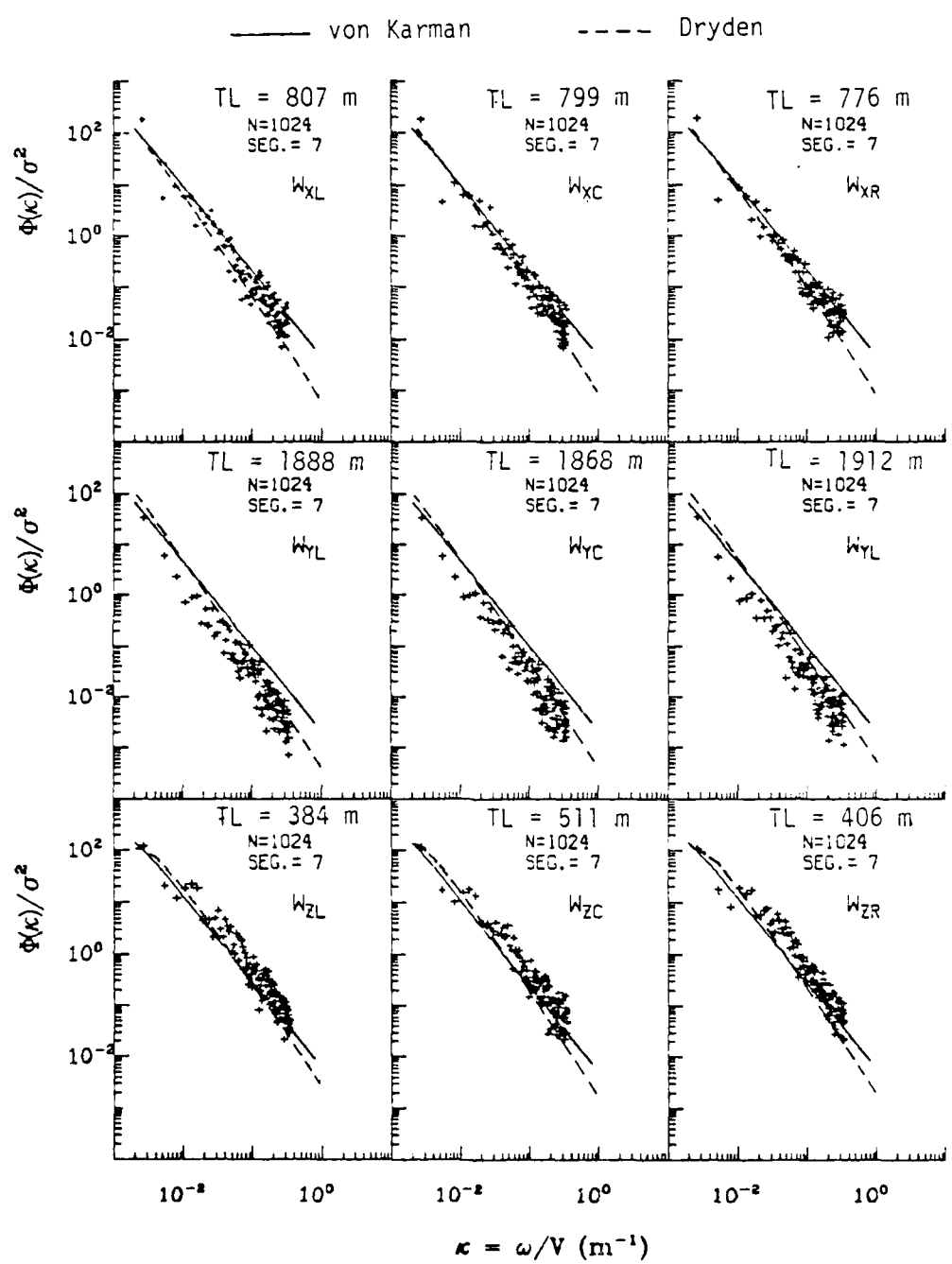
Figure 32. Normalized auto-spectra of turbulence components (Flight 6, Run 23; NASA B-57B aircraft).

## 3.0 MICROBURST TURBULENCE MODEL AND ITS APPLICATION IN FLIGHT SIMULATION

The microburst turbulence intensity and length scale obtained in the previous sections, although somewhat subjective and based on limited data, were used to develop a microburst turbulence simulation model. A z-transformation technique, which is based on the Dryden hypothesis of the spectral density function of turbulence and Taylor's frozen eddy hypothesis, has been developed by Wang and Frost (1980) and Huang and Frost (1984). We assume that the isotropic shapes of the spectrum hold for the non-isotropic conditions which occur at a very low altitude but that the turbulence intensity and the integral scale vary spatially.

Microburst turbulence components along an aircraft's trajectory are calculated by utilizing the z-transform technique. This technique uses a filter function, namely, the Dryden spectrum. Gaussian white noise signals are computer generated and passed through the filter to provide the simulated time history of the turbulence as output (see Figure 33). The same technique is also applied to generate the turbulence model suggested by the FAA in AC-120-41, and the two models are compared in a later section.

Using a rational spectral model, simulated turbulence can be generated with the difference equations. The z-transformation technique is a digital simulation model where the nth turbulent point is a function of the previous turbulence fluctuation values and noise signals. For the Dryden model, the difference equations are written as (see Huang and Frost 1984):

$$y_n = c_1 y_{n-1} + c_2 y_{n-2} + d_1 x_{n-1} + d_2 x_{n-2} \tag{14}$$

where $c_1$, $c_2$, $d_1$, and $d_2$ are parameters depending on the sampling rate ($\Delta t$), mean wind speed ($\bar{V}$), turbulence intensity ($\sigma_1$, $\sigma_2$, and $\sigma_3$), and turbulence length scale ($\lambda_1$, $\lambda_2$, and $\lambda_3$); y represents the digital generated turbulence component; and x designates the digital random noise signal. For the Dryden model, the constant parameters $c_1$, $c_2$, $d_1$, and $d_2$ are given as:



|          |        |           |
| Gaussian | Filter | Simulated |
| White Noise |     | Atmospheric |
|          |        | Turbulence |
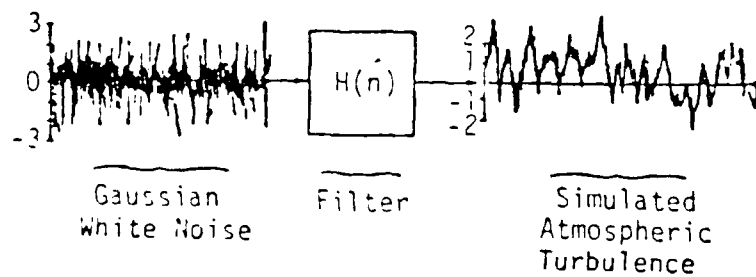
Figure 33. Turbulence simulation technique.

$$c_1 = \exp\left(\frac{-\overline{V}}{\lambda_1}\, \Delta t\right)$$

$$c_2 = 0 \tag{15}$$

$$d_1 = \sigma_1 \left[\frac{2\lambda_1}{\pi \overline{V}}\right]^{\frac{1}{2}} (1 - c_1)$$

$$d_2 = 0$$

for the longitudinal component and

$$c_1 = 2\exp\left[- \frac{\overline{V}}{\lambda_2}\, \Delta t\right]$$

$$c_2 = -\exp\left[-2\, \frac{\overline{V}}{\lambda_2}\, \Delta t\right] \tag{16}$$

$$d_1 = \left[\frac{3\overline{V}\sigma_2{}^2}{\pi\lambda_2}\right]^{\frac{1}{2}} \left\{\frac{\lambda_2}{\sqrt{3}\ \overline{V}} + \frac{1}{2}\, c_1\left[\left(1 - \frac{1}{\sqrt{3}}\right)\Delta t - \frac{\lambda_2}{\sqrt{3}\ \overline{V}}\right]\right\}$$

$$d_2 = \left[\frac{3\overline{V}\sigma_2{}^2}{\pi\lambda_2}\right]^{\frac{1}{2}} \left\{\frac{\lambda_2}{\sqrt{3}\ \overline{V}} \left(\frac{1}{2}\, c_1 - 1\right) - \left(1 - \frac{1}{\sqrt{3}}\right)\Delta t\right\}\left(\frac{1}{2}\, c_1\right)$$

for the lateral component. The vertical component has the same form as the lateral component, except for a different length scale and turbulent intensity, i.e., $\lambda_3$ and $\sigma_3$. The sampling interval used in the simulation is 0.5 second.

Results of the simulation are presented in Figures 34 through 37 using the FWG/JAWS and the FAA turbulence models, respectively. Figures 34 and 35 show three typical turbulent wind velocity components (quasi-steady mean wind + turbulence fluctuation) and resulting trajectories of a B727-type aircraft approaching through the JAWS 5AU1847 microburst along path $\overline{AB}$ ($z_0 = 300$ ft). The nomenclature used in defining the orientation of the runway to the wind field for both approach and takeoff cases are those described in Frost et al. (1985) (see Appendix). The simulation in Figure 34 uses the turbulence model derived from the JAWS data; Figure 35 shows similar results using the turbulence model suggested by the FAA in AC-120-41. While microburst turbulence may increase the workload of a pilot, its influence on the aircraft's trajectory would not, in general, be significant enough to alter the outcome of an approach or take off. Figures 36 and 37 show the spatial history of the turbulence fluctuations encountered by the aircraft in the simulation results given in Figures 34 and 35, respectively. Since the same noise signals are used for both the FWG/JAWS and the FAA models, the
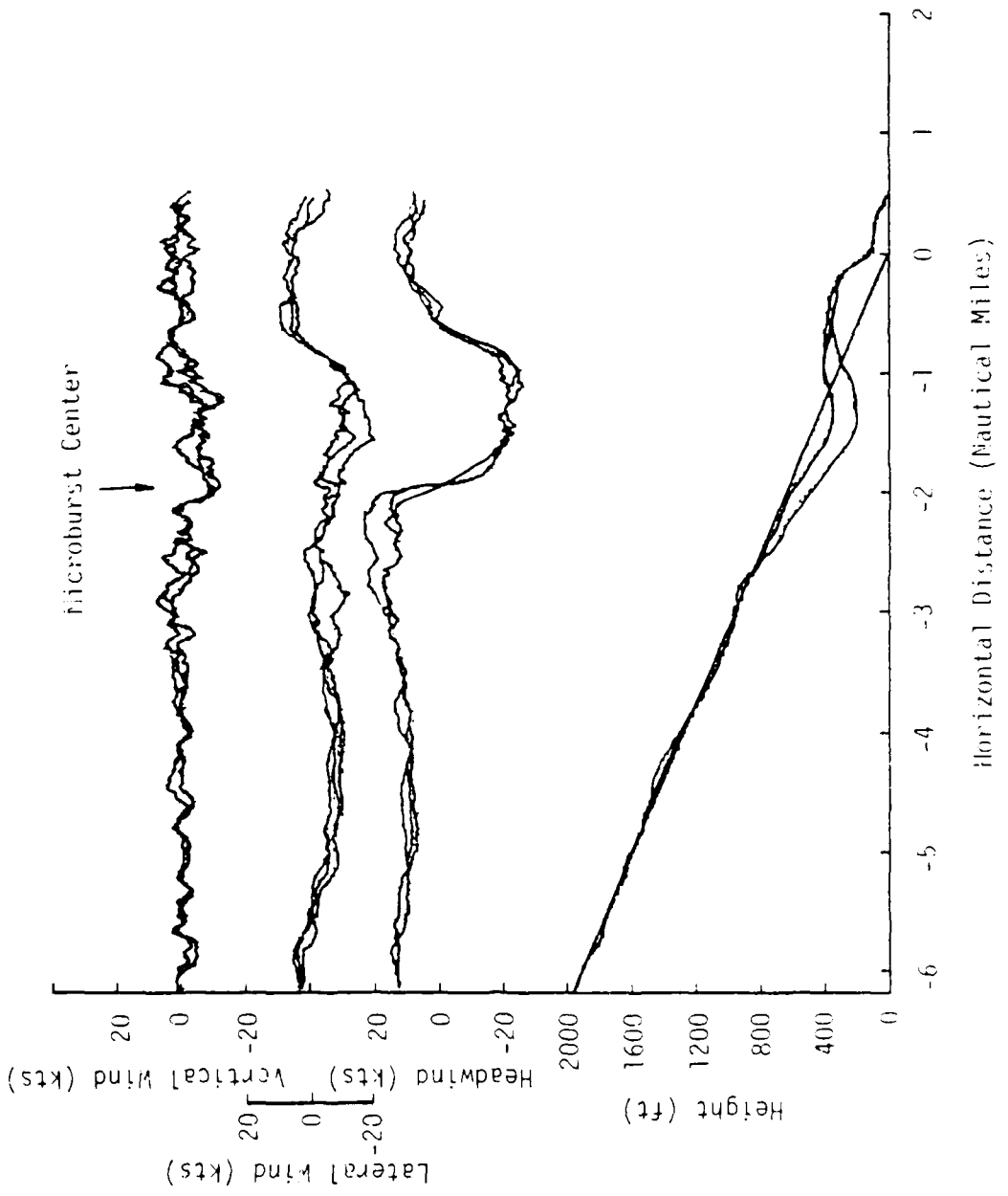
Figure 34. Three typical approach paths of a B727-type aircraft along path $\overline{AB}$ ($z_g = 300$ ft) encountering turbulence from TWG/JAWS model superimposed on quasi-steady winds (5AU1847 microburst).
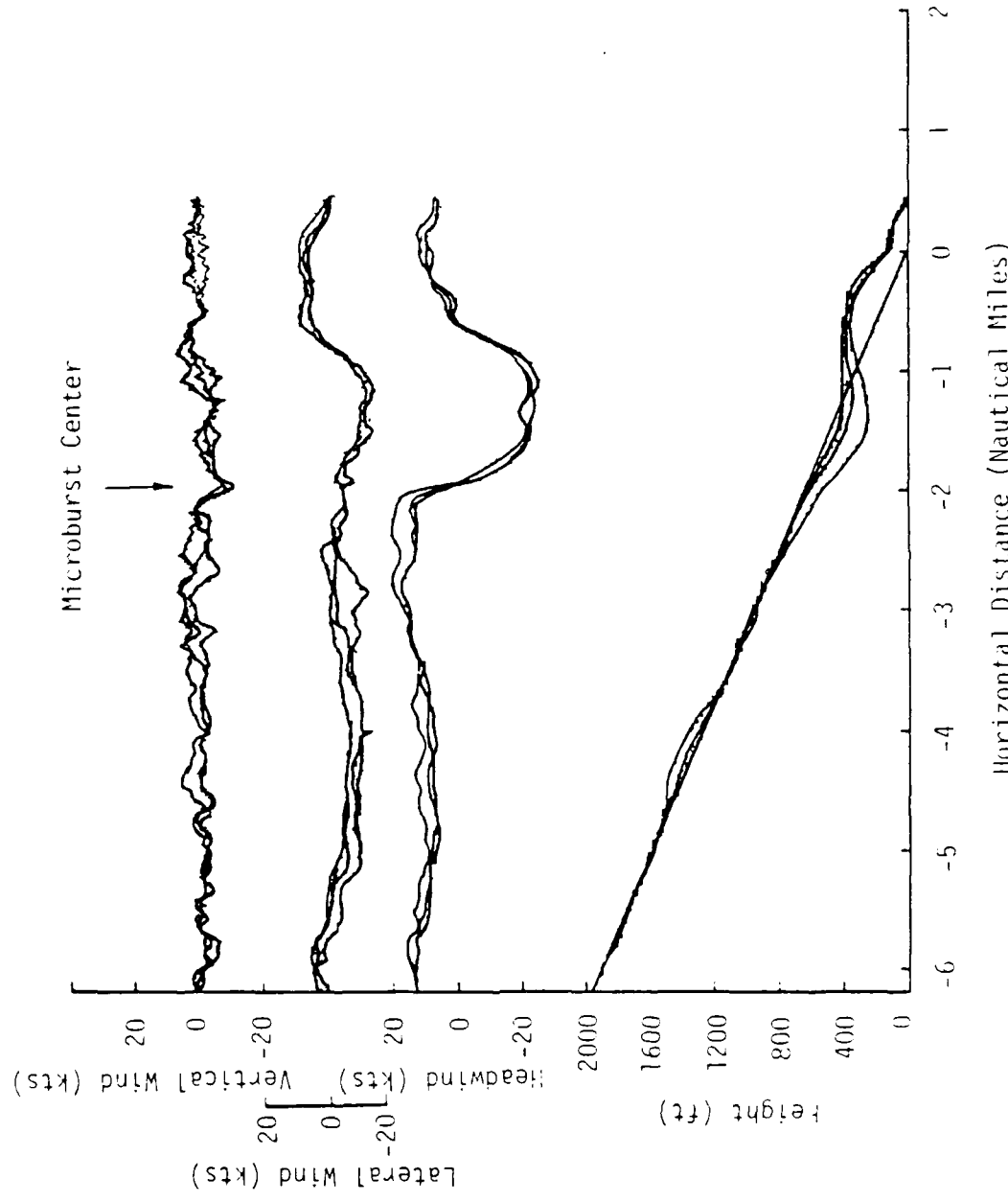
Figure 35.   Three typical approach paths of a B727-type aircraft along path AB ($z_0 = 300$ ft) encountering turbulence from FAA model superimposed on quasi-steady winds (5AUI847 microburst).
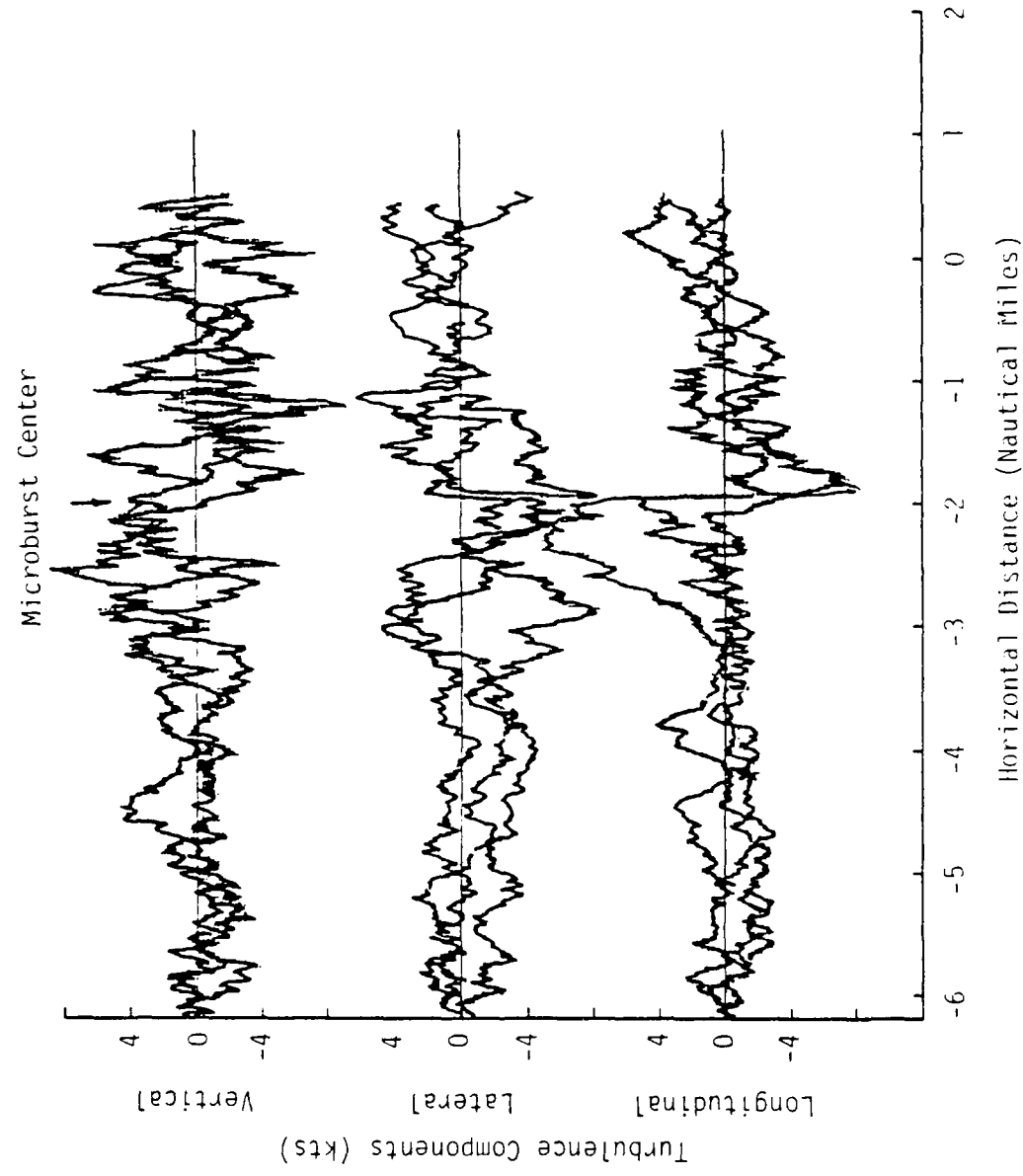
Figure 36. Turbulent fluctuations corresponding to the approach paths shown in Figure 34 (path $\overline{AB}$, $z_0 = 300$ ft) using the TWG/JAWS turbulence model (5AU1847 microburst).

59
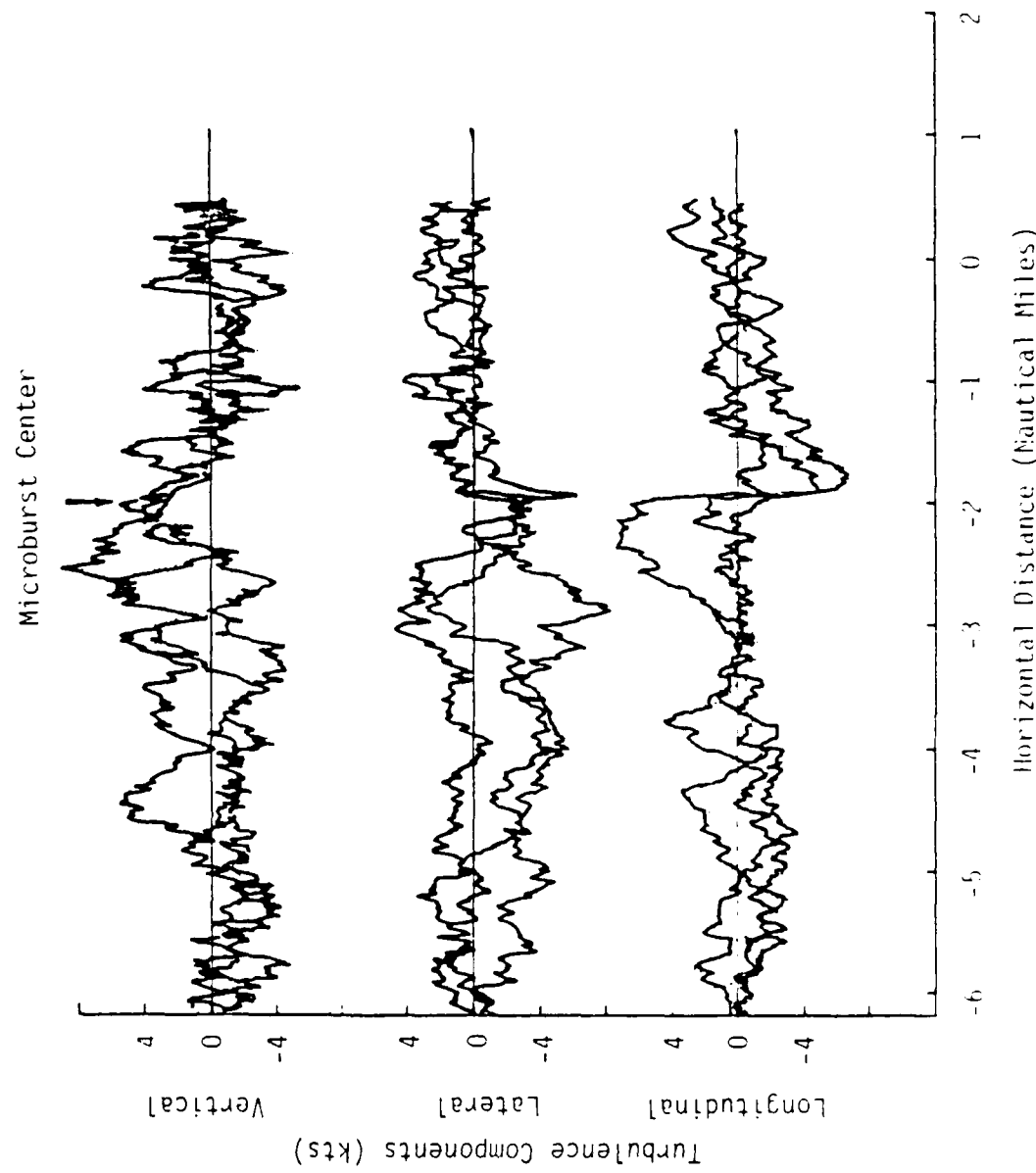
Figure 37. Turbulent fluctuations corresponding to the approach paths shown in Figure 35 (path AB, $z_0 = 300$ ft) using the FAA turbulence model (5A01847 microburst).

turbulence fluctuation patterns encountered by the aircraft are roughly similar to each other. However, the figures do show that the aircraft encounters more severe turbulence with the JAWS model than with the FAA model, especially near the microburst center. This increased turbulence in the region of strong shear is very consistent with physical reasoning and suggests that the JAWS model is physically more realistic.

Finally, a number of takeoffs with turbulence superimposed were simulated. Turbulence effects on the aircraft were assumed negligible until the aircraft's liftoff. Results of five takeoffs for different turbulence realizations based on the FWG/JAWS model (5AU1847 microburst) along the intended path $\overline{AB}$ ($z_0$ = 66 ft) are presented in Figure 38. Total turbulent velocity components (quasi-steady mean wind + turbulence fluctuations) and the aircraft's trajectories in a vertical plane are shown in the figure. Based on these five simulations, the maximum deviation of the climb-out trajectory from the reference flight path computed without turbulence is approximately 80 ft at a horizontal distance about 2 nautical miles from brake release. The standard deviations of the aircraft trajectories about the no turbulence flight path at horizontal distances of 1.5, 2.0, and 2.5 nautical miles are 25, 45, and 50 ft, respectively. Turbulence effects clearly influence the climb-out trajectory; however, this influence on the ultimate outcome of the departure is not, in general, significant. This conclusion is also true for the landing simulations shown earlier. However, in those cases, maximum departure from the intended flight path was on the order of 250 to 300 ft.
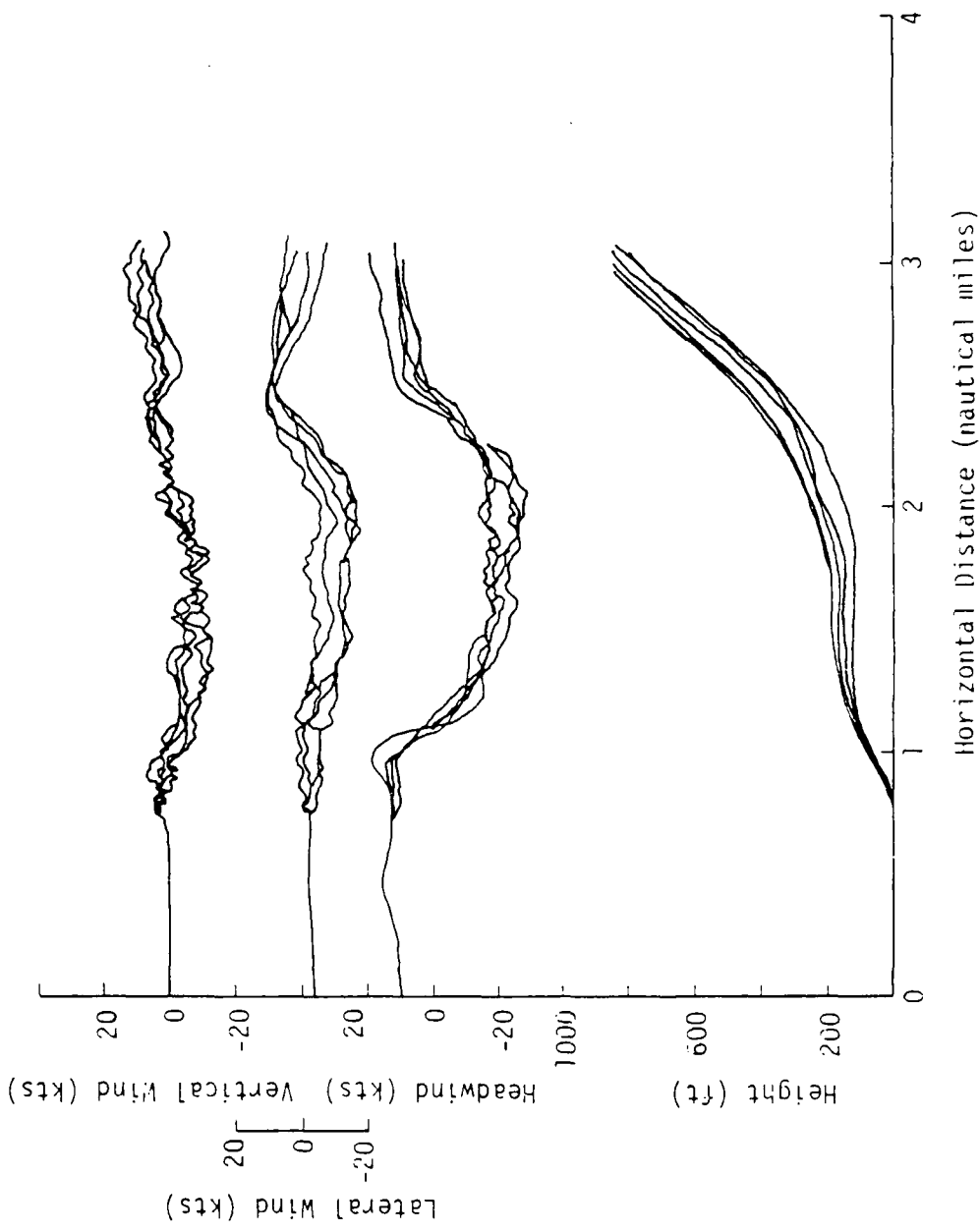
Figure 38.  Takeoff simulation of a B727-type aircraft along path AB ($z_o$ = 66 ft) using the FWG/JAWS turbulence model (5AU1847 microburst).

62

# 4.0 CONCLUSIONS

Turbulence information associated with the JAWS microburst data sets measured on August 5, July 14, and June 30, 1982, has been analyzed. Microburst turbulence intensity is calculated by subtracting the spectrum broadenings due to wind shear, antenna motion, and precipitation fall speeds from the second moment, namely, the radar spectral width. (Note that the pulse volume was a Cressman weighted average as discussed in Section 2.1.) The analysis shows that local isotropic turbulence is a reasonable assumption for the microburst turbulence model. The August 5 microburst, recommended as a good scenarios to be used in flight simulations, contains the strongest wind shear and most significant turbulence effects among the three microbursts. Both the von Karman and Dryden analytical spectrum functions appear to be good approximations of the partitioning of energy among the turbulent eddies (at least for high frequency) in a microburst.

Comparison of the turbulence intensity derived from the JAWS radar second moment with that from the *in situ* measurement of the NASA B-57B aircraft shows the former is about three times of the latter. This difference is probably caused by the fact that the radar-measured turbulence intensity is representative of three-dimensional spatially distributed turbulence and the aircraft-measured value is based on the aircraft's trajectory only. Several investigators reported a similar inconsistency between the radar/lidar spectral width which is regarded as a turbulence indicator and the aircraft-measured turbulence intensity. Efforts to examine this area theoretically and experimentally are highly recommended.

A z-transformation turbulence simulation technique has been developed to account for small-scale perturbation not previously contained in the smoothed JAWS microburst quasi-steady wind profiles (JAWS microburst data sets). The turbulence model derived from the radar-measured turbulence information is believed to be physically more realistic than the FAA AC-120-41 model because it shows stronger turbulence intensity in the high shear regions of the microburst. Flight simulations of a B727-type aircraft through the JAWS microbursts with turbulence superimposed suggest that although workload of a pilot may be significantly increased, the outcome of the approach or takeoff is, in general, not changed.

## REFERENCES

Barr, N. M., D. Gangaas, and D. R. Schaeffer (1974). "Wind Models for Flight Simulation Certification of Landing and Approach Guidance and Control Systems," FAA Report No. FAA-RD-74-206.

Bohne, A. R. (1985). "Joint Agency Turbulence Experiment--Final Report," AFGL-TR-85-0012, January.

Bohne, A. R. (1981). "Radar Detection of Turbulence in Thunderstorms," AFGL-TR-81-0102, March.

Boldman, D. R., and P. F. Brinich (1977). "Mean Velocity, Turbulence Intensity, and Scale in a Subsonic Turbulent Jet Impinging Normal to a Large Flat Plate," NASA TP-1037.

Burnham, J., and J. T. Lee (1969). "Thunderstorm Turbulence and Its Relationship to Weather Radar Echoes," Journal of Aircraft, 6(5), Sept.-Oct.

Campbell, W. C. (1984). "A Spatial Model of Wind Shear and Turbulence for Flight Simulations," NASA TP-2313, May.

Costello, F. A. (1976). "Velocity Field of a Gaussian Circular Jet with Normal Impingement," Journal of Applied Mechanics, Dec., pp. 551-554.

Crabb, D., D. F. G. Durão, and J. H. Whitelaw (1981). "A Round Jet Normal to a Crossflow," Journal of Fluids Engineering, 103:142-153, March.

Doviak, R. J., and D. S. Zrnic' (1984). "Doppler Radar and Weather Observation," Academic, Orlando, Fla.

Elmore, K. L., and J. McCarthy (1984). Private communication.

Fichtl, G. H. (1973). "Problems in the Simulation of Atmospheric Boundary-Layer Flows," AGARD Conference Proceedings No. 140, Advisory Group for Aerospace R&D, Neuilly Sur Sein, France.

Frost, W. (1984). "Turbulence Models," Presentation at the NASA Langley Wind Shear/Turbulence Workshop, May 30-June 1.

Frost, W., and R. Bowles (1984). "Wind Shear/Turbulence Inputs to Flight Simulation and Systems Certification," Proceedings. NASA Langley Research Center, Hampton, Va.

Frost, W., H. P. Chang, K. L. Elmore, and J. McCarthy (1985). "Microburst Wind Shear Models from JAWS," Final report under NCAR Subcontract S3011, January.

Frost, W., R. E. Turner, and B. H. Long (1978). "Engineering Handbook on the Atmospheric Environmental Guidelines for Use in Wind Turbine Generator Development," NASA TP 1359.

Huang, K. H., and W. Frost (1984). "Monte Carlo Particle Dispersion (MoCaPD) Model of Battlefield Obscuration," Final report for US Army Contract DAAG29-81-D-0100, by FWG Associates, Inc.

Istok, M. (1981). "Analysis of Doppler Spectrum Broadening Mechanisms in Thunderstorms," Paper presented at the 20th Radar Meteorology Conference.

Keeler, J., and C. Frush (1985). Private communication.

Lee, J. T. (1981). "Doppler Radar-Research and Application to Aviation Flight Safety, 1977-1979," DOT/FAA/RD-81/79, June.

Lee, J. T. (1977). "Application of Doppler Weather Radar to Turbulence Measurements Which Affect Aircraft," FAA-RD-77-145, 44 pp.

Lhermitte, R. M. (1968). "Turbulent Air Motions as Observed by Doppler Radar," Preprints of the 13th Radar Meteorology Conference, Montreal, Canada. American Met. Society, Boston, Mass.

Robison, F. L., and T. G. Konrad (1974). "A Comparison of the Turbulent Fluctuations in Clear Air Convection Measured Simultaneously by Aircraft and Doppler Radar," Journal of Applied Meteorology, 13:481-487.

Shayesteh, M. V., I. M. M. A. Shabaka, and P. Bradshaw (1985). "Turbulence Structure of a Three Dimensional Impinging Jet in a Cross Stream," AIAA-85-0044, AIAA 23rd Aerospace Sciences Meeting, Jan. 14-17, Reno, Nev.

Wang, S. T., and W. Frost (1980). "Atmospheric Turbulence Simulation Techniques with Application to Flight Analysis," NASA CR-3309.

Zegadi, R., J. L. Balint, R. Morel, and G. Charnay (1983). "The Influence of a Low Reynolds Number on an Impinging Round Jet," Structure of Complex Turbulent Shear Flow, IUTAM Symposium Marseille 1982 (R. Dumas and L. Fulachier, eds.).

APPENDIX

## NOMENCLATURE USED IN APPROACH/TAKEOFF SIMULATIONS

The nomenclature used in defining the orientation of the runway to the wind field are illustrated in this Appendix for both approach and takeoff cases. To investigate the influence of the microburst position relative to the intended touchdown or liftoff point on the runway, the center of the microburst is mathematically shifted along the path with respect to the runway. The runway is positioned relative to the center of the microburst such that an aircraft following the glide slope or takeoff path passes through the center of the microburst at a given height to be designated as $z_0$.

Figure A.1 schematically depicts the nomenclature used in the approach simulations. The intended touchdown point, TD, is the threshold of the runway corresponding to the specific flight path. The distance of the threshold from the microburst center is calculated as $z_0/\tan \gamma$, where $\gamma$ is the glide slope angle. A value of $z_0 = 0$ corresponds to the threshold of the runway coinciding with the microburst center. The orientation of the runway, $\theta$, is measured relative to the positive x direction. The $(x_0, y_0)$ coordinates designate the position in the horizontal plane at which $z_0$ is measured. Values of $x_0$ and $y_0$ are measured relative to an origin located at the northwest corner of the full-volume data set. For the August 5 microburst, the origin is at (-4.38 mi, -11.22 mi), (-7.05 km, -18.05 km), as measured from CP-2.

Takeoff path definition and orientation are shown in Figure A.2. The liftoff point, LO, is the end of the runway corresponding to the specific flight path. A 10° liftoff path with 5000 ft ground run (see Figure A.2) is selected as a refernce only for purposes of defining the position of the microburst relative to the runway. The B727-type aircraft, for example, would liftoff after approximately a 5000 ft run but would climb-out on an approximate 6.4° path if there was zero wind. The location of the center of the microburst is selected relative to the liftoff point, in a manner similar to that of the approach. The value of $z_0$ for takeoff is defined as the height at which the aircraft would pass through the center of the microburst when accelerating along the runway for 5000 ft and then climbing out along an arbitrarily defined 10° reference path. A negative $z_0$ indicates the aircraft is passing through the center of the microburst while still on the runway.
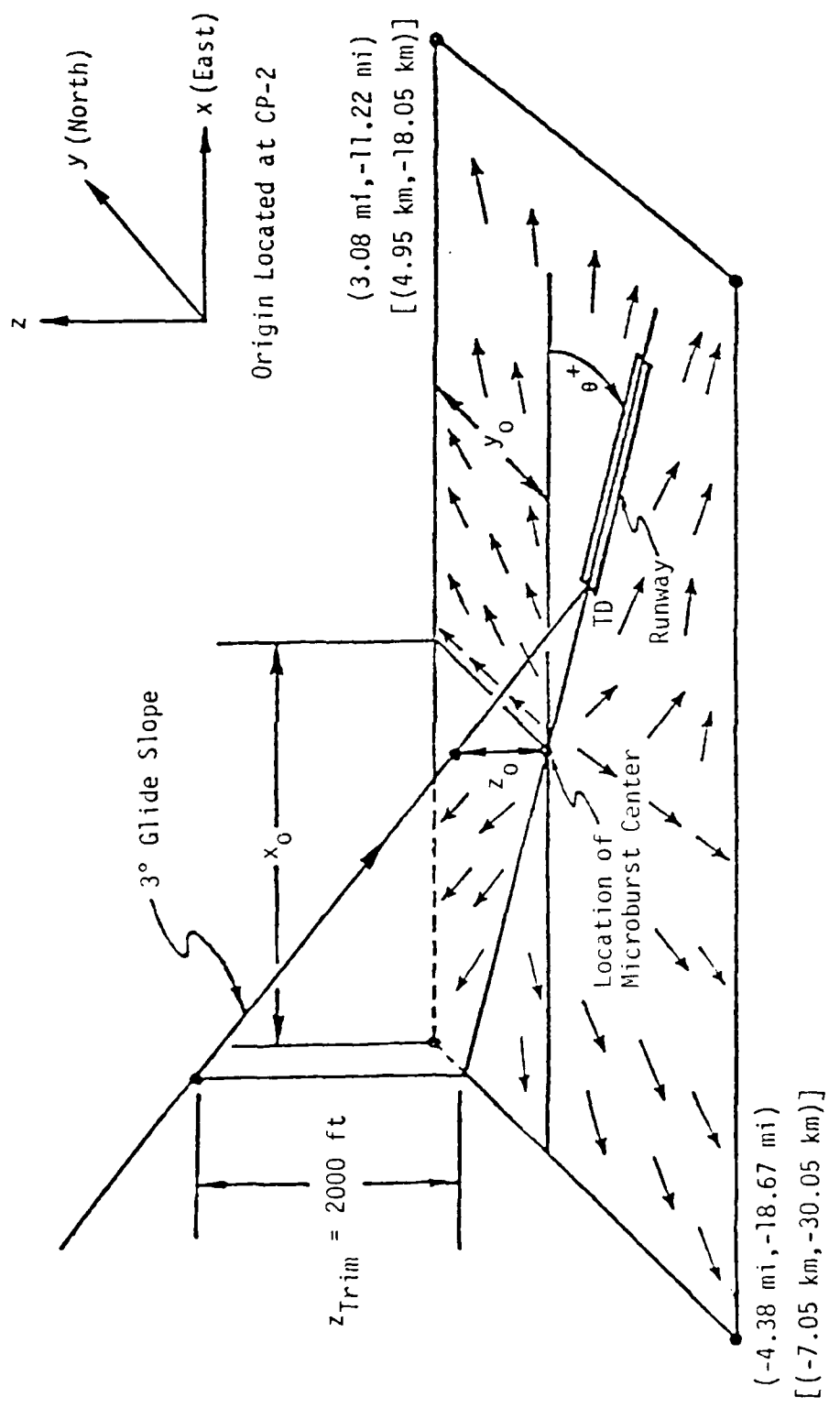
Figure A.1. Approach path definition and orientation (relative to the full-volume of the 5AU1847 microburst).

y (North)

x (East)

z

Origin Located at CP-2

(3.08 mi,-11.22 mi)
[(4.95 km,-18.05 km)]

$y_0$

$+$
$\theta$

TD

Runway

$x_0$

$z_0$

Location of
Microburst Center

3° Glide Slope

$z_{Trim}$ = 2000 ft

(-4.38 mi,-18.67 mi)
[(-7.05 km,-30.05 km)]

67
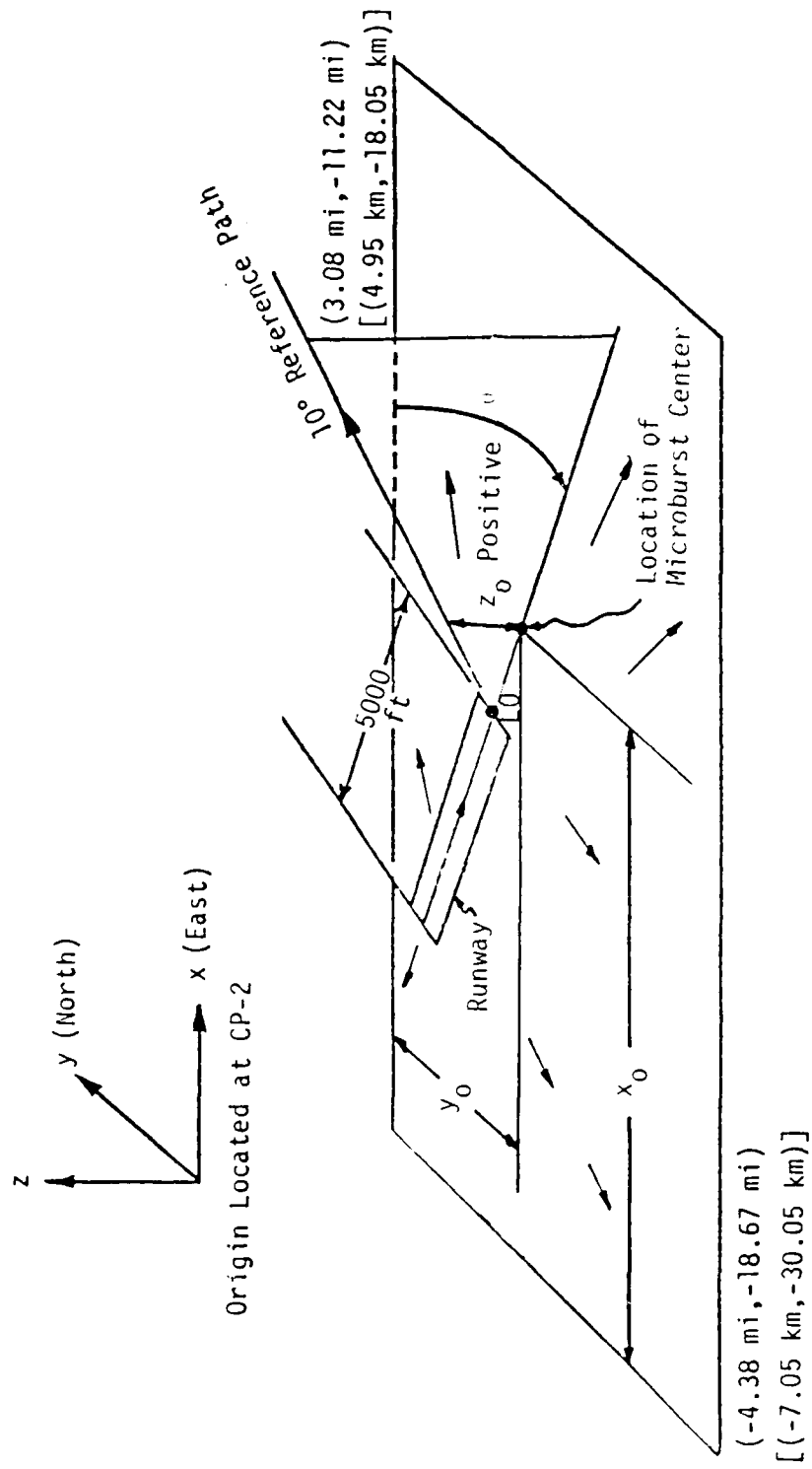
Figure A.2. Takeoff path definition and orientation (relative to the full-volume of the 5AU1847 microburst).

68

END
DATE
FILMED
JAN
1988